Lamb Wave Based Structural Health Monitoring of Aircraft Structures

by

Carlos Manuel Baptista Pereira da Silva
Licenciatura Aeronautical Engineering, Portuguese Air Force Academy, 2002
Master of Applied Science, University of Victoria, 2007

A Dissertation Submitted in Partial Fulfillment
of the Requirements for the Degree of

DOCTOR OF PHILOSOPHY

in the Department of Mechanical Engineering

Lamb Wave Based Structural Health Monitoring of Aircraft Structures

by

Carlos Manuel Baptista Pereira da Silva
Licenciatura Aeronautical Engineering, Portuguese Air Force Academy, 2002
Master of Applied Science, University of Victoria, 2007

SUPERVISORY COMMITTEE

Dr. Afzal Suleman (Department of Mechanical Engineering)
Supervisor

Dr. Daniela Constantinescu (Department of Mechanical Engineering)
Departmental Member

Dr. Curran Crawford (Department of Mechanical Engineering)
Departmental Member

Dr. Pan Agathoklis (Department of Electrical Engineering)
Outside Member

Supervisory Committee

Dr. Afzal Suleman (Mechanical Department)
Supervisor

Dr. Daniela Constantinescu (Mechanical Engineering)
Departmental Member

Dr. Curran Crawford (Mechanical Engineering)
Departmental Member

Dr. Pan Agathoklis (Electrical and Computer Engineering)
Outside Member

ABSTRACT

Structural Health Monitoring (SHM) through adequate damage detection and prediction of the remaining useful life of structures is a major area of interest in the aerospace community, where the growing maintenance costs can reduce the operational life of flight vehicles. The objective of a SHM system with an advanced diagnostic capability is to gradually replace current schedule-based maintenance tasks, where components are inspected following a pre-established number of cycles using condition-based maintenance, or are maintained prior to attaining an insufficient remaining useful life, based on specified confidence bounds. The research challenge is to obtain a reliable method for determining damage existence and respective location during its initial growth state as a component of an early warning system.

In this thesis, an SHM system based on Lamb waves is proposed. A damage detection algorithm based on the comparison between the damaged structural state and a reference state has been developed. The detection algorithm, based on discrete signals correlation, was tested and improved by incorporating statistical methods and domain division techniques. Two SHM system architectures, namely the sensor network and phased array system were designed, implemented and tested.

A visualization method based on the superposition of solutions obtained from a test set was implemented. Tests executed with multiple damage, representing surface and through-the-thickness holes and cracks were performed. The proposed SHM systems using Lamb waves were able to reliably detect holes of 1 mm holes in aluminum and 1.5 mm in composite plates with great confidence.

TABLE OF CONTENTS

LIST OF TABLES

LIST OF FIGURES

LIST OF ACRONYMS

2D-FFT	*Two-Dimensional Fast Fourier Transform*
AGS	*Advanced Grid Structure*
A-Wave	*First anti-symmetrical Lamb wave mode*
CLoVER	*Composite Long-range Variable-direction Emitting Radar*
CWT	*Continuous Wavelet*
DWT	*Discrete Wavelet*
EMAT	*Electro-Magnetic Acoustic Transducers*
FBG	*Fibre Bragg Grating*
FEM	*Finite Element Model*
FFT	*Fast Fourier Transform*
FT	*Fourier Transform*
IC	*Integrated Circuit*
IDT	*Interdigital Transducer*
Laser	*Light Amplification by Stimulated Emission of Radiation*
MEMS	*Micro-Electro-Mechanical System*
NDE	*Non Destructive Evaluation*
NDT	*Non Destructive Test*
PCB	*Printed Circuit Board*
PoD	*Probability of Detection*
PVDF	*Polyvinylidene Fluoride*
PZT	*Lead Zirconate Titanate Piezoelectric*
RMS	*Root Mean Square*
SHM	*Structural Health Monitoring*
S-Wave	*First symmetrical Lamb wave mode*
ToF	*Time of Flight*
VI	*Virtual Instrument*
WT	*Wavelet Transform*
WVD	*Wigner-Ville Distribution*

ACKNOWLEDGMENTS

First of all, I want to express my gratitude to the Portuguese Air Force and Fundação para a Ciência e a Tecnologia (ref: SFRH/BD/20123/2004 – Nationally financed by Programa Operacional Potencial Humano – Quadro de Referência Estratégico Nacional – Ministério da Ciência e da Tecnologia, with the European Social Fund co-financing) for having given me the opportunity to do a PhD in the University of Victoria. Additionally, give my thanks to the Pacific Century Scholarship Program for the Graduate Fellowship.

During my research, I had the valuable support of several people, to whom I am very grateful, in particular: my colleague, Bruno Rocha, for his collaboration and help; Professor Afzal Suleman, for the opportunity of joining his research team and mentoring and Ricardo Paiva, for his valuable support in proof-reading the manuscript.

This work would not have been possible if it were not for the vital experimental assist provided by Sergeant Ramos. I am also grateful to the Aeronautical Laboratory staff, at the Air Force Academy, who directly and indirectly supported this project, namely Col. Pedro Costa, Major Maria Madruga, 1st Lt Luis Félix, Sergeants Fernandes and Bandeiras, and Mrs. Fernanda. Valuable assistance was also provided by Sandra Makosinski and Ian Soutar at the University of Victoria.

Lastly, I would like to express my appreciation to all my family members, my girlfriend Nanete, my nieces Beatriz and Sara and friends, for their permanent support, above all during my absence periods while studying in Canada.

To Nanete,
my brother and best friend João Pedro,
to Elsa and
my lovely nieces Beatriz and Sara.

CHAPTER 1

INTRODUCTION

Presently, aircraft structures are maintained and revised on a scheduled basis. Each aircraft manufacturer establishes, for each model, a strict inspection and revision calendar that must be adhered to firmly. This approach leads to high operational costs. Parts are replaced just because they exceeded their predicted lifetime, while others are inspected without revealing any kind of damage. Related disassembling and assembling processes are also time-consuming, and sometimes unnecessary. In this case, costly aircraft grounding occurs. Furthermore, this approach is not fail-safe. Despite the regular inspections, aircraft structural components can fail without notice or previous warnings. Ideally, it is desirable to install a Structural Health Monitoring (SHM) system on the aircraft to enable damage detection and correction in real-time. Aircraft would be grounded only when necessary, just to replace the damage parts. Additionally, pilots could restrict and control the flight severity depending on these real time warnings.

Some aircrafts are already equipped with equipment that monitors the structural stresses and engine operation. Data is collected when the aircraft lands. Only after the post processing, conclusions are drawn and it may be too late to act. The desire to operate aircraft with a higher safety factor, lesser time in the hangar, higher performance and higher revenues are fuelling the development of new SHM systems and approaches. Other indirect advantage includes the possible reduction of safety factors during the components design process, which can lead to higher payloads and lower fuel consumptions, thus making aviation greener.

There are several approaches currently being proposed and studied, all with the same objective in mind: to develop systems capable of monitoring, in real time, the structural integrity. System capabilities include the detection of damage presence, shape, size, location and growth patterns. As the predictive algorithms for damage growth are already well established, the remaining useful life of the component can be estimated. Another important requirement is that such systems must be reliable and avoid false warnings.

SHM implies that structures need sensors and/or actuators on or embedded in it. Different transducers, signal types and algorithms are available. Thus, a number of different solutions are possible depending on the type of actuator/sensor and monitoring principle.

The current thesis research focuses on Lamb wave-based SHM. A comprehensive study has been carried out, including simple experiments to understand the physics of Lamb wave propagation and its characteristics. The lead-zirconate-titanate piezoelectric (PZT) sensor was selected and it was applied on both *sensor network* and *phased array* architectures.

1.1 Motivation

There are several types of non destructive tests (NDT) being currently used. Depending on the structure, different techniques can be selected and each with its advantages and limitations. The first one is the fact that NDT involves manually inspecting on site disassembled parts of the aircraft. The current state of the art on SHM, including techniques to monitor damage using Lamb waves, are capable of detecting damage size of around 3 mm. Furthermore, no comparison has been reported in the open literature between sensor networks and phased arrays architectures.

The main goal of proposed thesis is to detect damage smaller that 3mm. Capturing damage in an initial state of growth can be of paramount importance to avoid a catastrophic in-flight event. This detection capability would surpass any current traditional NDT technique. Sensor networks and phased arrays are studied extensively in order to better understand their performance and limitations.

1.2 Thesis Layout

The layout of the thesis document is presented in the following way:

Chapter 1 – Introduces the subject of Structural Health Monitoring, the main motivation and proposed contributions to field are outlined, followed by an overview of the layout of the thesis.

Chapter 2 – Summarizes the current aircraft maintenance solutions and traditional non destructive tests available. The various SHM approaches reported in the literature are reported and discussed. A deeper and more detailed discussion is provided on Lamb wave generation and propagation and the respective algorithms and techniques, including the most recent research documented in the open literature.

Chapter 3 – Based on the theoretical knowledge on Lamb waves propagation properties, preliminary numerical and experimental tests are presented. The fundamental research aids in understanding the characteristics of propagation in order to better define the necessary equipment for generation and identification of Lamb waves, and determine the most adequate transducer characteristics. The chapter concludes with a brief introduction to the phased array concept.

Chapter 4 – Damage detection algorithms are explained in detail for sensor networks and phased arrays, both for isotropic and anisotropic materials.

Chapter 5 – A chronological description of the several experimental studies on sensor network based SHM is described, including the design and development of a software tool and the experimental setup.

Chapter 6 – The knowledge gained while studying the sensor network architecture was extended to the phased array based SHM. Using previously developed phased array control equipment, experiments were conducted and some important conclusions are drawn.

Chapter 7 – Finally, the last chapter summarizes the contributions of the thesis to the state of the art in SHM and future work is proposed for further development and application of the Lamb wave based SHM approach.

CHAPTER 2

STRUCTURAL MAINTENANCE CONCEPTS

In order to fully understand the currently available solutions, the latest developments in the area of Lamb wave based solutions are discussed. Available structural assessment methodologies are explained, with particular focus on Lamb waves and its application to damage detection and identification.

2.1 Conventional and Current Maintenance Solutions

In the 1860s, Wohler [1] identified and studied for the first time failure by fatigue in structures. In the early years of aviation, the structures were designed based on the infinite life concept. The idea was to create structures that operated under the fatigue stress limit. This over conservative approach resulted in heavy structures, something which is not desirable in the aerospace industry.

Palmer-Miner [2] research in the field of structural safety led to the safe life approach which established a finite service life, within which there is a low probability of fatigue cracks initiation and growth. This concept remained in use for many years. It did not, however, take rogue flaws due to manufacturing into consideration. Other forms of damage, which could reduce a component's life, such as corrosion or accidental damage were also not accounted for. Frequently, service loads did not comply with the design ones, the damage models were inaccurate and the stress analysis was not comprehensive. These facts lead to multiple accidents, like the ones that occurred during five Havilland COMET flights between May 1952 and January 1954. The last accident happened after the aircraft had flown but 1000 trips, while modelling and simulation tests predicted a safe life of 3060 flights.

Following these events, further studies on crack growth led to the fail safe concept [3]. Here, a structure is allowed to retain a residual strength without repair after failure or partial failure of a primary structural element. It is based on the multiple load path construction and establishes crack stoppers implementation. Under these conditions stress levels promote slow crack propagation, allowing crack detection before it reaches its critical length.

More recently, the damage tolerance approach is in effect [4]. Although essentially an evolution of the fail safe concept, it differs in the way that quantitative crack growth calculations are made assuming worst case scenarios. These include initial manufacturing defects and sensitivity details for crack detection inspection procedures (e.g. a service life until the first inspection is defined). In order to avoid catastrophic failure, an inspection calendar is established for each individual component.

Currently, most components maintenance schedules are based on the damage tolerance approach. Notable exceptions are engine pylons and landing gears on which the safe life concept is employed due to the incorporation of high strength materials in these particular aircraft components.

2.2 Non Destructive Tests

For the damage tolerance approach to be practical, several types of non destructive tests and evaluations should be performed. Because it allows inspection without interfering with a product's final use, NDT provides an excellent balance between quality control and cost-effectiveness. Non Destructive Evaluation (NDE) is another term that is often used interchangeably with NDT. More accurately, however, NDE is used to describe measurements that are more quantitative in nature. For example, an NDE method would not only locate a defect, it would also be used to quantify one or more of its parameters such as size, shape, or orientation.

Current NDE methods fall into one of these categories: Visual and Optical Testing (VT); Liquid Penetrant Testing (LPT); Magnetic Particle Testing (MT); Electromagnetic Testing (ET) or Eddy Current Testing; Radiography (RT); Ultrasonic Testing (UT) [5,6,7,8,9,10]. The choice of the method to be used depends on factors such as the component type, whether it is in assembled or disassembled state, material and the damage type being searched for.

In the present investigation, the most important fact is to know what minimum size of damage can be spotted using such methods. This way, one will be able to assess if the SHM system being developed is adequate. Fig. 2.1 shows the *Probability of Detection* (PoD) using four different methods.

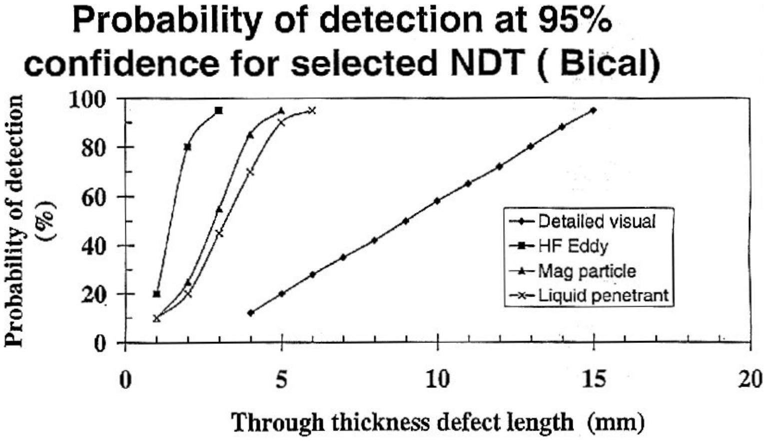

Fig. 2.1: Probability of detection for different NDT techniques [11]

As one can see, defect lengths as small as 3 mm are easily detected. Below that value, the PoD drops abruptly. An SHM system must be able to monitor and find damage lengths inferior to 3 mm with high PoD.

Despite the level of maturity and the significant role played in today's engineering by the techniques described above, they do not guarantee total safety. As mentioned before, these tests are carried out on a schedule basis and provide limited information. As an example, in 2005, an Airbus A310 lost its vertical stabilizer five days after a routine maintenance check [12]. With this in mind, a desirable quality in an SHM system is to be able to monitor structural integrity in a continuous/real time manner.

Financially speaking, an SHM implementation must be cost effective when compared to traditional testing. It has been proved that application of SHM systems may help in reducing a fleet's overall maintenance costs, at least 30% [13].

2.3 Structural Health Monitoring

The desired SHM involves assessing structural integrity through different damage diagnosis stages: detection, location and severity. Ideally, damage prognosis follows, which should give an insight into the remaining useful life of a component [14].

There are several different theoretical fundaments under development that are related to SHM. They vary from low to high frequency methods and acoustic emission.

Low frequency methods look for changes in mass and/or rigidity which manifest themselves in terms of global dynamic property variation (e.g. frequency response) [15].

However, detectable changes only occur for damages affecting, at least, 10% of the monitored area [16]. Despite its insufficient capability for small damage detection, they can easily be applied to complex structures (e.g. severe joint failure).

Considering damage as a localized property variation, more area focused methods were studied. As an example, methods based on the measurement of electrical impedance were developed [17]. Still, lack of detection sensibility exists when flaws are not in the sensors vicinity. Acoustic emission has also been used for damage triangulation and relative growth monitoring [18]. This method is based on the fact that cracks emit acoustic waves when propagating. Its major drawback is the low amplitude of such waves, which results in a poor signal to noise ratio.

Finally, wave based methods have also been used. Waves transmitted through the material interact with damage thus generating reflection waves. The fact that they can be generated upon request attenuates the degradation imposed by environmental noise [19]. Despite the fact that there are several wave types [20] (e.g. Longitudinal, Shear, Rayleigh, Stonely, Creep, Shear horizontal and Love), only Lamb waves will be explored in this work.

Table 2.1 summarizes all available approaches, related mechanism, merits and applications and demerits and limitations.

Table 2.1: SHM approaches [20]

APPROACH	MECHANISM	MERITS AND APPLICATIONS	DEMERITS AND LIMITATIONS
Modal-data-based (eigen-frequency, mode shape and curvature, strain energy, flexibility, sensitivity, damping properties, etc.)	Based on the fact that presence of structural damage reduces structural stiffness, shifts eigen frequencies, and changes frequency response function and mode shapes.	Simple and low cost; particularly effective for detecting large damage in large infrastructure or rotating machinery	Insensitive to small damage or damage growth; difficult to excite high frequencies; need for a large number of measurement points; hypersensitive to boundary and environmental changes.
Electro mechanical/impedance based	Based on the fact that the composition of a system contributes a certain amount to its total electricalmechanical impedance of the system, and presence of damage modifies the impedance in a high frequency range, normally higher than 30 kHz.	Low cost and simple for implementation; particularly effective for detecting defects in planar structures.	Unable to detect damage distant from sensors; not highly accurate; accurate for large damage only.
Static-parameter-based (displacement, strain, etc.)	Based on the observation that presence of damage causes changes in displacement and strain distribution in comparison with benchmark.	Locally sensitive to defects; simple and cost-effective.	Relatively insensitive to undersized damage or the evolution of deterioration.
Acoustic emission	Based on the fact that rapid release of strain energy generates transient waves, whereby presence or growth of damage can be evaluated by capturing damage-emitted acoustic waves.	Able to triangulate damage in different modalities including matrix crack, fibre fracture, delamination, microscopic deformation, welding flaw and corrosion; able to predict damage growth; surface mountable and good coverage.	Prone to contamination by environmental noise; complex signal; for locating damage only; passive method; high damping ratio of the wave, and therefore suitable for small structures only.
Elastic-wave-based (Lamb wave networks, phased arrays, etc.)	Based on the fact that structural damage causes unique wave scattering phenomena and mode conversion, whereby quantitative evaluation of damage can be achieved by scrutinising the wave signals scattered by damage.	Cost-effective, fast and repeatable; able to inspect a large structure in a short time; sensitive to small damage; no need for motion of transducers; low energy consumption; able to detect both surface and internal damage.	Need for sophisticated signal processing due to complex appearance of wave signals, multiple wave modes available simultaneously; difficult to simulate wave propagation in complex structures; strong dependence on prior models or benchmark signals.

2.4 Lamb Wave Approach

2.4.1 Background

The original studies on waves, by Lord Rayleigh, date back to 1889 [21]. In 1917, Horace Lamb published his classic analysis and description of acoustic waves, which included Lamb waves [22]. These waves can exist in thin plate-like structures with parallel free boundaries. By 1945, Osborne and Hart noticed that such waves were also present in underwater explosions [23]. In 1950, Mindlin completed a theoretical approach to these types of waves [24]. At the time, all the progress was solely motivated by its medical applications. In 1961, Worlon thought about using Lamb waves for damage detection and hence the basis for a new NDE technique emerged [25]. By 1962, Frederikhad conducted the first experimental study [26].

Given the increased capabilities of nowadays computer systems, signal generation and data acquisition equipment and transducers, deeper and more complex studies in SHM have become possible. The path is then open to realistic Lamb wave applications, in which mitigation of some of today's problems related to structural integrity is sought.

Damage detection by high frequency waves is achieved through the emission of Lamb waves and the gathering of the respective structural responses. It is basically a pulse-echo or pitch-catch scanning method that is mainly applied to beams and plates. Many aerospace systems can be idealized using these basic structural components. As such, they present themselves as good test specimens. The prospective damage types that are prone to this kind of inspection have been summarised by Rose [27].

The capabilities for this class of methods include: inspection of large structures while retaining coating and insulation (e.g. a pipe system under water) and entire cross sectional area of a structure (100% coverage over a fairly long length); no need for complex and costly insertion/rotation devices and for device motion during inspection; exceptional sensitivity to multiple defects with high identification accuracy; small energy consumption and cost-effectiveness [27]. The potential of Lamb wave based SHM methodologies to monitor large metallic aircraft surfaces has been investigated by Dalton, Cawley and Lowe [28].

2.4.2 Lamb Wave Theory

Lamb waves are elastic waves that propagate in a direction parallel to the mid surface of thin plate-like structures with free boundaries. Plates constitute the best specimens for the study of Lamb waves, although these can also propagate in low curvature shells. The main characteristic of interest of such waves is their low amplitude loss during the travel through the structure. They are nonetheless particularly susceptible to interference caused by damage or boundaries.

When Lamb waves are transmitted particles move in one of two possible ways. One is symmetric with respect to the mid plane of the plate and occurs in the so called symmetric modes. Conversely, the other type of movement is anti-symmetric. For each of these two types, several modes may exist so they can be used to assess structural integrity with respect to both internal and surface damages. Each mode has different phase and group velocities, along with unique particle displacement distribution and stress.

The stationary patterns of the first anti-symmetric (A-Wave) and symmetric (S-Wave) modes can be seen on Fig. 2.2. A- or S-Waves modes are defined according to the number of inflection points across the material thickness. In this case, they are designated by A_n and S_n waves, *n* being the wave number.

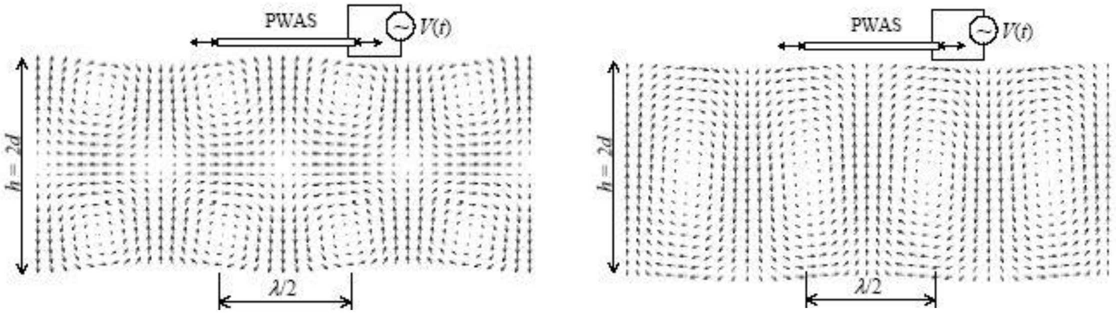

Fig. 2.2: Symmetric wave (S_0) and anti-symmetric wave (A_0) [29]

Observing the two types of waves on Fig. 2.3 it can seen that the S-Wave type essentially produces compression and traction on the upper and lower surfaces, while the mid surface remains unaffected. The A-Wave type produces movement in the normal direction with respect to the propagation direction. The movements of the upper, mid and lower surfaces are in phase.

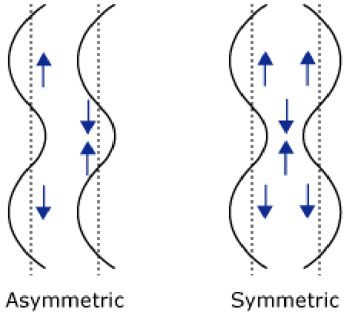

Fig. 2.3: Lamb wave movement [29]

2.4.3 Mathematical Modelling

Consider a thin plate of $2h$ thickness, as seen in Fig. 2.4.

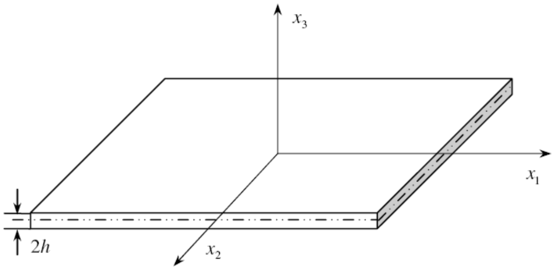

Fig. 2.4: Plate element [20]

Waves can be described by the following equation, in Cartesian tensor form [30]:

$$\mu\, u_{i,jj} + (\lambda + \mu)\, u_{j,ji} + \rho\, f_i = \rho\, \ddot{u}_i \text{, with } i,j = 1,2,3 \tag{2.1}$$

u_i and f_i are the displacement and body forces for the direction x_i. ρ is the density, υ the Poisson’s ratio and μ the shear modulus of the plate. λ is the Lamé constant, which is defined by:

$$\lambda = \frac{2\mu\, \upsilon}{1-2\upsilon} \tag{2.2}$$

Following Helmholtz decomposition [30], equation (2.1) can be separated into longitudinal and transverse governing modes, respectively [20].

$$\frac{\partial^2 \phi}{\partial x_1^2} + \frac{\partial^2 \phi}{\partial x_3^2} = \frac{1}{C_P^2} \frac{\partial^2 \phi}{\partial t^2} \tag{2.3}$$

$$\frac{\partial^2 \psi}{\partial x_1^2} + \frac{\partial^2 \psi}{\partial x_3^2} = \frac{1}{C_S^2} \frac{\partial^2 \psi}{\partial t^2} \tag{2.4}$$

Being C_P and C_S the longitudinal and transverse wave propagation velocities, respectively.

The solutions for equations (2.3) and (2.4) have the form [20]:

$$\phi = \left[A_1 \sin(px_3) + A_2 \cos(px_3)\right] e^{i(kx_1 - \omega t)} \tag{2.5}$$

$$\psi = \left[B_1 \sin(qx_3) + B_2 \cos(qx_3)\right] e^{i(kx_1 - \omega t)} \tag{2.6}$$

Where,

$$p^2 = \frac{\omega^2}{C_P^2} - k^2 \tag{2.7}$$

$$q^2 = \frac{\omega^2}{C_S^2} - k^2 \tag{2.8}$$

$$k = \frac{2\pi}{\lambda_{wave}} \tag{2.9}$$

A and *B* constants can be determined by the boundary conditions. *k*, ω and λ_{wave} are wavenumber, circular frequency and wavelength, respectively.

The displacements in the wave propagation direction and its normal, for the plane strain case, are defined as [20]:

$$u_1 = \frac{\partial \phi}{\partial x_1} - \frac{\partial \psi}{\partial x_3} \tag{2.10}$$

$$u_2 = 0 \tag{2.11}$$

$$u_3 = \frac{\partial \phi}{\partial x_3} + \frac{\partial \psi}{\partial x_1} \tag{2.12}$$

Stress tensor components σ_{31} and σ_{33} are given by [20]:

$$\sigma_{31}=\mu\left(\frac{\partial u_3}{\partial x_1}+\frac{\partial u_1}{\partial x_3}\right) \tag{2.13}$$

$$\sigma_{33}=\lambda\left(\frac{\partial u_1}{\partial x_1}+\frac{\partial u_3}{\partial x_3}\right)+2\mu\frac{\partial u_3}{\partial x_3} \tag{2.14}$$

The applicable boundary conditions are [20]:

$$u(x,t)=u_0(x,t) \tag{2.15}$$

$$t_i=\sigma_{ij}n_j \tag{2.16}$$

$$\sigma_{31}=\sigma_{33}=0 \text{ for } x_3=\pm\frac{d}{2}=\pm h \tag{2.17}$$

From the above, the general Lamb wave equation can be derived [20]:

$$\frac{\tan(qh)}{\tan(ph)}=-\frac{4k^2qp\mu}{(\lambda k^2+\lambda p^2+2\mu p2)(k^2-q^2)} \tag{2.18}$$

Considering that the tangent function can be defined with the sine and cosine functions, it possesses both symmetric and anti-symmetric characteristics. As a result, equation (2.18) can be separated into the two main mode equations [20]:

$$\frac{\tan(qh)}{\tan(ph)}=-\frac{4k^2qp}{(k^2-q^2)^2} \text{ for the symmetric mode} \tag{2.19}$$

$$\frac{\tan(qh)}{\tan(ph)}=-\frac{(k^2-q^2)^2}{4k^2qp} \text{ for the anti-symmetric mode} \tag{2.20}$$

For most practical cases, these equations can only be solved numerically.

2.4.4 Dispersion Curves

The Lamb wave phase velocity, C_L, depends on both frequency and component thickness. Since the wave velocity varies with frequency, the propagation of Lamb waves is essentially dispersive. For a given frequency multiple modes may exist and so the generated wave will be a complex mixture of different modes, therefore hard to analyse. The analytical dispersion curves give an idea of the various existing modes and their velocities for each frequency of excitation. Therefore, it becomes necessary to plot the dispersion curves in order to gain an insight on the dispersive behaviour.

Viktorov [29] developed the following alternative way to solve the abovementioned equations (2.19) and (2.20).

Firstly, it is necessary to calculate the transverse and longitudinal velocities, C_S and C_P [71]:

$$C_S = \sqrt{\frac{E}{2\rho(1+\upsilon)}} \tag{2.21}$$

$$C_P = \sqrt{\frac{\upsilon E}{\rho(1+\upsilon)(1-2\upsilon)} + \frac{E}{\rho(1+\upsilon)}} \tag{2.22}$$

The constants ξ, ζ and $\bar{d}$ are defined as:

$$\xi = \frac{C_S}{C_P} \tag{2.23}$$

$$\zeta = \frac{C_S}{C_L} \tag{2.24}$$

$$\bar{d} = \frac{\omega}{C_S} h \tag{2.25}$$

Where ω is the frequency and h is plate's half thickness.

The dispersion curves may then be calculated through solving the Rayleigh-Lamb frequency equations [71]. For the symmetrical mode the equation is:

$$\frac{\tan\left(\sqrt{1-\zeta^2}\ \bar{d}\right)}{\tan\left(\sqrt{\xi^2-\zeta^2}\ \bar{d}\right)} = 4\ \zeta^2 \sqrt{1-\zeta^2}\ \frac{\sqrt{\xi^2-\zeta^2}}{\left(2\ \zeta^2-1\right)^2} \tag{2.26}$$

For the anti-symmetrical mode it becomes:

$$\frac{\tan\left(\sqrt{1-\zeta^2}\ \bar{d}\right)}{\tan\left(\sqrt{\xi^2-\zeta^2}\ \bar{d}\right)} = \frac{\left(2\ \zeta^2-1\right)^2}{4\ \zeta^2\sqrt{1-\zeta^2}\sqrt{\xi^2-\zeta^2}} \tag{2.27}$$

Both equations admit several roots, corresponding to several anti-symmetrical and symmetrical Lamb wave modes, called S_0, A_0, S_1, A_1, etc.

Fig. 2.5 shows the solutions attained for both modes, in terms of $\frac{\omega}{2\pi}.\bar{d}(= f.d)$ and $\frac{C_L}{C_S}\left(=\frac{c}{cS}\right)$.

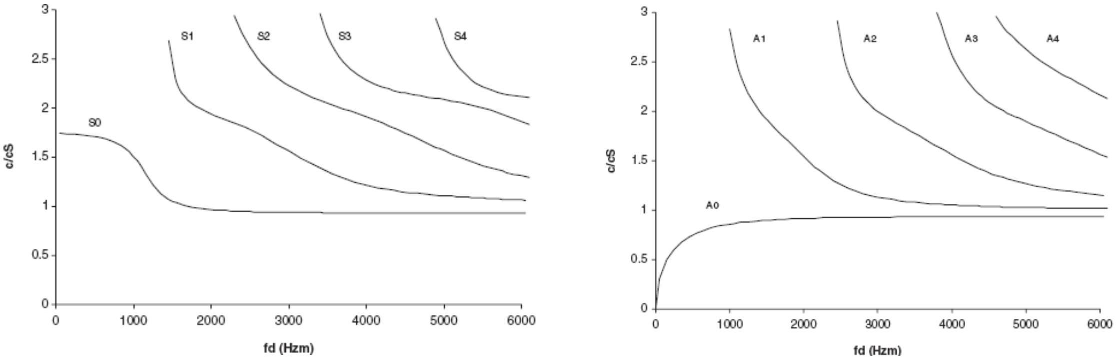

Fig. 2.5: Dispersion curves for several modes [29]

Most SHM Lamb wave based applications have focused on the first symmetric and anti-symmetric modes. An example analysed by Giurgiutiu [29] is given for an aluminum plate with a thickness (*2h*) of 16 mm. Numerically solving the equations for C_L and f, the evolution of their roots can be plotted, as shown in Fig. 2.6. It can be seen how at low frequencies (f <500 KHz), the symmetrical Lamb wave velocity approaches the transverse wave velocity, C_S. In contrast, at high frequencies (f >2500 KHz), the dispersion curves for the S_0 and A_0 modes coalesce.

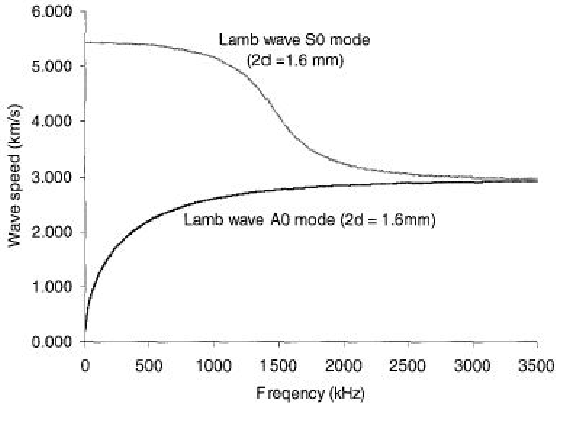

Fig. 2.6: Lamb Waves velocities [29]

It is important to note that Lamb waves travel in packs. In order to characterize the velocity of these packs, a group velocity may be defined, C_g.

$$C_g = C_L^2\left[C_L - (fd)\frac{d\,C_L}{d(fd)}\right]^{-1} \tag{2.28}$$

To simplify the C_g calculation, the following approximation can be established:

$$\frac{d\,C_L}{d\,f} \approx \frac{\Delta\,C_L}{\Delta\,f} \tag{2.29}$$

Fig. 2.7 can be obtained from the solution for C_g as a function of f.

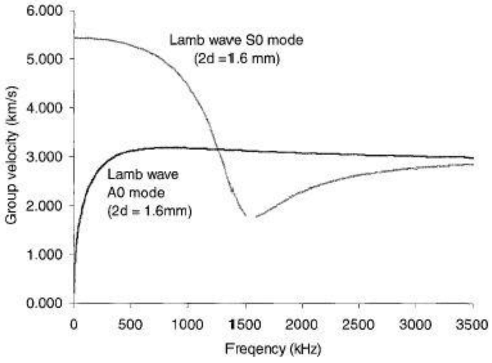

Fig. 2.7: Lamb wave group velocities [29]

In practical terms, these are the velocities that can be measured and used for SHM purposes. Additionally, the frequency regions where velocities present a less dispersive behaviour are the ones to be used. These regions are usually called non-dispersion regions.

2.4.5 State of the Art

Research is being carried out in several fields related to this SHM approach, namely:

- Numerical Modelling, which includes wave modelling, damage modelling and simulated damage detection and sizing;
- Factors which affect wave propagation such as structural reinforcements, temperature and damage orientation and size;
- Generation and acquisition capabilities, involving development of transducers;
- Mode selection and actuation wave shape;

- Implementation techniques through transducer networks and arrays;
- Signal processing in the time or frequency domains, or both;
- Damage detection algorithms.

Since most works do not address one of these aspects in particular, the state of the art regarding each of those is presented below.

Concerning numerical modelling, Lee and Staszewski [31,32] reviewed modeling techniques for Lamb wave based damage identification. Conventional Finite Element Modeling (FEM) and spectral element methods [33] have seen widespread use. Commercial software, such as ANSYS® and PATRAN® are being used nowadays to carry out wave modeling. The FEM approach is truly advantageous for the determination of propagation characteristics in various different media due to its cost-effectiveness. The latest studies range from single mode wave propagation simulation to damage characterization. Galan [34] managed to simulate wave scattering in laminated plates using boundary elements solution. Using spectral finite elements, Ostachowicz [35] presented a robust method capable of detecting damages of small sizes under considerable measurement error.

The amplitude of Lamb waves may suffer changes due to various reasons, even when damage is not present. External conditions such as temperature or humidity are some of them. When it comes to damage detection, this represents a challenge that needs to be addressed. Studies undertaken by Blaise [36,37] indicate that temperature fluctuations can lead to significant changes in Lamb wave amplitude and propagation velocity (up to 50%,for values inside the normal structures operational temperature range). Konstantinidis [38] successfully detected 22 mm damages on a plate and concluded that, in the long term, and due to temperature changes, detection capability decreases. There, an optimal baseline subtraction method is presented as a means to overcome the effects of temperature.

A certain level of immunity to outside stimuli is a desirable trait in an SHM system designed for onboard operation in various weather conditions. However, a similar system designed for ground tests need not be as robust. In other studies it is mentioned that relatively small changes in temperature (±40ºC) should not have a large impact on the outcome of damage detection. Nguyen [39] conducted numerical and experimental trials in order to determine the influence of temperature changes (ranging from -20ºC to 50ºC) and concluded that no significant changes occurred.

Despite the fact that a significant number of aerospace structures can be modeled as plates or low curvature shells, most of them present discontinuities (e.g. stiffeners and rivets). Therefore, another area of study delves on whether or not waves are able to go trough such items since wave amplitude attenuation may occur in such cases. As an example, Zhao [40] conducted several experiments on an aluminum aircraft panel using the S_0 mode. The experiments were conducted while employing an eight sensor network across a 0.1m x 0.1m area in between stringers and damages of 3 mm were successfully detected. However, for larger areas, the attenuation introduced by the presence of stringers (through energy dissipation and wave scattering) resulted in a vastly reduced capability to perform damage detection. In order to study this effect, a different riveted panel was used and a PZT array was installed to generate Lamb waves. Fig. 2.8 shows a schematic of the panel with the PZT array, along with the results obtained for active Case 1 transducers and sensing Case 2 transducers.

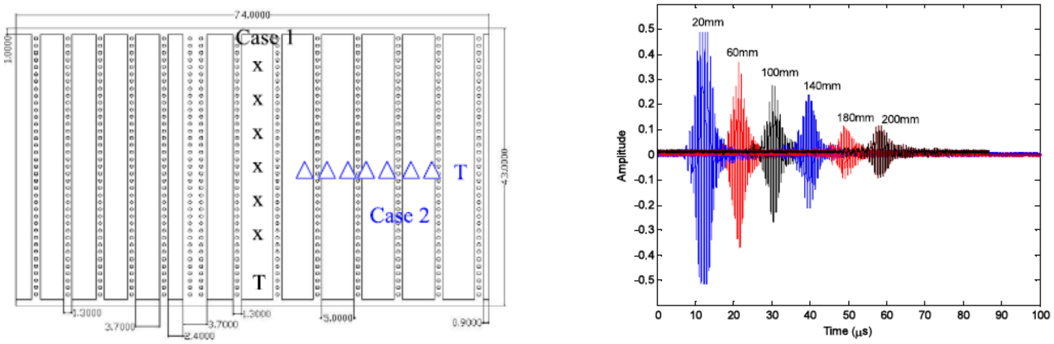

Fig. 2.8: S_0 mode amplitude attenuation [40]

Monnier [41] tested a composite panel with multiple stringers and concluded that the S_0 mode was able to propagate despite all constraints. It was observed that the major amplitude loss occurred as the first stringer was reached, with no significant attenuation at the remaining stringers. Fig. 2.9 presents the composite panel tested and the S_0 energy attenuation evolution.

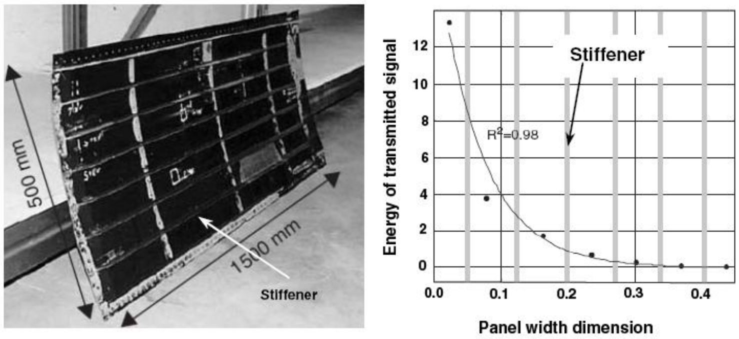

Fig. 2.9: S_0 mode wave energy attenuation [41]

The damage length and orientation with respect to the activated wave, and the relative distance to a certain sensor, play a significant role in damage detection. This particular issue is valid for cracks, which are common structural defects in aerospace components. Lu [42] ran numerical and experimental tests to determine the influence of crack orientation on reflected waves. Several sensors were placed around 20 mm and 40 mm cracks and from the test results it was verified that as the incident angle decreases, reflection also decreases but transmission increases. Additionally, it was found that whenever crack length increases, the amplitude of the reflected wave follows suit, while the transmitted energy decreases. Jin [43] used the A_0 wave to inspect plates with crack lengths of 56 mm by applying Interdigital Transducers (IDT). It was found that for this case, only a very specific IDT positioning allowed correct assessment of crack location, size and shape. Fig. 2.10 shows the scan scheme used.

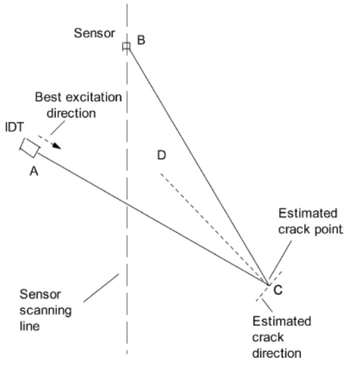

Fig. 2.10: IDT damage scan example [43]

Several functional materials have been studied, developed and applied to Lamb wave emission and acquisition. The most widely used transducers are PZT. Piezoelectricity is the capability to mechanically deform when subjected to an electric charge and vice-versa. In this way PZT can double as sensors and actuators. PZT are usually characterized by their strain constants, d_{ij}, where *i* stands for the polarization direction and *j* the mechanical direction movement. The larger they are, the larger their mechanical deformation will be for a given charge in the corresponding direction. For surface mounted PZT discs, d_{ij} is the most important strain constant. It relates the mechanical deformation on any direction in the plane of the PZT disc when it is polarized along its normal axis [44].

Other solutions involve the use of ultrasonic probes, such as Electro-Magnetic Acoustic Transducers (EMAT). Nevertheless, those cannot be embedded into the structure. Therefore, they do not comply with the desired property of automation in an SHM system.

An emerging field of study in SHM is concerned with reliability. This involves the assessing the durability of actuators [45], their response under extreme conditions such as high temperature, large strains or cryogenic environments [46].

Some of the main advantages of PZT are the fact that they present a wide actuation frequency band, low weight and power requirements. They can also be manufactured in almost every shape or size. The fact that PZT double as actuators and sensors opened the path for their systematic application in SHM [29,47,48]. Size, shape and location must be selected in order to achieve the desired results [49,50]. In [51], numerical simulations and experiments regarding the use of PZT have been conducted in. Giurgiutiu [52] studied the relationship between PZT transducer size and actuation capacity. It was proved that, depending on the size of transducers, there are particular actuation frequencies that maximize actuation amplitude.

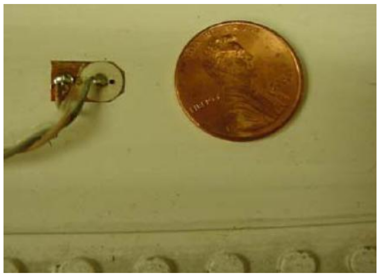

Fig. 2.11: PZT transducer [52]

IDT are also being used. They are composed of Polyvinylidene Fluoride (PVDF) piezoelectric films. The space between each film determines the best actuation frequency, similarly to what happens with PZT. This type of IDT is more flexible and durable than common PZT. However, they perform the best at high frequencies, ranging from 0.5 to 4 MHz, which precludes the usage of lower frequency modes. Additionally, they present a preferred sensing orientation and unidirectional wave activation. Recent developments have led to the manufacturing of IDT which can be moved and rotated [43]. Quek [53] established a performance comparison between PZT and IDT transducers for damage location, concluding that both were able to detect cracks of 3 mm length using the A_0 mode. In this instance, IDT proved to be more sensitive to weld notches due to the fact that they can generate directional waves. Fig. 2.12 shows an IDT produced by KTech® [54].

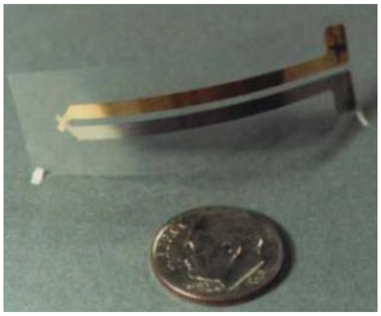

Fig. 2.12: PVDF IDT transducer [54]

Other promising transducers are based on fibre-optics. Due to their nature they may only be employed as sensors; they are sensible to pressure, strain, temperature, electrical field and magnetic field [55]. Until recently, the majority of applications were related with the acquisition of quasi-static measurements. Applications involving dynamic strain readings, vital for Lamb wave based SHM, are presently under development with the introduction of fibre Bragg Grating (FBG) transducers. They are light, thin and, above all, can be embedded into the structure, e.g. during the manufacturing process of composite materials. Still, the fact that environmental conditions influence readings and their dependence on the sensing direction are the main shortcomings of this type of transducer. Nonetheless, in recent developments, some of these limitations were overcome with relative success. Betz [56] undertook damage location experiments with FBG by using rosettes, in order to more accurately determine the wave propagation direction. Damages of 12 mm (hole type) were thereby successfully detected. Fig. 2.13 shows the system used, along with a generic FBG placement and a FBG rosette placement scheme.

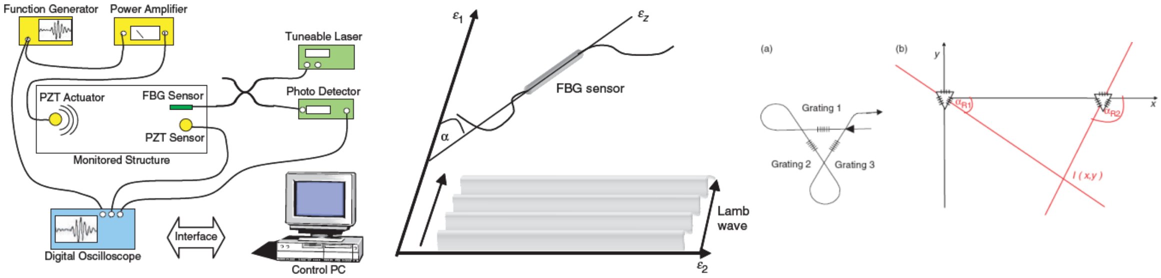

Fig. 2.13: FBG system for Lamb wave based SHM [56]

Not focusing on Lamb wave based systems, Amano [57] tested the implementation of an FBG grid embedded on an Advanced Grid Structure (AGS). By measuring strain changes, upon an impact test, damaged components were successfully detected. Fig. 2.14 shows the FBG system implemented.

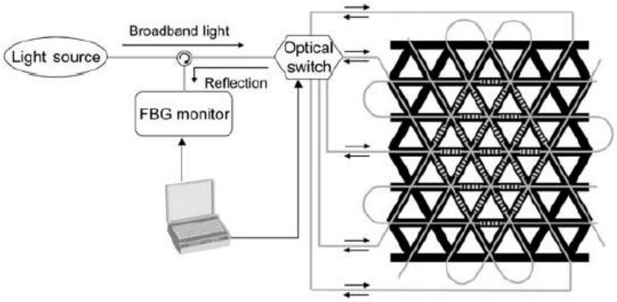

Fig. 2.14: FBG system for strain measurement [57]

Further developments regarding novel transducer technologies include magnetostrictive sensors [58] and IDT based sensors shaped as micro-electro-mechanical systems (MEMS) [59,60].

The actuation of transducers is translated into the excitation of several Lamb wave modes that may coexist. Numerous studies were dedicated to the selection of the most adequate modes to be used. The A_0 and S_0 modes are favoured due to the fact that not only are their propagation velocities quite distinct but also their excitation frequencies fall within the non dispersion region. While S_0 has a higher propagation velocity and is ideal for detecting internal defects, such as delaminations [61,62], A_0 is more sensitive to surface damages. Both modes are sensitive to any kind of damage, however. Furthermore, Rose [63] determined that the S_1 mode is better suited for surface damage detection.

By studying different configurations for sensor positioning, Su [64] concluded that mode separation can be achieved. As a result, it is possible to enhance a desired mode.

Other studies are centered on the most adequate waveform design to be activated. It has been determined that a narrow bandwidth signal, with a finite number of peaks, helps in avoiding wave dispersion. In this way, actuation frequency can be made more precise. Wilcox [65] executed a thorough study on this matter. Essentially, a balance between the wave packet duration and the stimulated frequency precision must be established. In addition, the transducer capability has to be compatible with the desired output.

Two main transducers positioning strategies are presently being implemented: networks and arrays. Irrespective of the positioning strategy, optimum solutions point to a minimum amount of sensors with sufficient sensitivity. The variables accounted for range from sensor type, location, stagger and search area coverage. For the specific case of networks, at least three sensors are necessary to perform triangulation.

There are some studies dedicated to network optimization, such as the one by Chakrabarty [66] where the main objective was to minimize a cost function which weighted both coverage area and financial cost. Staszewski [67] conducted optimization on a network, seeking the best positioning and number of sensors for a direct wave analysis damage assessment. Other authors based their selection of performance measurements on mode shapes [68] and eigenvalues [69] of the structure. Through numerical simulation of wave propagation on an aluminum structure, Lee [70] determined that when seeking for damage by analysing the transmitted wave, sensors should be placed in its vicinity. This constitutes a problem, since damage location is, by definition, unknown. In case the focus is on the reflected wave, sensors are best positioned near the borders of the component.

The second main strategy is based on transducer arrays. This option consists of placing a certain number of transducers which may be aligned in various manners (linear, round, cross, diamond, etc.), depending on the application. Through sequential activation, using a predetermined time delay, a wave front is emitted in a predefined direction. The main advantage of such an approach is the enhancement of the amplitude of the activated wave. By steering the wave front, the test specimen can be scanned for damage, resembling the behaviour of radar. Bao [71] investigated this particular type of arrangement. Using a linear array, by means of simulation and experimental work, the detection of 19 mm cracks was made possible. Fig. 2.15 shows the generated wave travelled distance for each sensor, which will produce a wave front. Fig. 2.16 shows an example of the beam forming and damage scan visualization.

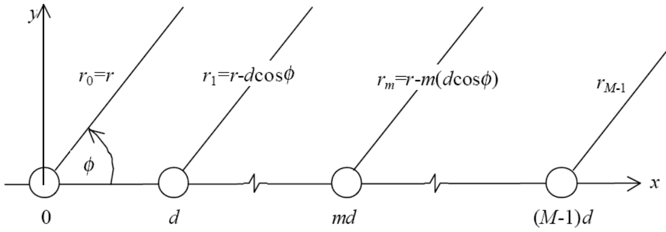

Fig. 2.15: Phased array beam principle [71]

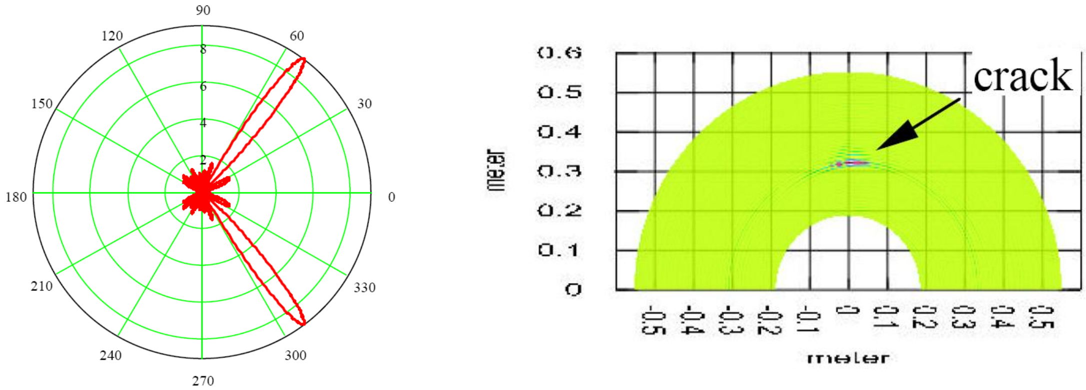

Fig. 2.16: Phased array beam forming and resulting damage scan image [71]

Salas [72] developed a new concept of PZT transducer fabrication meant to produce results similar to a phased array. In this case, a transducer unit is composed of eight parts, each of which is responsible for actuation/sensing in a predetermined azimuth range. Analytical and experimental damage detection tests were successfully performed. The main advantages of this type of PZT are its flexibility and conformability to curved shapes, the capability of excitation of multiple modes and independent sensor/actuator role. Fig. 2.17 shows in detail the CLoVER transducer and its composition.

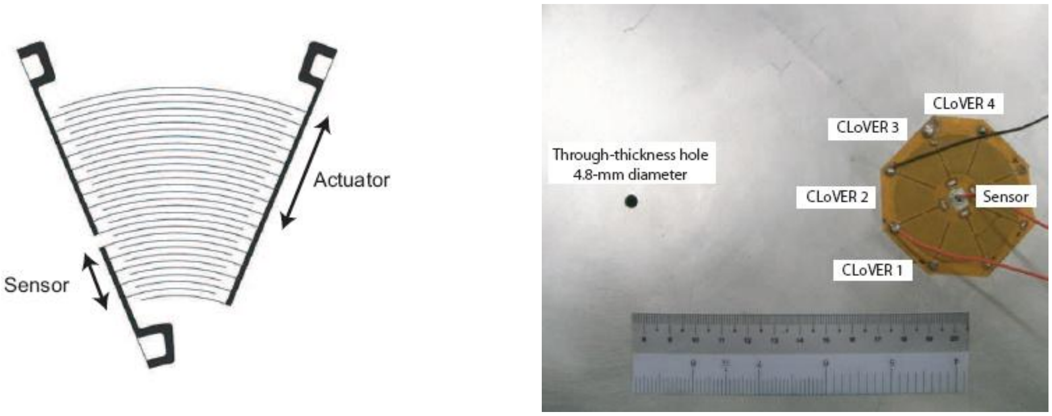

Fig. 2.17: CLoVER transducer [72]

There are a various ways of analysing the signal extracted from the sensors. The raw signal is necessarily acquired in the time domain. Straightforward information can be retrieved from data-series: wave modes, propagation velocities and boundary reflections. Striving for increased signal usability leads to the usage of one of the numerous processing methods available (e.g. root-mean-square (RMS), energy density by Hilbert transform). Further processing is necessary when comparing a baseline signal with a damaged one. Michaels [73] used both normalization and data shifting to synchronize both responses during a four network damage detection experiment on an aluminum plate. Using this approach and with sensors placed near the damages, 6.4 mm holes were successfully detected.

Time reversal can also be used for damage location. This process implies re-emitting the reversed response acquired by a sensor (which then performs as an actuator). Assuming that there is no damage present, the initial transducer should receive a signal very similar to the one initially sent. In so being, baseline and damage comparison is unnecessary. Sohn [74] successfully applied this method for the detection of delamination on a composite panel. On the delaminated plate, the received signal did not match the original one created by the first actuator. This approach also focuses its search on the direct paths established between sensor and actuator pairs. Given this limitation, only relatively high density network grids or 1D specimen can profit from this form of processing. Still, very small damages can be detected. With this methodology, Prada [75] was able to detect damages of 0.4 mm on a 250 mm diameter isotropic billet, and Xu [76] time reversal approach concluded that single mode tuning is the best way to enable. Fig. 2.18 illustrates how time reversal works.

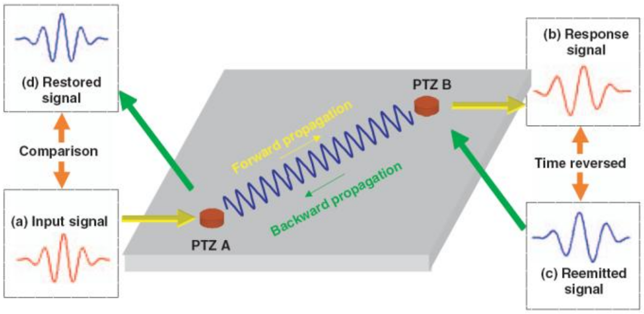

Fig. 2.18: Time reversal example [74]

In a frequency domain analysis, the main purpose is mode identification. Post-processing options include Fourier Transform (FT), and either one or two dimensional Fast Fourier Transform (FFT). The latter is particularly effective in identifying the different modes. Experimental results were obtained by Gomez-Ullate [77] using 2D-FFT on data collected using a vibrometer. Gao [78] carried out a similar experiment using laser scanning of a copper plate which allows generated modes to be detected (Fig. 2.19 summarizes the results). The mechanical properties of the plate were also calculated based on the modes identified.

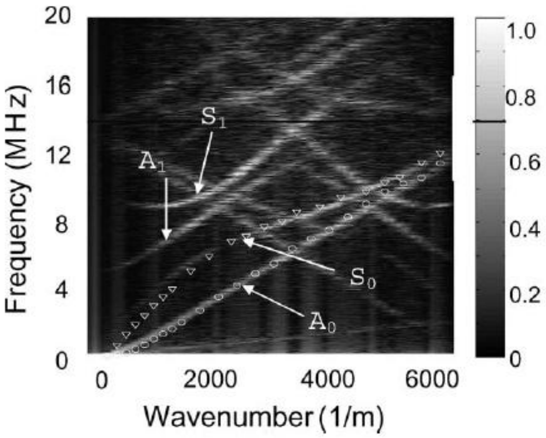

Fig. 2.19: Lamb wave modes detection using laser scanning [78]

Joint time frequency domain analysis can be achieved by a short-time Fourier Transform, Wigner-Ville Distribution (WVD) and Wavelet Transform (WT). These methods encompass both time and frequency variation along the time response. Paget [79] conducted an experimental impact test on a composite panel where WT was used to decompose the time-series data received from the transducers. Three levels of impact energy were applied to a specimen and this was reflected in the WT coefficients.

In order to assess damage severity, damage indices are used. These may only be used to assess the structural health state, based on the comparison of certain features. Most of the methods based on damage indices account for the fact that as time lag between direct wave arrival to sensor and damage wave detection increases, there is also a positive change in attenuation. For the time domain a damage index can be calculated based on signal magnitude [80], whereas in the frequency domain and combined domains, RMS magnitude [41,81,82], among others, have been used.

Following signal acquisition and respective post-processing, qualitative and/or quantitative characteristic features related to damage presence can be extracted. Different algorithms for damage location can be applied depending on the strategy chosen: networks or arrays. Under the topic of PZT networks there are two available approaches. The first one, "Pitch and Catch" is based on the detection of the scattered wave caused by damage presence directly between actuator and sensor pair. For an estimate of the damage location, damage index integration is frequently used. The simplest approach implies creating a sufficiently dense grid, established by the numerous direct paths between every actuator/sensor pair available. Ihn [83] successfully tested this principle on an Airbus aircraft panel using two strips of eighteen PZT each, as seen on Fig. 2.20, and computed damage indices based on measurements of wave energy. Cracks starting at 4 mm were detected and it was concluded that damage length was linearly proportional to damage index calculated. Time reversal can also be used. The intersection of at least two concurrent paths, established by different pairs of actuators, whose time reversal test failed, indicates the damage location. The relationship between the reversibility evaluations can be used to estimate damage size.

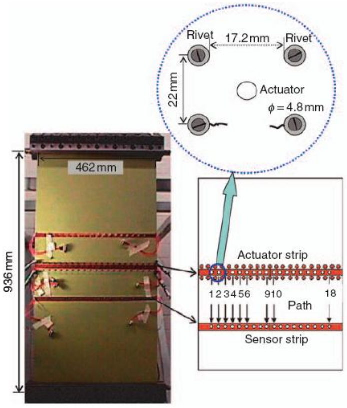

Fig. 2.20: "Pitch and catch" test example [83]

The Pulse-Echo technique relies on the fact that the active wave echo produced by the damage can be retrieved by the sensors. This approach requires a smaller number of transducers in comparison with the "Pitch and Catch" technique. Notwithstanding, it has its own shortcomings, which are related with the possibility of information loss due to the long distances travelled by the active wave. Raghavan [84] carried out tests for damage location this technique, successfully locating holes as small as 5 mm in diameter (Fig. 2.21). During this study temperature influence was also taken into consideration and it was found that both PZT performance and bonding material can be affected. This study also puts forward the idea that an offset variation occurs for the sensed time domain response when the ambient temperature lies in 20ºC-80ºC range. However, for higher temperatures (80ºC-130ºC), activated wave peak amplitude is significantly decreased. Also, the variations for Young modulus and phase velocity are shown on Fig. 2.22.

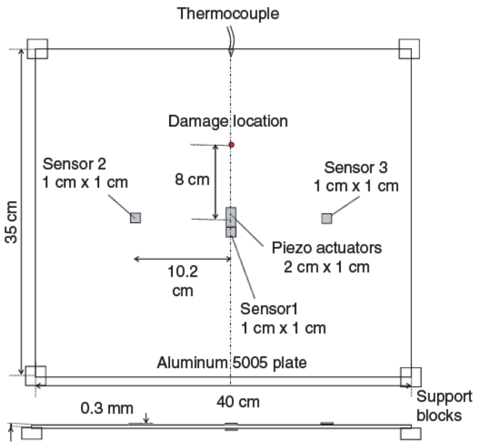

Fig. 2.21: Network experiment setup [84]

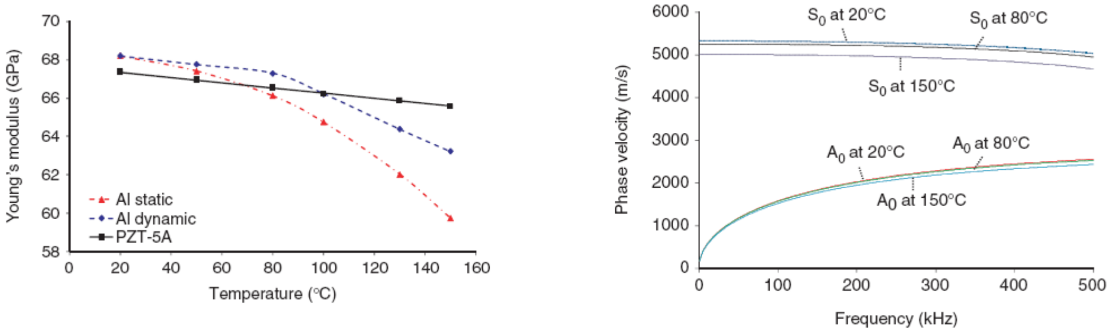

Fig. 2.22: Young modulus and phase velocity progress under temperature variation [84]

For both "Pitch-Catch" and Pulse-Echo techniques, the Time of Flight (ToF) parameter is frequently used. ToF is defined as the difference between the time at which the damage interaction occurred and the time at which the active wave was generated. Knowing the propagation velocity of the activated mode and the ToF, allows the determination of the region where damage is located. For the particular case of Pulse-Echo, using at least three sensors enables the use of triangulation methods.

Another available method is the migration technique. It is based on a geophysical method that has been in use for the last fifty years to detect seismic epicentres and does not require a baseline. Some investigators are exploring the viability of the application of such a method. Wang [85] studied its implementation to a quasi-isotropic composite panel with two distinct delaminations. There are three basic steps necessary: first, the active wave propagation is calculated step by step; second, the sensed response is time reversed and its corresponding propagation is also calculated step by step; finally, for each step, the resulting wave fields are superimposed. Fig. 2.23 exemplifies the visualization of results obtained with this technique. In this particular case, two 0.1 m x 0.1 m delaminations were identified. If damage is present, it will be sensed as a wave generator. This is based on Huygens' Principle which states that damage behaves as a source.

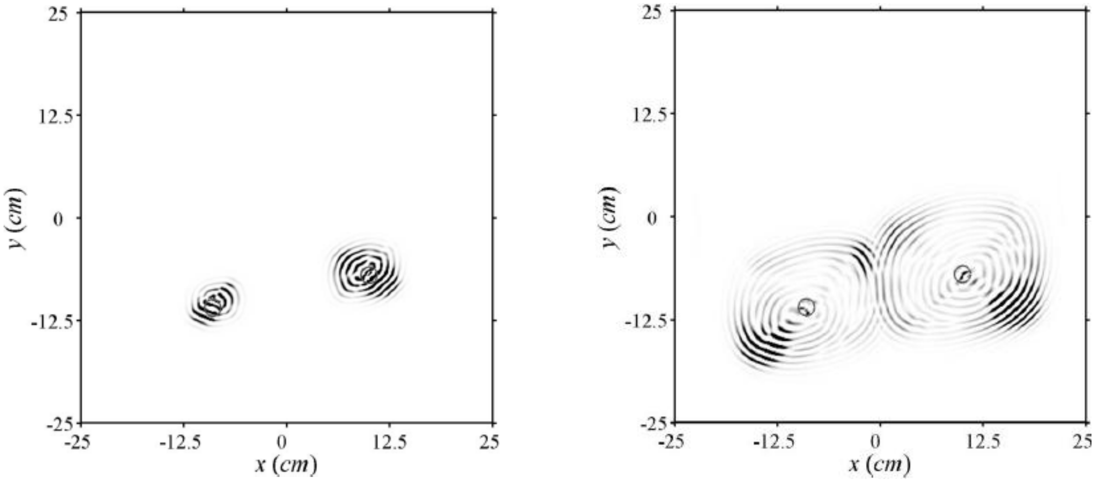

Fig. 2.23: Migration technique [85]

For phased array the Pulse-Echo technique is commonly used. Thus, every approach previously mentioned for PZT networks can also be applied in this case. The main difference is that damage location azimuth is pre-determined by the steering factor. Thus, if the ToF of the echo is determined for a certain azimuth and the propagation velocity is known, the damage location can be pinpointed.

Linear arrays, when placed in the middle of a panel, mirror the damage. To mitigate this issue, different shapes for phased arrays have been studied. Malinowski [86] investigated a star-shaped array using spectral elements, with promising results. The simulated transducers positioning and damage detection can be seen on Fig. 2.24. Using this new configuration the mirroring issue is avoided as selected regions are scanned independently.

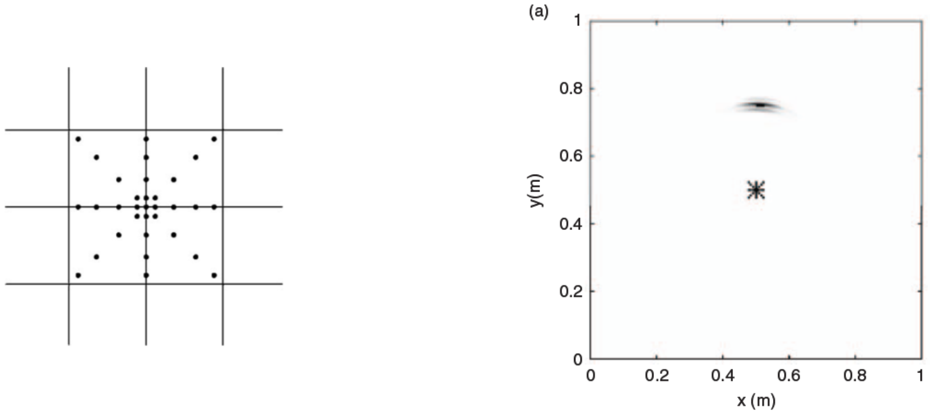

Fig. 2.24: Star shaped array [86]

Analytical and experimental work using PZT for damage location in thin walled structures was presented by Yu [87], and it verses on both isotropic and composite materials. Fig. 2.25 shows some of the experimental setups. Results show that available techniques (networks and phased arrays) using different approaches (Pulse-Echo, "Pitch-Catch" and time-reversal) are suitable for damage detection. The influence of operational and environmental variations is also addressed and it is remarked that bonding materials reliability should be improved. Finally, the advantages of having transducers equipped with wireless processing units are also noted.

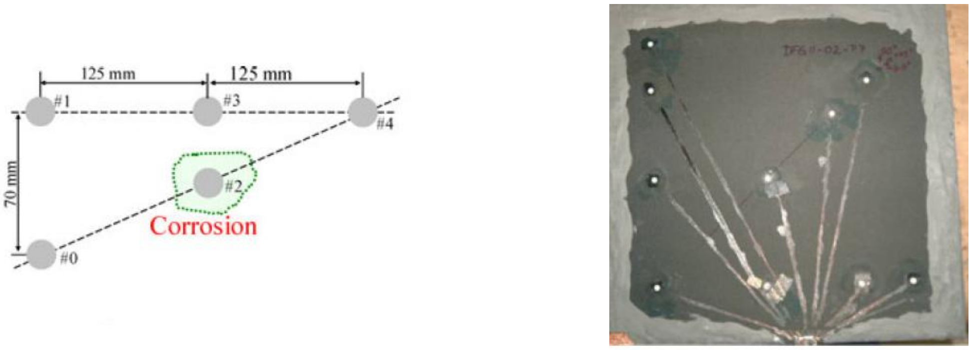

Fig. 2.25: Network (left) and propagation velocity (right) setup experiments [87]

All these different approaches are becoming mature enough to be flight tested. As an example, experiments using several different methodologies were carried out in flight tests using a UK Hawk MK-1A, showing promising results even under harsh flight conditions [88]. Experiments were set on a pod, which was mounted under the left wing. Its schematics can be seen on Fig. 2.26.

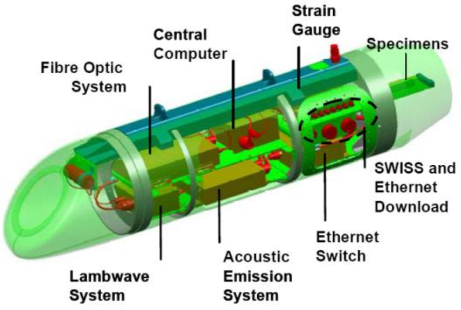

Fig. 2.26: AHMOSII pod [88]

The present literature review shows how extensive the Lamb wave research scope can be. At the moment, the major research focus is on damage location using both networks and phased arrays. Regarding networks, most studies are based on the "Pitch-Catch" strategy, which implies a dense network. Pulse-Echo networks, on the other hand, require a reduced number of sensors but are only effective provided that these are placed in close proximity to the damaged areas (Fig. 2.25 – Left).

Commonly, tests are carried out under favourable conditions. For example, in Fig. 2.25 it can be seen how clay is used to damp boundary reflections, whereas in Fig. 2.21, close range sensors and four simple supports are used. These particular conditions are perfectly valid. In order to increase the knowledge of Lamb wave characteristics, some particular conditions may apply.

The predominant choice of mode in phased arrays is the A-Wave. This is due to the fact that the propagation velocity of symmetric waves is significantly higher, which would require more advanced (and expensive) data acquisition equipment.

In the reviewed literature, no claims are made regarding the detection of damages smaller than 3 mm (for plates).

The main goal of the present work is to attain a better resolution and more precise damage location capability, under no particular boundary conditions. Simultaneously, a minimum number of sensors and a maximization of area coverage are sought. Additionally, and in contrast with previous work, S-Wave based damage location is tested for phased arrays.

CHAPTER 3

FUNDAMENTALS ON LAMB WAVES

Based on the theoretical understanding of Lamb wave propagation and their properties, simple experiments were implemented in order to characterize Lamb wave generation capabilities. This was achieved using the resources available at the beginning of the experimental studies, at the Portuguese Air Force Aeronautical Laboratory.

3.1 Initial Trial Setup

The definition of a working system in this context is one that is capable of accurately actuating the system at an operator-selected frequency and amplitude, while monitoring the progression of this actuation throughout the plate. Finally, being capable of retrieving the acquired data for computational analysis is another desirable trait.

Fig. 3.1: Trial setup

With respect to the hardware, a National Instruments® PXI-607E Analog I/O was employed. This system was able generate and acquire signals with a sampling frequency of 1.25 MS/s. Circular PZT, 25 mm in diameter, specific for out of plane actuation were available. Even though it would be preferable to have PZT designed for in plane actuation, the Poisson effect ensured that in plane actuation was always present. For data acquisition, an Agilent 54622A Oscilloscope was used. The latter possesses an internal memory that can store up to 1000 samples, and a maximum frequency of 100 MS/s per channel.

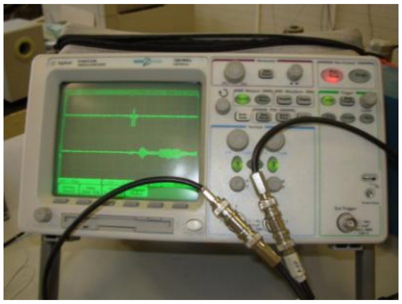

Fig. 3.2: Agilent 54622A oscilloscope

The initial actuation signal was prepared using the LABVIEW® graphical programming software and transmitted to the board using the PXI-607E board. Creating the signal using a programming software and then transmitting it through a data acquisition board (instead of just using a generic function generator box) is preferable since, in that way, the user has a much greater degree of control over the signal being generated. Precise control is then attained in terms of window selection, type of signal, as well as update rate and buffer size. The PXI-607E is connected to a Bayonet Neill-Concelman (BNC) connector board, which contains 10 basic I/O ports, where each can be set for a separate channel, which allows simultaneous actuation/reception of multiple signals.

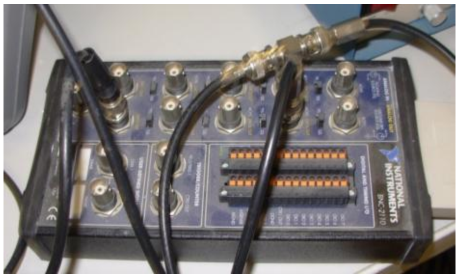

Fig. 3.3: NI BNC board

One important feature of LABVIEW® is that instead of writing actual lines of code, the programmer employs pre-programmed blocks, or functions to construct a virtual instrument (VI). The VI contains two main components: a front panel (e.g. Fig. 3.4), which corresponds to the user interface and a background diagram (e.g. Fig. 3.5 and Fig. 3.6), which is the actual block diagram containing the graphical code.

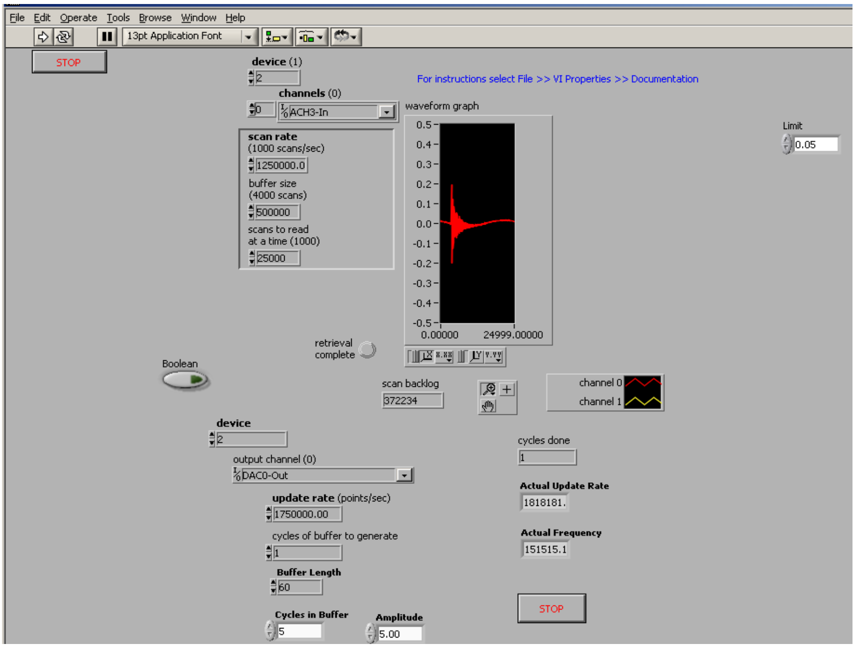

device (1): 2

channels (0): 0 ACH3-In

scan rate (1000 scans/sec): 1250000.0

buffer size (4000 scans): 500000

scans to read at a time (1000): 25000

Limit: 0.05

scan backlog: 372234

device: 2

output channel (0): DAC0-Out

update rate (points/sec): 1750000.00

cycles of buffer to generate: 1

Buffer Length: 60

Cycles in Buffer: 5

Amplitude: 5.00

cycles done: 1

Actual Update Rate: 1818181.

Actual Frequency: 151515.1

Fig. 3.4: LABVIEW® front panel

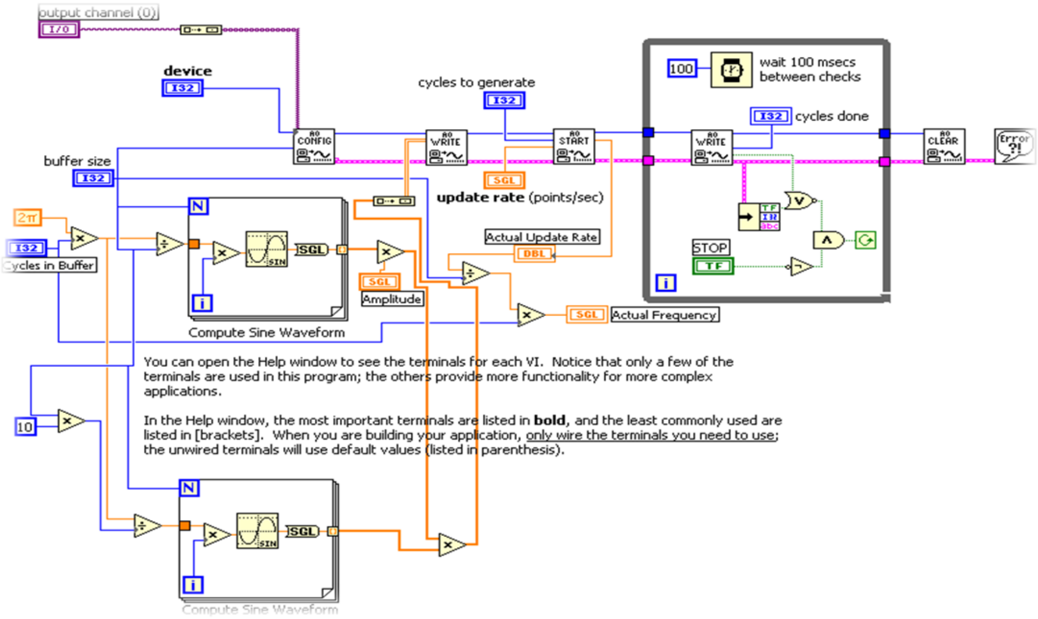

You can open the Help window to see the terminals for each VI. Notice that only a few of the terminals are used in this program; the others provide more functionality for more complex applications.

In the Help window, the most important terminals are listed in **bold**, and the least commonly used are listed in [brackets]. When you are building your application, only wire the terminals you need to use; the unwired terminals will use default values (listed in parenthesis).

Fig. 3.5: LABVIEW® signal generation VI

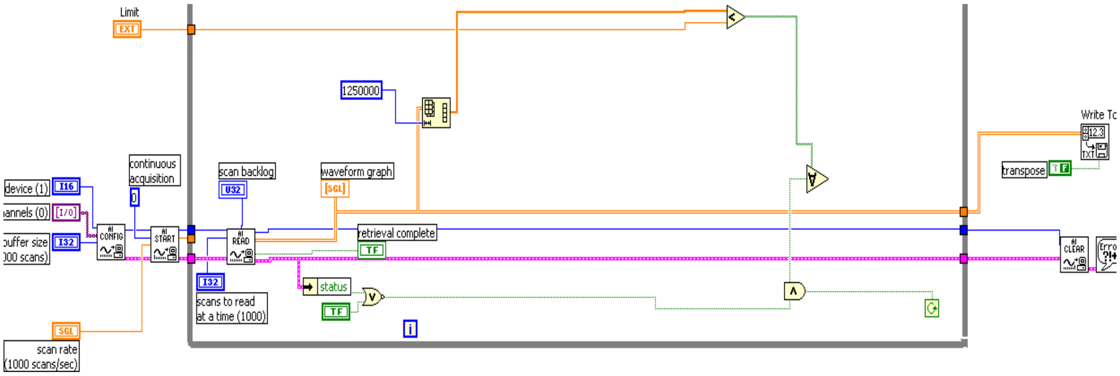

Fig. 3.6: LABVIEW® acquisition VI

The available PZT were glued to an aluminum plate using a type of epoxy specifically developed for this purpose. The top surface of the PZT is divided into two areas (poles), allowing the soldering of two separate wires that drive the electric signal.

The selected plate specimen was 1 m x 1.6 m, with a thickness of 1.6 mm. Two PZT were glued 40 mm apart, their positioning being shown in Fig. 3.7, where an N-S-E-W system of orientation is used. In setting up the PZT positions, the postponing of boundary reflections was accounted for, while guaranteeing that the stagger would be adequate, to allow waves with higher lengths to propagate clearly.

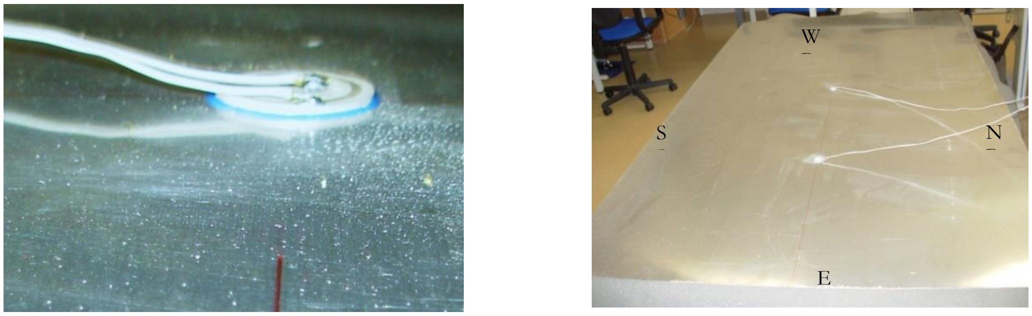

Fig. 3.7: Bonded PZT transducer and aluminum plate with N-S-E-W coordinate system

Several experiments were performed using this setup. In these, typical Hanning-window actuation wave frequencies were experimented with. Also, simulated damage using point masses at selected locations was introduced.

Fig. 3.8 depicts the arrival of the direct S-Wave followed by the expected boundary reflections. The actuation signal degradation with frequency increase is pretty clear, showing the lack of capability of the hardware in use at the time.

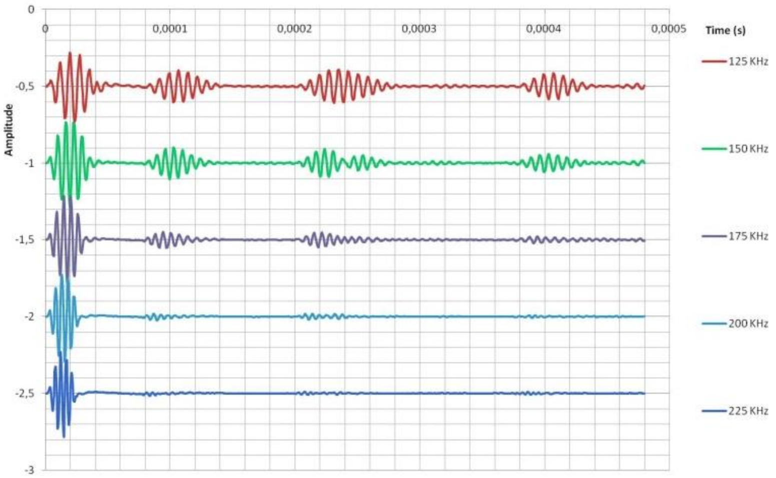

Fig. 3.8: Frequency scan and boundary reflections

For the 125 KHz actuation frequency, arrival times of boundary reflections, distance travelled by the wave and velocity estimation are shown in Table 3.1.

Table 3.1: Expected boundary reflection times

	North	***East***	***South***	***West***
Time (s)	$2.05\text{x}10^{-4}$	$2.29\text{x}10^{-4}$	$2.05\text{x}10^{-4}$	$3.80\text{x}10^{-4}$
Distance (m)	1.077	1.200	1.077	2
Velocity (m/s)	5254	5240	5254	5263

This data was useful to validate the expected symmetrical wave propagation velocity, which was determined to be approximately 5250m/s. Upon inspection of Fig. 2.6, (produced for a similar plate) it can be verified that the value computed for the velocity is indeed correct and ensures positive identification of the S-Wave.

3.1.1 Lessons Learned

The development of software capable of outputting an actuation signal and acquiring the resultant response was completed using the LABVIEW® graphical software. The initial reflection patterns were studied and helped in determining the frequency range necessary for proper actuation. Using the data gathered, the S-Wave was positively identified, based on its boundary reflections.

The main difficulties this initial research was faced with stemmed from the limitations of the hardware. The frequencies necessary to achieve a clear actuation and reception are in the hundreds of KHz range, and the hardware used herein was only capable of a maximum of 150 KHz. The use of frequencies above 150 KHz with this hardware resulted in a steady degradation of the excitation signal, eventually leading to unreliable responses. Another source of difficulty was the fact that only one board was being used for both actuation and reception, presenting cross talk issues. Moreover, since the sampling frequency of the board was limited to 1.25 MS/s, and following a desirable anti-aliasing rule of ten times the signal frequency, at the most it would allow the monitoring of a maximum frequency of 125 KHz, which was clearly insufficient.

The maximum amplitude achievable for the direct S-Wave acquired signal was around 140 KHz, for the PZT in use. According to the literature [52], higher actuation frequencies demand lower PZT sizes. This particular issue will be detailed in section 3.5.

In summary, the first set of accomplishments included: the successful generation of Lamb Wave, including the identification of both A- and S Waves; the determination of propagation velocities which were consistent with the expected ones and the successful identification of boundary reflections.

Damage simulation through mass addition did not succeed. Despite multiple efforts to place different types of surface damage on the plate in a multitude of locations, no change in the reflectivity pattern was observed. This means that in order to see damage reflections, actual physical damage should be present.

Also, another important accomplishment achieved during this phase was the successful determination of the physical limitations of the hardware. This is crucial since data acquisition reliability could only be ensured at low actuation frequencies. More importantly, the experiments allowed insight into what characteristics would be desirable in future systems.

3.2 Experimental Setup Definition

Upon running several experiments using the trial setup, it was possible to determine the desired hardware and software requirements for the next step. In essence, the hardware should be able to work at high sampling frequencies and possess enough memory to store all the necessary data corresponding to the test time, with a suitable precision.

An NI PXI-5421 100 MS/s Arbitrary Waveform Generator 16 bit 8 MB was acquired. On the data acquisition side, a NI PXI-5105 60 MS/s 12 Bit 8 Channels with Simultaneous Sampling Oscilloscope was employed. These two boards are mounted on a NI PXI-1033 chassis that connects to a laptop computer using a PCI-Express card slot. These last two were chosen so that they would not hamper the performance of the two NI boards.

With regard to the software, LABVIEW® was replaced by the NI SIGNAL EXPRESS suite. The latter is more user friendly, allows the management of the actuation generation in a straightforward manner, data gathering and saving as well as some signal processing. At the same time, it carries a visual module that allows real time monitoring of actuation and response signals.

PZT were replaced by smaller diameter versions with the same circular shape. Their smaller size favours the move to the generation of higher frequency actuation waves, which possess lower wavelengths.

The previous aluminum plate was replaced by a 1m x 1m with 2 mm thickness one.

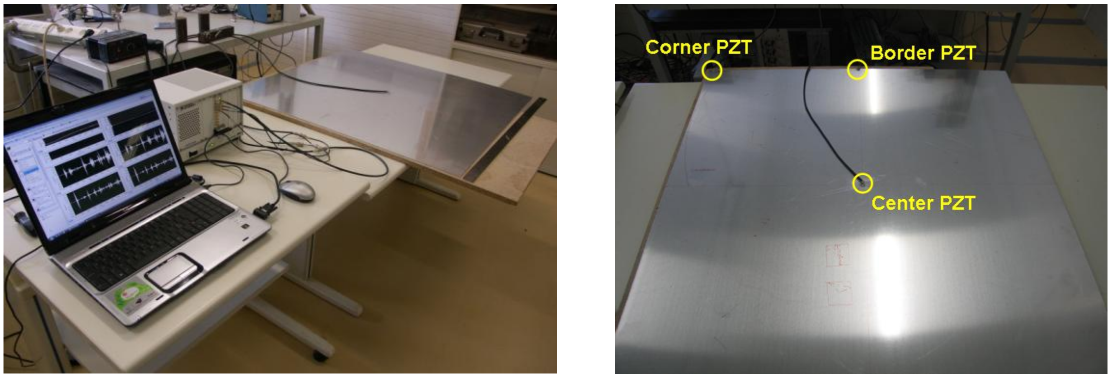

Fig. 3.9: Experimental setup

The criteria for the plate dimensions and PZT positioning changed. With the first set the main goal was to generate Lamb waves, check their propagation velocities and perform a crosscheck using boundary expected reflections. To do that, only two PZT were necessary and they had to be placed far enough from the borders. Also, the plate was laid on a foam layer to attenuate any possible interference from the support contact. The second setup incorporates more concern for real applications. The plate is simply supported on a rigid support and in this way it is more subject to outside interference. One PZT was glued at the middle, in order to be available for any scanning. For damage location, a triangulation algorithm must be applied. This means that a minimum of three sources of data must be accessible. Therefore, two more sensors were installed. These were glued next to the boundaries. On the one hand, this presents a disadvantage since whenever PZT are working as sensors, they will receive two signals almost simultaneously (i.e., the direct signal and its reflection). This represents a slight deterioration in the precise determination of arrival time. On the other hand, the only disturbance will be limited to that data interval. If they were moved further into the plate, boundary reflections would jeopardize the detection of possible damage reflections. This occurs because the possibility of having an overlap between both would then increase. When working as actuators, no significant changes occur.

In order to check if everything was working properly, several tests were undertaken. Initially, the dispersive curves were calculated for the experimental setup (section 3.3). Following, the most adequate actuation function was investigated to suit the needs of the experimental work (section 3.4). Finally, a frequency sweep was made within the hardware limitations. This allowed the determination of the limits of actuation frequency, as well as the optimum one to use (section 3.5). This was attained by observing the sensed signal precision and, more importantly, its amplitude. The actuation frequency was found to be limited to 500 KHz.

3.3 Dispersion Curves

Lamb waves have a dispersive nature, i.e., their propagation velocity depends on the frequency. Naturally, this is a very important concept that needs to be well understood. The factors which influence the dispersive behaviour are the Young modulus, density, Poisson ratio and specimen thickness. For the aluminum plate in use:

Table 3.2: Aluminum plate properties

Property	***Value***
Young modulus (E)	70 GPa
Density (ρ)	2700 Kg/m^3
Poison ratio (v)	0.35
Thickness (h)	0.002 m

From this data it is possible to estimate the transverse and longitudinal velocities, using equations (2.21) and (2.22):

$$C_S = \sqrt{\frac{E}{2\rho(1+\upsilon)}} = 3098.70 \ m/s$$

$$C_P = \sqrt{\frac{\upsilon E}{\rho(1+\upsilon)(1-2\upsilon)} + \frac{E}{\rho(1+\upsilon)}} = 6450.05 \ m/s$$

Solving the Rayleigh-Lamb equations (2.26) and (2.27) for the frequency and Lamb wave velocity, the first modes of A-Wave and S-Wave give:

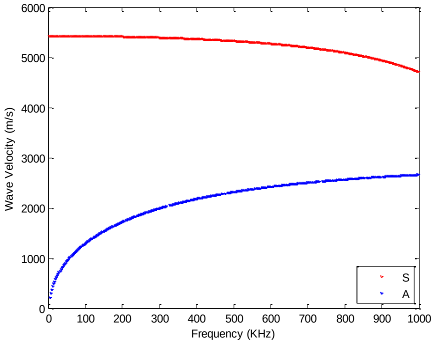

Fig. 3.10: Numerical Lamb wave velocities

Afterwards, group velocity can be calculated (Fig. 3.11), using equation (2.28).

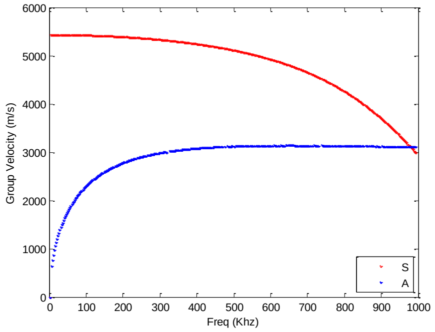

Fig. 3.11: Numerical Lamb wave group velocities

The variation of the estimated group velocities with respect to frequency is coherent with the available literature [52].

It is of interest to evaluate the wavelengths associated to each type of wave.

The evolution of the wavelength with respect to frequency can be estimated through the following equation (also shown in Fig. 3.12):

$$\lambda = \frac{C_g}{f} \tag{3.1}$$

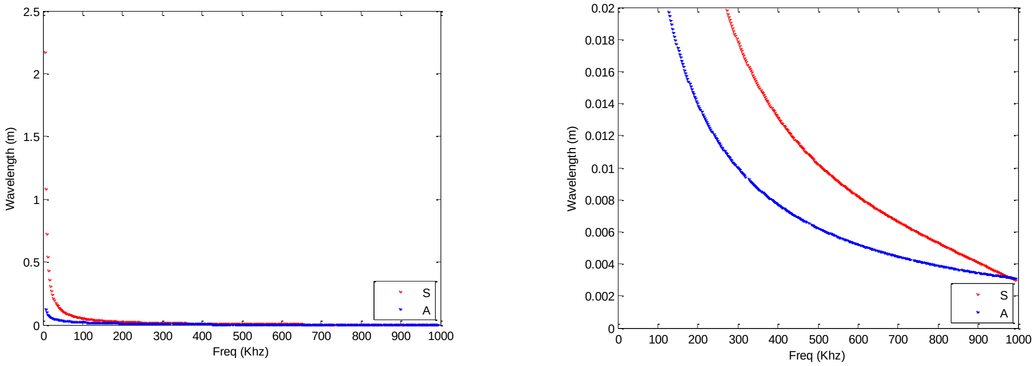

Fig. 3.12: Numerical Lamb wave wavelength

For both types of wave, it is seen that wavelengths decrease with increasing frequency. This is important for the selection of the sensors. In [52], it is stated which sensor size grants the most adequate actuation frequency for each type of wave.

3.4 Actuation Wave Study

Setting up the actuation wave requires a careful study. Several variables must be taken into consideration when defining this function: frequency, number of peaks and the way these are varied over time (non uniform, symmetric or anti-symmetric). These parameters will directly affect how many frequencies will be stimulated, the actuation wavelength that will be produced, whether higher or lower resultant Lamb wave amplitude will be achieved, and also facilitate time definition.

Essentially the two factors playing a major role are the frequency and time definition. Time definition is evaluated by comparison between the shapes of the emitted and sensed waves. A higher definition corresponds to the situation where the sensed wave highly resembles the actuation one. It will be shown that frequency and time definition are conflicting requirements and a compromise must be found in order to find a useful actuation function. Several functions were investigated by observation their time definition and the frequency power spectrum. Some of these will be presented later in this section.

The ideal function possesses the following characteristics: a clearly defined frequency which allows defining the precise velocity of propagation for a specific Lamb wave; a short wavelength, allowing a sharp response while reducing the possibility of overlap between damage and permanent reflections (these include the ones originating at the boundaries and discontinuities).

The actuation wavelength can be calculated as follows:

1. After selecting the actuation frequency, determine the S-Wave propagation group velocity:

$$V_S = F(f) \tag{3.2}$$

2. Determine the period of one cycle:

$$T_1 = \frac{1}{f} \tag{3.3}$$

3. Depending on the number of desired peaks, an *n*-cycle actuation total period is defined:

$$T = n\,T_1 \tag{3.4}$$

4. Determine the generated actuation wavelength as:

$$\lambda = T\,V_S \tag{3.5}$$

Only in very specific conditions will the damage reflection wave appear to be isolated. This problem does not manifest itself in this case. However, if it overlaps with a permanent reflection, constructive or destructive interference will take place. In those cases, it cannot be ensured that the damage reflection is being captured at its beginning, end or somewhere in between. Upon detection, the best solution is to consider that the highest value corresponds to an intermediate time step (neither at the beginning nor at the end of the reflection wavelength).Naturally, for a Pulse-Echo technique it would be preferable to have an instantaneous or quasi-instantaneous actuation, clearly defined in time (e.g. an impulse, a square wave (Fig. 3.13) or a ramp wave (Fig. 3.14)). The wavelength would have to be small, and the reflections would be easily detected. The problem is that such functions stimulate a wide range of frequencies due to the rapid change in shape. Various Lamb wave modes would then be excited, which results in a response that is hard to evaluate.

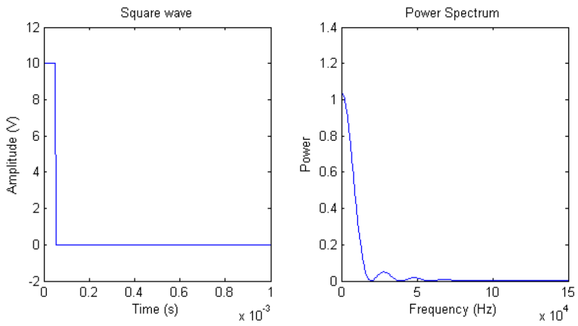

Fig. 3.13: Square actuation wave

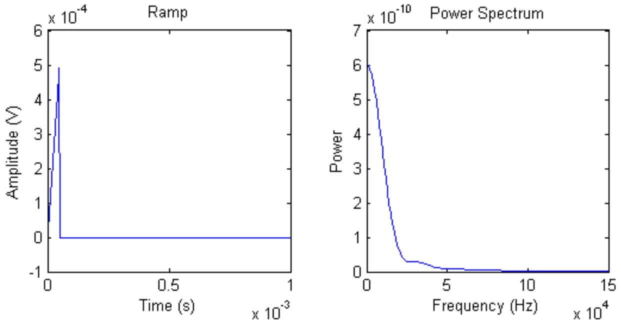

Fig. 3.14: Ramp actuation wave

As for a second approach, and considering that frequency is very important for Lamb waves, a perfect sine can be selected (one cycle). In this way, the frequency is perfectly set but the corresponding response has low amplitude. A possible solution is to define more cycles. Then, the response amplitude increases but at the expense of a larger wavelength. Additionally, undesirable frequencies, called side lobes, are stimulated. These are visible on the FFT spectrum. After several tests it was found that the use of five cycles constituted the best option (Fig. 3.15).

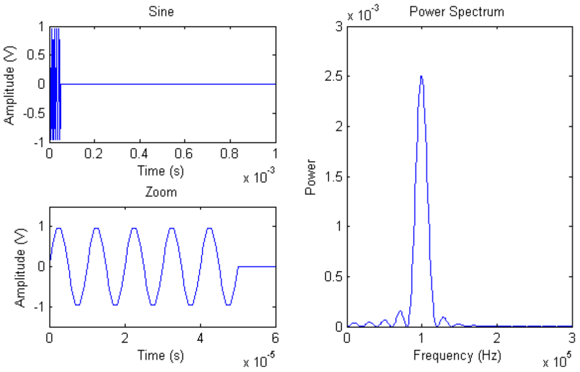

Fig. 3.15: Five sine cycle actuation wave

Fig. 3.16 shows the analysis of the actuation and the sensed response, both in time and frequency domains. The side lobes are clearly visible and time definition is poor.

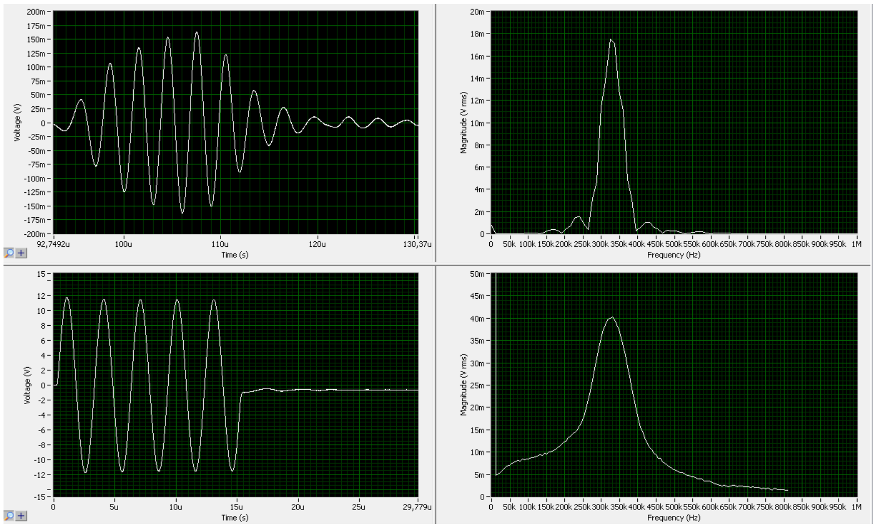

Fig. 3.16: Five sine cycle actuation wave and respective feedback

With this in mind the next task is to improve the time definition of the wave. This can be achieved by modulating the amplitude. In the first of two possible solutions a sine wave is multiplied with another one of lower frequency. The corresponding function can be defined as:

$$f(t) = A\sin(2\ \pi\ f\ t)\ \sin\left(\frac{2\ \pi\ f}{10}t\right) \tag{3.6}$$

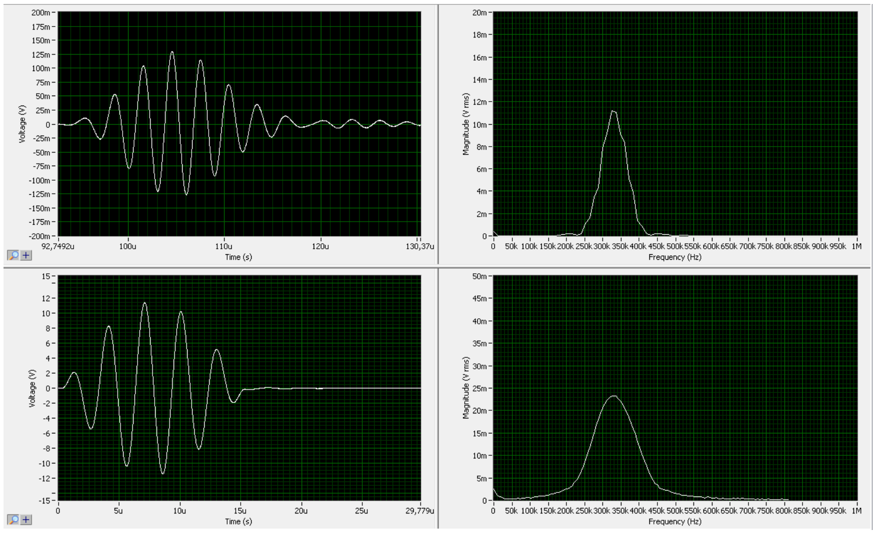

Fig. 3.17: Equation (3.6) actuation wave and respective feedback

A better definition in time is then observed. From the resulting FFT it can be seen that the side lobes almost disappear but the frequency peak is lower and its range gets wider. This is mainly due to the fact that at beginning and end of the actuation phase, the time derivative of the function is clearly nonzero.

The second option studied modulates the first sine with a cosine function:

$$f(t) = A\sin\left(2\ \pi\ f\ t\right)\left(\frac{1}{2} - \left(1 - \cos\left(\frac{2\ \pi\ f}{5}\right)\right)\right) \tag{3.7}$$

This approach allows for a smother transition from/to zero at the beginning/end of the actuation. The results in Fig. 3.18 show that once again the side lobes disappear, and the peak is lower but wider. The positive aspect of this function lies in its time definition, which is superior to that of all the previously mentioned functions.

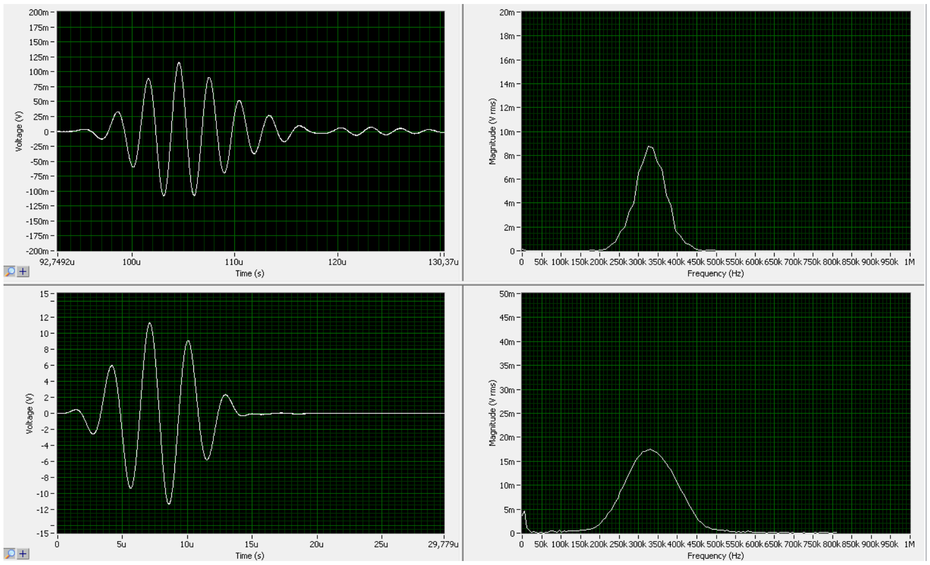

Fig. 3.18: Equation (3.7) actuation wave and respective feedback

Time definition plays a very important role when planning the interpretation of the results. Bearing this in mind, a step by step function was defined using the NI ANALOG GENERATOR. This function produces three peaks instead of five (Fig. 3.19).

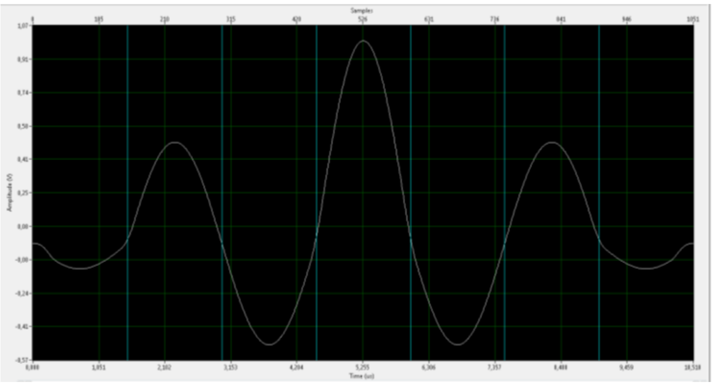

Fig. 3.19: User defined function

Essentially, it uses a sine divided into seven intervals, each of which has a preset amplitude. At the limits of the interval, this function is smoothed in order do avoid frequency dispersion. The results are shown on Fig. 3.20.

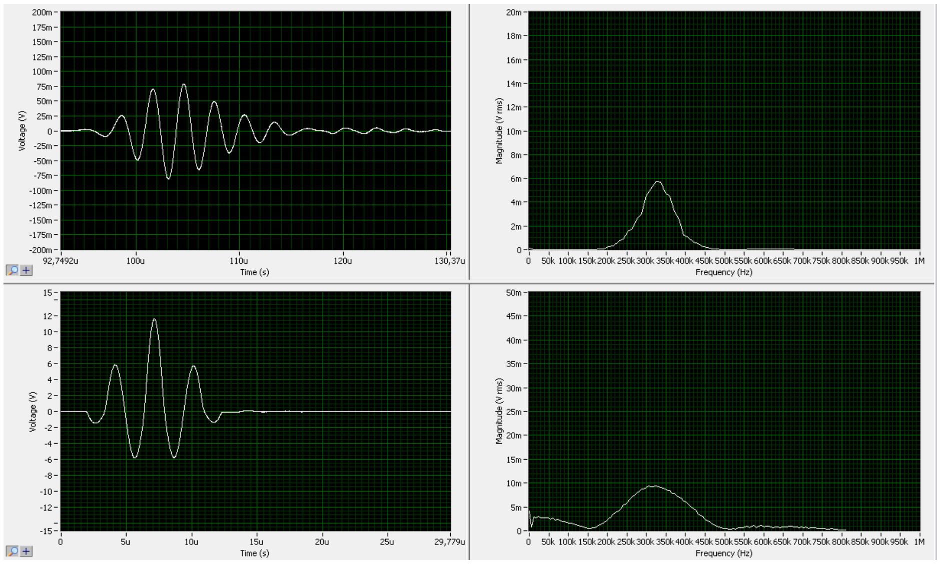

Fig. 3.20: User defined function and respective feedback

Time definition does not undergo a large improvement and, in addition to this, the frequency sharpness and response amplitude are significantly reduced.

These studies allowed a compromise to be found frequency and time definition. The function of choice was the one from equation (3.6) which was smoothed using the NI ANALOG GENERATOR®.

3.5 Actuation Frequency Scan

Actuation frequency scans are useful since they allow checking of which are the best frequencies and wave types to use. They also allow the identification of the A- and S-Waves. Fig. 3.21 shows the acquired signal as a function of the actuation frequency. This test was executed using the center PZT as an actuator and the border PZT as a sensor (see Fig. 3.9).

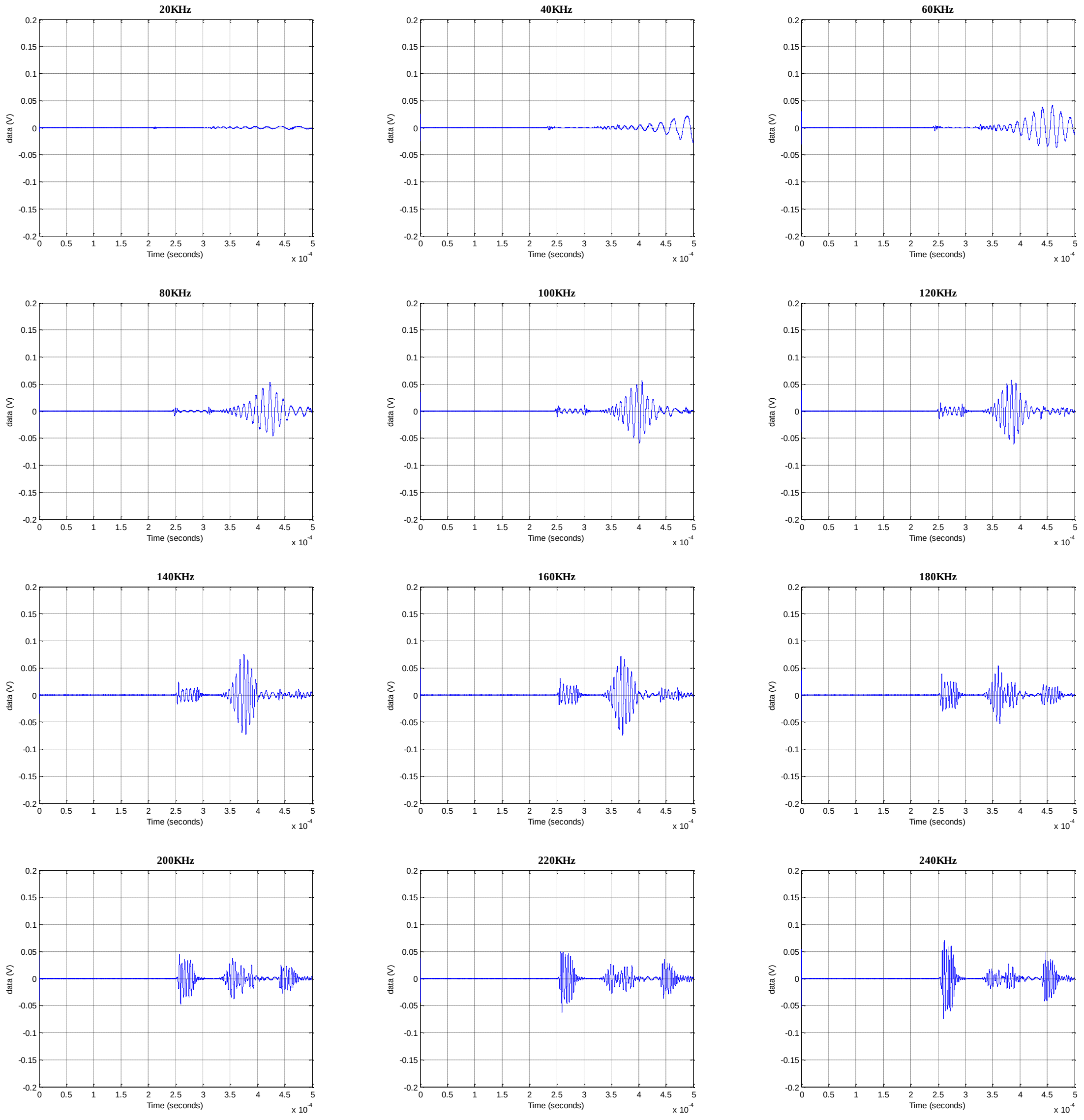

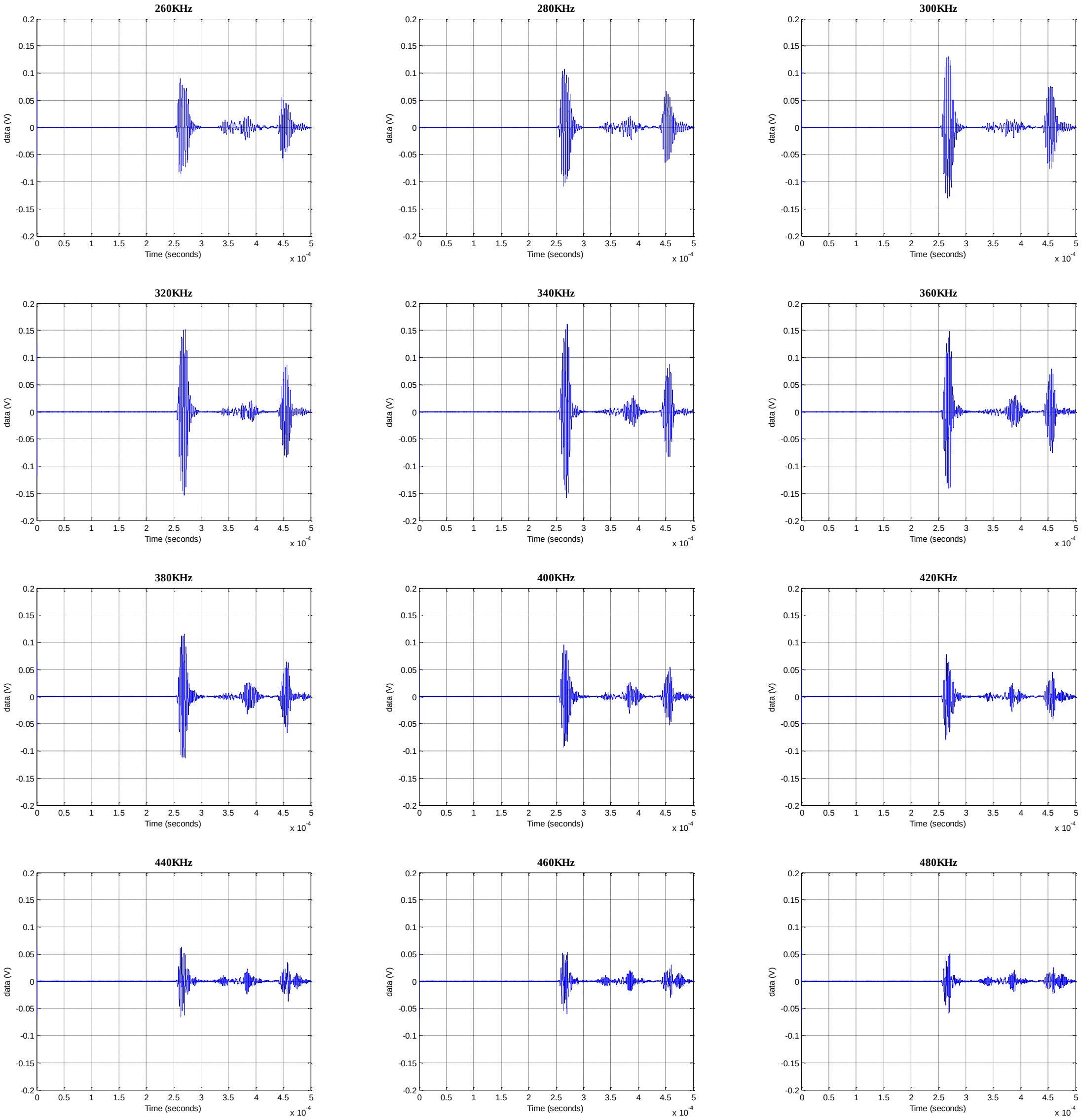

Fig. 3.21: 20 KHz-480 KHz actuation frequency scan

Upon analysis of the above figure, several conclusions may be drawn. Starting with the first test, a slow wave appears from the right. Moving along in the frequency range, the wave moves to the left and increases its amplitude. This is identified as the A-Wave, because it accelerates significantly in the early stages of the frequency increase. It can be seen how its highest amplitude is achieved around 140 KHz after which it drops continuously. Also during this first phase, the S-Wave starts to form at the middle of the time window and it does not present a significant change in velocity, as expected. Still, its propagation velocity is shown to suffer a mild decrease along the scan. In addition, the second highest wave observed (on the right of the time window) corresponds to one boundary reflection of the S-

Wave. It is not until a frequency of 320 KHz is reached that its amplitude increases significantly, reaching a peak at around 340 KHz. The frequencies, at which the S-Wave and A-Wave reach their highest values, are coherent with Giurgiutiu's results [52]. There it is stated that the best Lamb wave excitation and detection is obtained when the PZT length is an odd multiplier of the half wavelength.

The sensors in use have a diameter of 8 mm. From Fig. 3.12, for a wavelength of 16 mm the A- and S-Wave corresponding frequencies are, approximately, 140 KHz and 340 KHz, respectively. These are the frequencies at which their highest amplitudes occur.

Moving to higher frequencies implies lowering the wavelength. This leads to a degradation of the quality in the sensed signal. The only way to avoid such a problem is to use smaller transducers. Transducers selection is therefore the topic of the next section.

3.6 Sensor Selection

The above analysis helps in selecting the proper PZT should the goal be the acquisition of the Lamb wave at its highest possible amplitude. Besides this, for SHM purposes, it is desirable to isolate one wave, as much as possible. In the present work the focus is on the S-Wave and how to enhance it.

In order to do that, a relationship between wavelengths needs to be established. Both S- and A-Waves are clearly read when PZT have a dimension equal to half of their wavelength. In this scenario, if for a certain frequency the S-Wave wavelength is an odd multiple of A-Wave one, both can be easily acquired (no separation). The best solution is to work in the frequency range where this does not take place.

The proposed algorithm for the determination of the relationship between both wavelengths at each particular frequency is as follows:

1. Divide the S-Wave wavelength by the A-Wave wavelength;
2. Halve the result of the above and save the remainder of the division, which should be between zero and two;
3. Calculate the absolute value of the difference between the remainder and one, for each frequency. The most adequate frequencies will be the ones for which this value is near one.

Fig. 3.22 shows the results obtained using the algorithm described above considering the properties from Table 3.2.

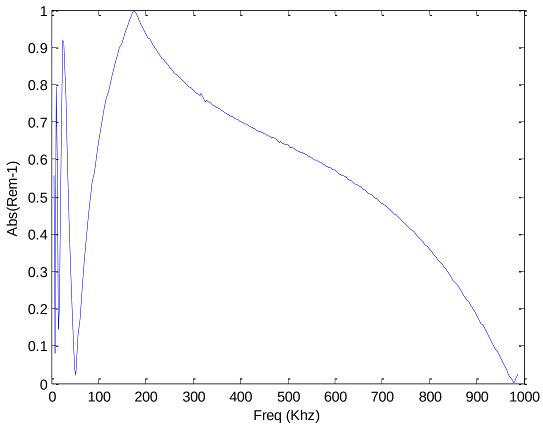

Fig. 3.22: A- and S-Wave wavelengths correlation

The best mode separation is achieved for an actuation frequency of 175 KHz. From the wavelength evolution of both the A- and S-Waves in Fig. 3.12 it can be seen that the proper sensor size selection will be 15.6 mm for S-Wave and 7.7 mm for A-Wave.

Other issues that have to be taken into account are:

- Sensors natural frequency. Actuation frequency should be far enough from it, in order to avoid resonance;
- Sensors size. Bigger sensors will drive high power waves. However, their sensibility will be small due to the fact that higher sizes represent higher inertia. Additionally, for large diameters, localized voltage fields may appear.

For the purposes of the work developed thus far, the principles established here regarding sensor selection were not applied.

3.7 Numerical Simulation

As part of the preliminary studies, a numerical simulation was programmed with the following objectives:

- Check for mechanical wave propagation with and without damage present in a plate;
- Test the damaged and undamaged difference results;

- Understand wave readings acquired by transducers positioned near the corners of the plate.

The first task was to simply simulate the expected echo wave generated by damage. The Finite Element Analysis (FEA) software ANSYS® was used to model the experimental setup.

The aluminum plate is a 1 m x 1 m square, modeled with the same overall properties from Table 3.2. Assuming that the actuators are approximately 10 mm on the side, the mesh size was set to this value. Two elements are used across the thickness. In order to match the experimental constraints as closely as possible, zero displacement in the Z direction was set for the bottom surface nodes. This effectively simulates the contact with the wooden support the actual plate rests on.

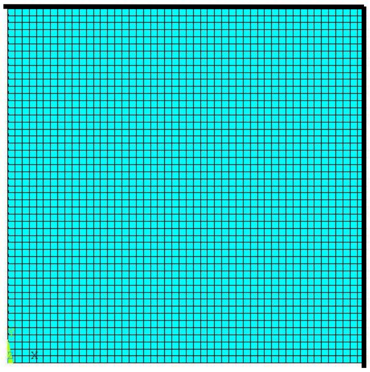

Fig. 3.23: ANSYS® aluminum plate model

To simulate the actuation, the nodes at the upper-right corner, top surface, were prescribed a time varying displacement, matching the stimulus sent to the actuator (note that symmetry is enforced along the axes highlighted in Fig. 3.23). Table 3.3 lists the nodes where this forced displacement is applied. See Fig. 3.24 for details on the position of these nodes.

Table 3.3: ANSYS® actuating nodes selection

Node	***Movement***
2704	*X* direction
2702	*Y* direction
5202	*X* and *Y* direction

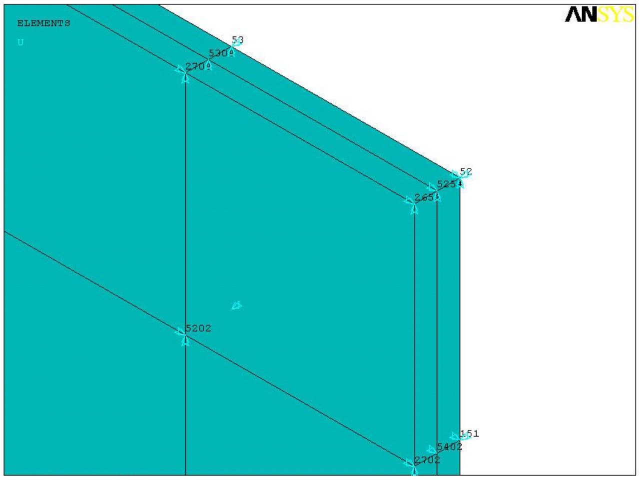

Fig. 3.24: ANSYS® zoom on actuating nodes

The displacement function applied to the nodes was the one defined in equation (3.6). The amplitude reflects the assumption of a strain of 10^{-6} due to the actuation. Several frequencies were tested. In order to clearly see how the wave propagates, a frequency of 100 KHz was chosen matched the expected result

Since this constitutes a transient analysis, it is necessary to determine the period of actuation, which defines the time step.

$$Actuation \quad period = \frac{1}{f} n \text{ , } n \text{ number of function peaks} \tag{3.8}$$

This function is set to have five peaks corresponding to a $5\text{x}10^{-5}$ s actuation period (Fig. 3.25). The sampling frequency, which corresponds to the sub step time, must be high enough to avoid aliasing. A value of 2 MS/s was then set. ANSYS® allows a maximum of 1000 iterations, which limits both the usable simulation time and the sampling frequency. In Fig. 3.26 the wave propagation is shown, based on collected data regarding the Z-displacements of the model.

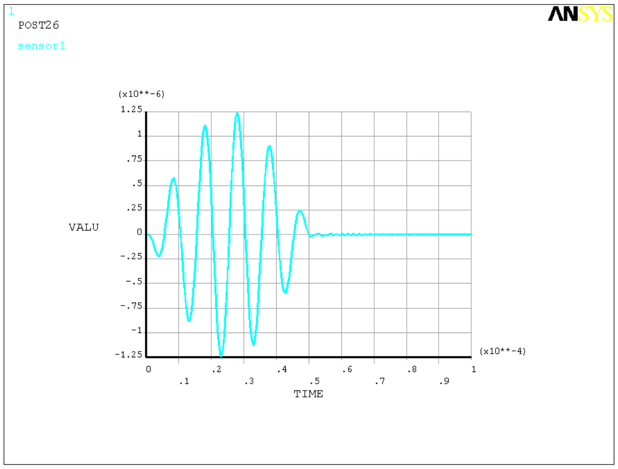

Fig. 3.25: ANSYS® actuating function

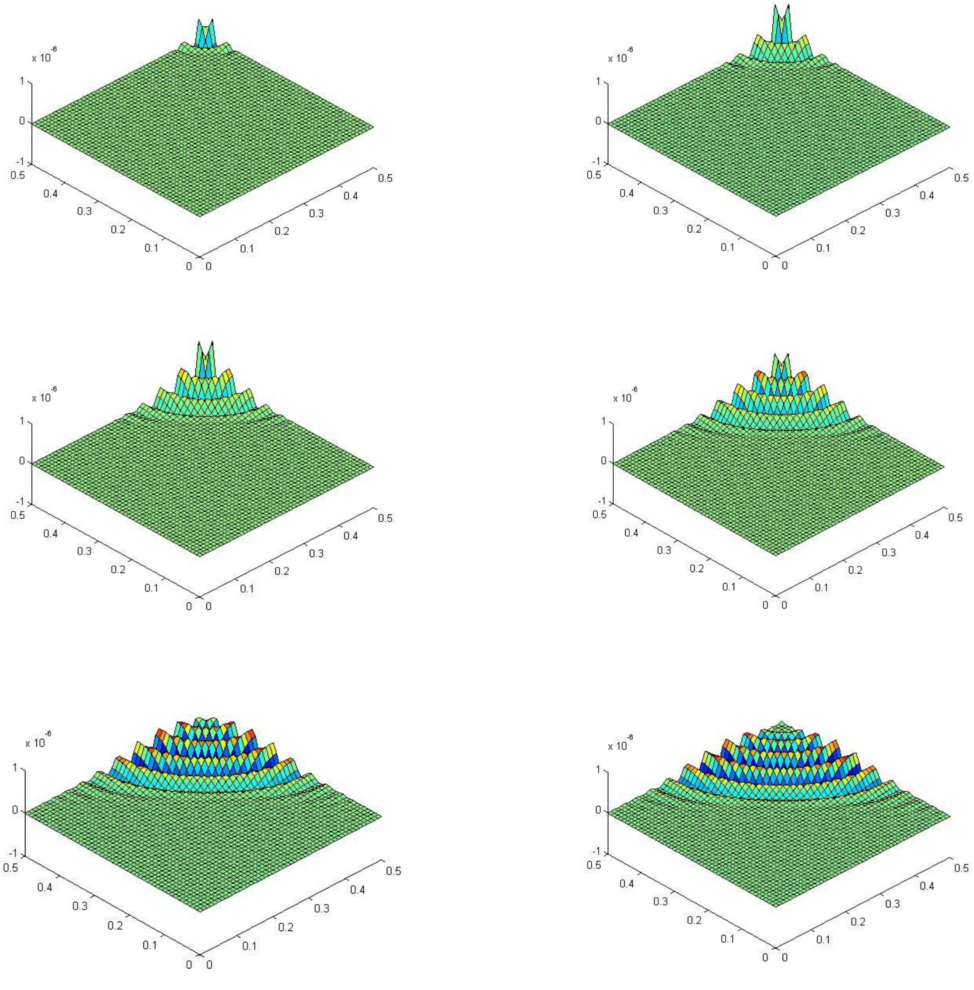

Fig. 3.26: ANSYS® actuation wave propagation

To simulate the damage on the plate, two sets of nodes across the thickness were clamped. This is simple way of modeling a discontinuity in the material. Notwithstanding, it allows the wave response to be checked for the presence of damage. While similar to method previously described, at this instance, the response of the undamaged plate is subtracted to the response of the damage done. This procedure was carried out using MATLAB®. In Fig. 3.27 the results are plotted for several time steps.

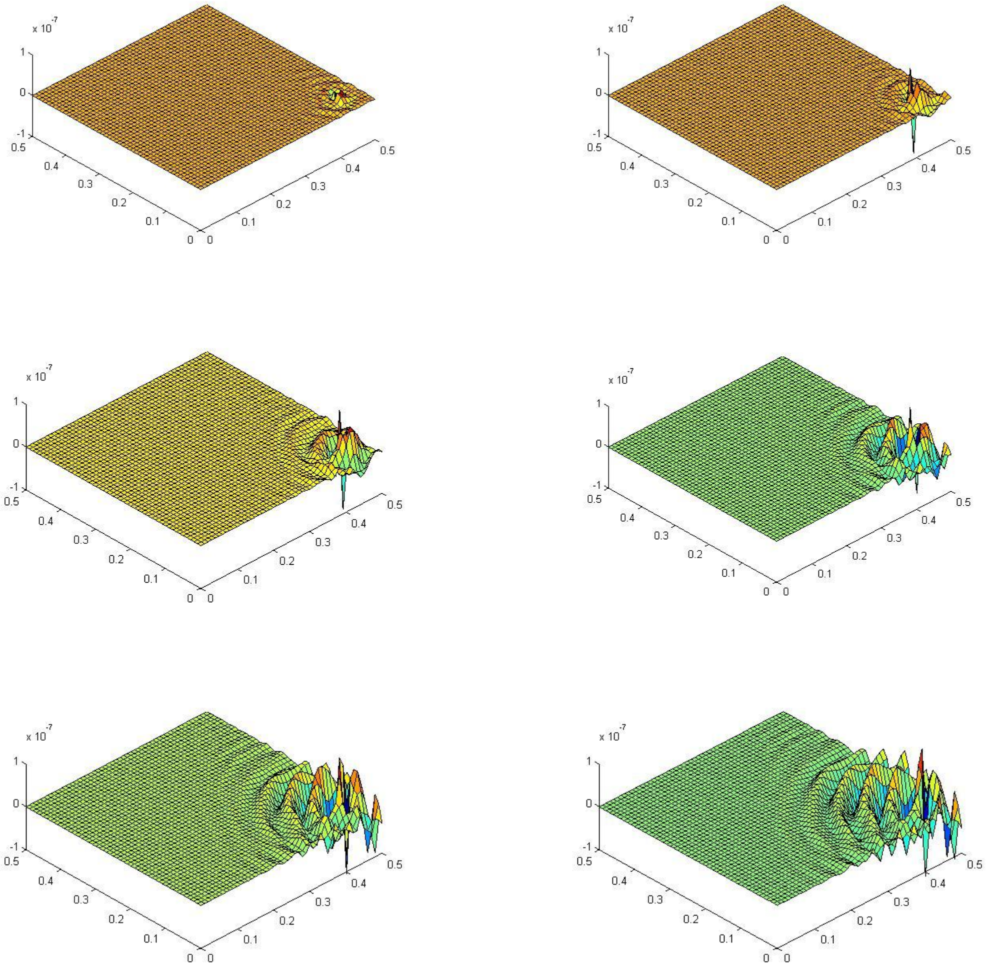

Fig. 3.27: ANSYS® damage wave propagation

From the analysis of these results two basic assumptions can be established. The first one is that the damage will work as a wave generator by itself (naturally of significantly lower amplitude than that of the actuation wave). Secondly, the reflection wave is not uniform for all directions - it seems to present higher amplitude in the direction of the actuator. All other variations most likely result from the fact that interaction with other reflections occurs (e.g.

boundary reflections). Nevertheless, if there is a network of at least three sensors damage detection should be achievable.

Other simulations were performed using different frequencies. The goal here was to verify if such a simple approach was adequate for the validation of dispersion curves. At higher frequencies, inconsistent results were encountered (for instance, different velocities were found along different radial directions, something which is not possible in isotropic media). Still, this numerical approach for echo detection prompted some conclusions on how waves propagate and interact with damage.

During the real life experiments it was observed that the corner PZT received an unexpected response. It was expected that the arrival of the S-Wave would shadow any boundary reflection. However, it was observed that for at least two particular cases this did not happen. The first one occurred for the situation of having the corner PZT as an actuator and the center PZT as a sensor and the second one took place when these roles are reversed. In general, the results were similar to those shown in Fig. 3.28.

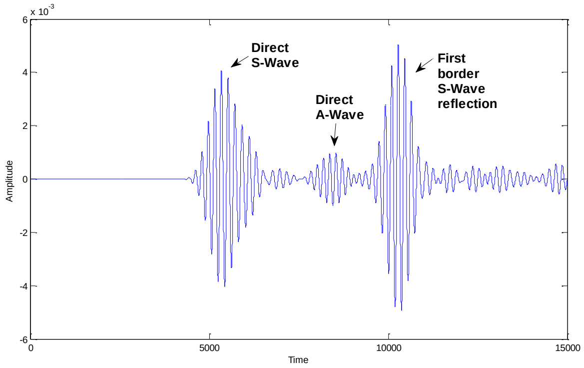

Fig. 3.28: Generic acquired data for the corner PZT

Through simulation, a very similar result was verified for a sensor placed near the origin. Fig. 3.29 shows the simulated direct wave acquisition and its respective first border.

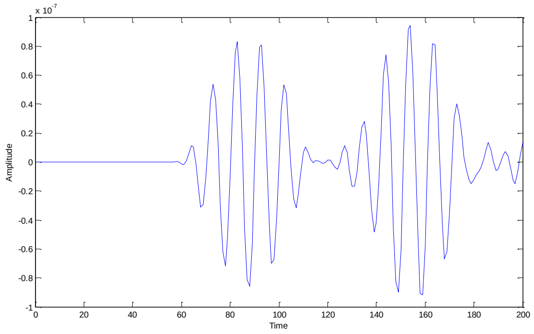

Fig. 3.29: Simulated acquired data for a corner transducer

The main conclusion here is that interaction occurs between the direct wave arrival and the immediate reflections produced at the corner boundaries.

This numerical simulation allowed a better insight into the particularities associated with the positioning of transducers.

3.8 Damage Echo Decay Experiment

It is expected that the amplitude of a damage echo decays when the distance between sensor and damage increases. In the numerical simulations, this became clear. Preliminary experiments were performed by drilling successive holes on a plate, in order to verify this. Knowing the distance to the damage and the wave velocity, the echo wave could be easily identified and measured. Fig. 3.30 shows the echo amplitude reading as a function of distance.

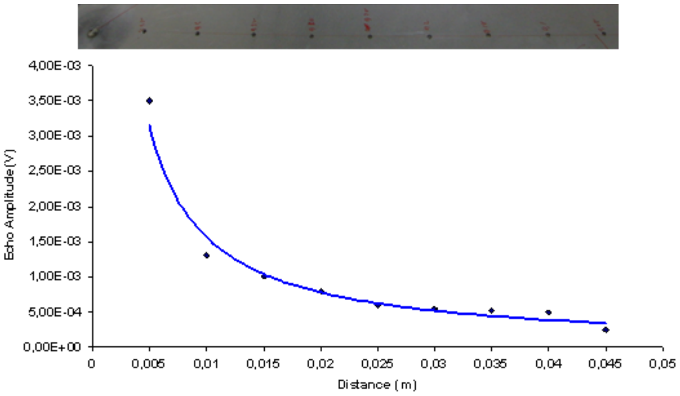

Fig. 3.30: Echo amplitude vs. Damage distance

The overall trend shows that the amplitude is inversely proportional to the distance (*x*):

$$Expected\ Echo\ Amplitude\ (V) = K\ x^{-1} \tag{3.9}$$

In this particular experiment the echo amplitude equation was found to be:

$$V_{EA} = 2.25 \cdot 10^{-5} x^{-1.0068}$$

This function could be useful for damage location. Damage orientation and wave dispersion homogeneity are believed to also have a considerable impact in this function (value of the *K* constant). Therefore, this type of information may only play a complementary role.

3.9 Linear Phased Array Study

Phased arrays were another area of interest in the present work (using the S-Wave). In order to become familiar with this particular SHM technique, some effort was put in the study and simulation of Lamb wave beam forming.

3.9.1 Beam Forming

In order to create a beam in a certain direction θ $(0 < \theta < \pi)$, producing a desired wavefront, the following algorithm is proposed (Fig. 3.31 illustrates the beam forming process):

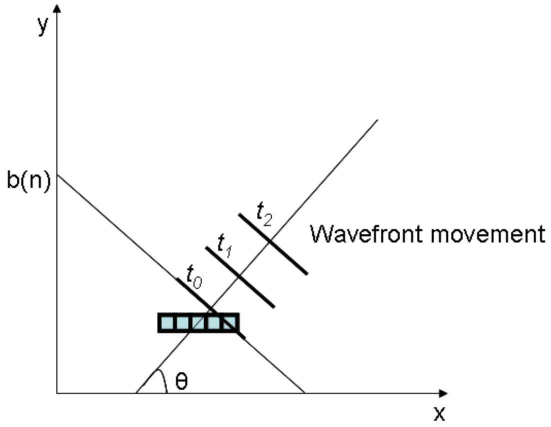

Fig. 3.31: Beam forming scheme

1. Determine which transducer will be part of the wave front. This will determine which will be the first one to be activated. For each transducer in the array at coordinates $(x(i), y(i))$ (where *i* identifies the transducer), a line equation has to be

established. This line crosses the transducer coordinates and is parallel to the wave front. The zero intersect is:

$$b(i) = y(i) - \tan\left(\theta - \frac{\pi}{2}\right) x(i) \text{ , } i=1..n \tag{3.10}$$

2. The sensor with highest *b*, b_{MAX}, will be the last one to be activated. The corresponding line will be used for the next step;
3. Determine the distance between each transducer and the line determined in 1:

$$d(i) = \frac{\left|\tan\left(\theta - \frac{\pi}{2}\right) x(i) - y(i) + b_{MAX}\right|}{\sqrt{\tan^2\left(\theta - \frac{\pi}{2}\right) + 1}} \tag{3.11}$$

4. Determine the trigger time for each transducer, with respect to the last activation, t_0:

$$trigger(i) = t_0 - \frac{d(i)}{C_g} \tag{3.12}$$

3.9.2 Numerical Simulation

Preliminary numerical studies promoted a better understanding of the beam forming process. Additionally, they address other issues, such as the determination of the minimum time required to produce a coherent wavefront.

A MATLAB® code was written that considered the following variables:

- Seven actuator positions;
- Desired beam forming direction;
- Wave velocity.

This code calculates the necessary actuator delays and outputs the desired wavefront. Fig. 3.32 shows a creation of a 90 and a 60 degree beams forming.

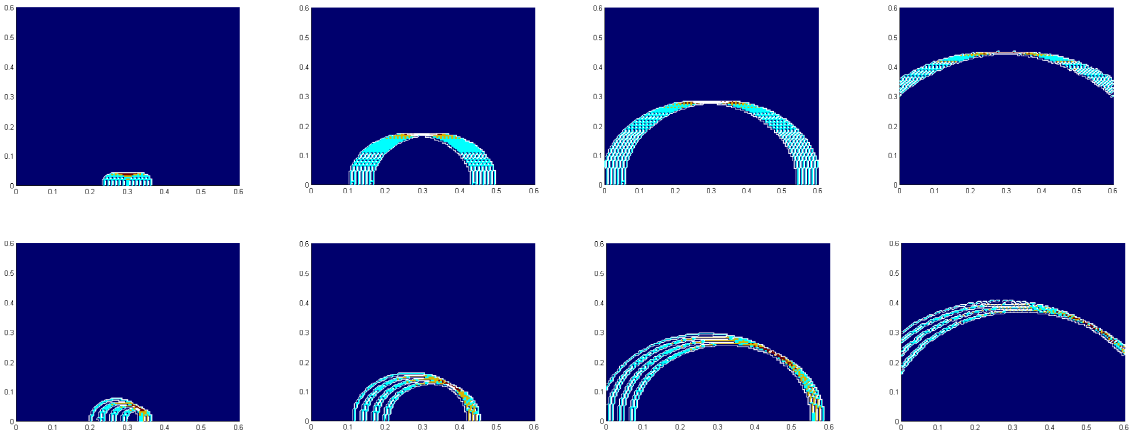

t=n *t=2n* *t=3n* *t=4n*

Fig. 3.32: 90 and 60 degree beam forming simulation

From the figures above it can be seen how the wave front length remains constant. Nevertheless, this length will depend on the orientation and the span of the linear phased array. Its maximum value occurs for 90 degree, when it is equal to the linear array length. On another note, wave superposition increases with time, this reduces amplitude "hot spots" and the "thickness" of the front. Although the wavefront length is kept constant, the amplitude at its edges is expected to increase, as a result of coalescence of the waves, effectively producing a wider front. The relationship between the length of the array and the effective wave front span depends on the aperture ($\Delta\alpha$)[90]:

$$\Delta\alpha = \sin\left(\frac{\pi}{3}\right)\frac{\lambda}{L} \tag{3.13}$$

Where λ is the emitted wavelength and L is the array length. Additionally, the number of actuators and their proximity define the wavefront length and amplitude homogeneity, respectively.

3.9.3 Distance Between Phased Array Transducers

The type of array that is best tailored for investigation is the linear one. In order to determine the most suitable placement of the transducers, their dimensions have to be taken into consideration. Assuming that all transducers are equal in size and circularly shaped, the best actuation frequency depends on their diameter, as hinted before. As a consequence, for each actuation frequency, there will be a corresponding wavelength. This truly determines the proper transducers spacing or pitch.

Wave spreading in directions other than the desired one may occur. This occurrence is called wave side lobes.

The correct choice of actuation frequency and transducer pitch ensures that the goals of a strong beam focusing and minimum unwanted spread are met. Moreover, as the number of elements increases, so better characteristics will be achieved.

In [89], it is stated that pitch must be less than half the Lamb wave wavelength, in order to eliminate the undesired side lobes.

$$Pitch \leq \frac{\lambda}{2} \tag{3.14}$$

8 mm diameter transducers were chosen. Considering that pitch will result from the sum between sensor diameter and inter sensor spacing, the minimum pitch allowed will be 8 mm. Still, sensors must be spaced so as to avoid actuation conflicts at their border. Fig. 2.1 shows half wavelength distribution according to actuation frequency (S-Wave) and some reference pitch values.

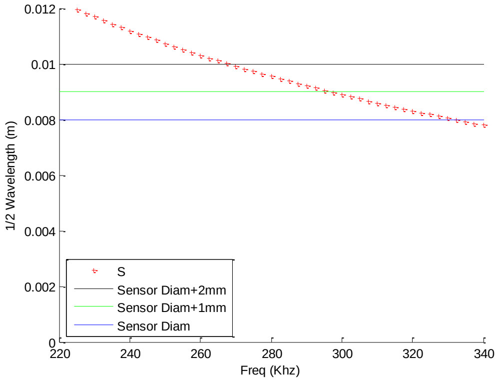

Fig. 3.33: Pitch and half wavelength distribution

It can be seen that for a 9 mm pitch the highest possible actuation frequency will be around 300 KHz. Since the wavelength curve is but theoretical, a tolerance must be enforced in order to avoid the wave side lobes appearance.

CHAPTER 4

DAMAGE DETECTION AND POSITIONING ALGORITHMS

The primary objective of SHM is damage detection. On a higher level it is desired to position the damage itself on the specimen being tested. Wave emission and sensing based methods rely on the assumption that a discontinuity, such as damage, will produce an extra reflection, named echo. Fig. 4.1 shows the echo received by a sensor. Based on the propagation velocity and ToF it is possible to determine the distance between the echo generator and the sensor. With this information, however, one can only determine a region where the damage may be present.

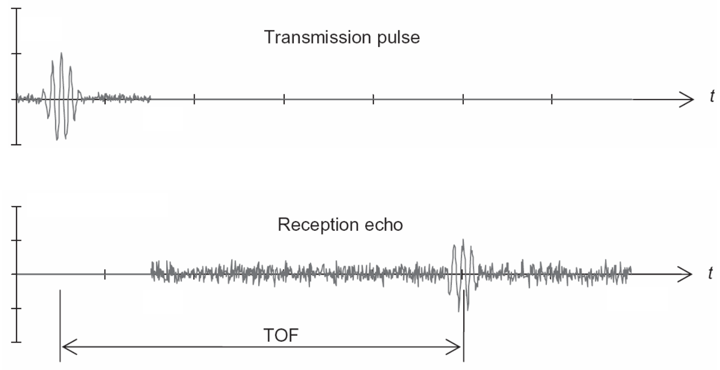

Fig. 4.1: ToF echo detection [71]

In order to more accurately pinpoint the damage position, more information is required. The PZT transducers used can work as sensors or actuators; something which has been incorporated in the algorithms developed. In a network, a minimum of three sensors are needed. If three regions of possible damage location are determined, there will be just one point where all three will intersect.

For phased arrays, the direction of the wavefront propagation is predetermined when the array is activated. Knowing the direction and the time of travel for the echo it is possible to determine the damage location.

Preparing an algorithm to carry out this task depends, on the approach chosen. Network and phased array techniques rely on different algorithms but both can be based on either of two basic principles:

- A simple wave sweep with the installed sensors can be executed. In this case the damage presence will result in unexpected reflections being generated by defects. The echo and permanent reflections created at the boundaries, sensors, other wave types present and discontinuities will be sensed simultaneously;
- The algorithm should be based on the assumption that if the response for the undamaged structure can be compared with the one presenting damage, a difference will emerge at a specific time. This approach allows the isolation of the damage reflection, thus eliminating the permanent reflections.

Even though the second approach is more complex since it demands that the undamaged response is stored at all times, it does make damage detection easier. On the one hand, the possibility of having a superposition of permanent reflections with damage generated ones will have been ruled out from the onset. On the other hand, specimen deterioration (e.g. component aging) can result in different undamaged patterns.

In the following sections, the methods studied for both network and phased arrays are further discussed.

4.1 Sensor Networks

For the sensor network approach, two methods can be implemented. A direct one, which uses only the data collected from the PZT as they generate the wave and sense its reflections. A different method consists of taking into account the reflections captured by the other sensors. Fig. 4.2 shows both methods (first on the right and second on the left), with dots representing the location of PZT.

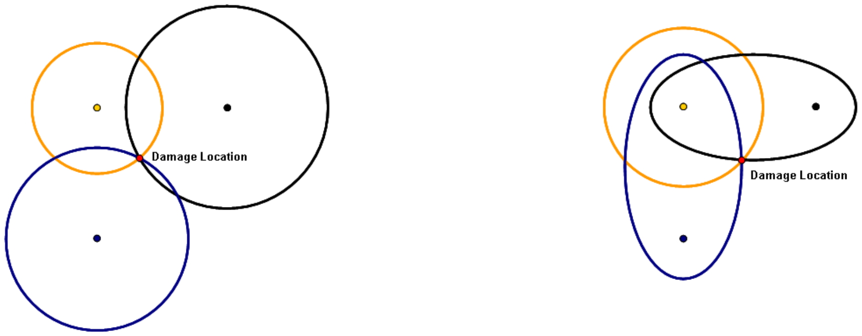

Fig. 4.2: Damage location for a three sensor network

Considering that the propagation velocity is maintained equal along all directions, three circumferences will be determined. These circumferences are based on the fact that echoes and generated waves travel in the same direction but in opposite ways.

In the second case, the equations for one circumference and two ellipses are established. The circumference surrounds the wave generating transducer. The responses gathered by the transducers other than the actuator one include the echoes created by the damage. The time at which these echoes are sensed will depend on the summation of two unknown distances. The first will correspond to the distance travelled by the generated wave until it reaches the damage. The second will be the one travelled by the echo between the damage and the sensor. Since the total distance travelled is known, the locus of the candidate damage points is an ellipse. For the first case presented, knowing the propagation velocity of the wave and the time spent between its emission and echo detection, the travelled distance can be calculated. In this way PZT are seen as both actuators and sensors. The procedure follows:

1. Choose an actuation frequency and determine the wave propagation velocity (*V*);
2. Run separate tests using one actuator at a time;
3. Store the response sensed at that particular transducer;
4. Repeat step 2 on the damaged structure;
5. Repeat step 3. Now, for each PZT, both undamaged and damaged profiles exist;
6. For each data pair , subtract and determine the time at which the echo occurred (t_i , PZT *i*);

7. Knowing the wave velocity and the time, for each PZT, the radial distance to the damage (r_i) can be established. Note that the travelled distance will correspond to twice the radius:

$$2r_i = V\,t_i \tag{4.1}$$

8. For each PZT define a circumference using the PZT position as the centre (x_i, y_i), and the distance found in step 7 as the radius r_i:

$$(x - x_i)^2 + (y - y_i)^2 = r_i^2 \tag{4.2}$$

9. Solve the system of three equations for the unknown coordinates (x, y). They correspond to the damage position.

This approach does not profit from the presence of the other two PZT available at step 2. In order to use them, another assumption must be made: that damage works as a source of reflections, and besides the one that is sent to the actuator (the echo), others are also sent in other directions. From the propagation velocity of the wave and the time spent between its emission and reflection detection, the travelled distance can be estimated. In this way, each PZT is looked at as a sensor. The following procedure requires only one actuation:

1. Choose an actuation frequency and determine the propagation velocity of the wave (*V*);
2. Run one test using just one PZT as an actuator;
3. Store the responses sensed by all PZT;
4. Repeat step 2 on the damaged structure;
5. Repeat step 3. Now, for each PZT, both undamaged and damaged profiles exist;
6. For each data pair, subtract and determine the time at which the damage refection occurred (t_{ij},actuating PZT *i*, sensing PZT *j*);
7. Knowing the wave velocity and the time, for each PZT, the distance travelled by the wave (d_i) can be determined. Note that this corresponds to the total distance

travelled. The first component of which is the distance between the actuator and the damage, while the second one is between the damage and the sensor:

$$d_{ij} = V t_{ij} \tag{4.3}$$

8. For each PZT define an ellipse where the actuating PZT and sensing PZT positions are the two foci. The centre (h, k), semi-major axis a, distance between the two foci c, and semi-minor axis b can be calculated as follows (Note: the *x* axis is parallel to the major axes and one ellipse will in fact degenerate into a circumference, in the case of the PZT serving as an actuator):

$$a_{ij} = \frac{d_{ij}}{2} \tag{4.4}$$

$$c_{ij} = \frac{\sqrt{\left(x_i - x_j\right)^2 + \left(y_i - y_j\right)^2}}{2} \tag{4.5}$$

$$b_{ij} = \sqrt{a_{ij}^2 - c_{ij}^2} \tag{4.6}$$

$$h'_{ij} = x_i + \frac{\left(x_j - x_i\right)}{2} \tag{4.7}$$

$$k'_{ij} = y_i + \frac{\left(y_j - y_i\right)}{2} \tag{4.8}$$

$$\frac{\left(x' - h'_{ij}\right)^2}{a_{ij}^2} + \frac{\left(y' - k'_{ij}\right)^2}{b_{ij}^2} = 1 \tag{4.9}$$

9. Chose one common coordinate system and rotate accordingly the coordinates x', y', h' and k' in order to get x, y, h and k;

10. Solve the system of three equations (two ellipses and one circumference) for the unknown coordinates (x, y). These correspond to the damage position.

Although it is more elaborate, this procedure provides extra data per test run.

The Network algorithms presented are valid for constant thickness specimen made of isotropic materials. For these particular cases, the propagation velocity of the wave can be considered constant. In anisotropic materials or specimen of varying thickness the velocity will not remain constant. From this point onwards, the focus will be on the adaptation of the methods described above to composites. These are known to present a specific wave propagation velocity in each direction, due to different values of the Young modulus for each orientation. This requires an estimate of the wave propagation velocity.

4.1.1 Composite Materials

Considering that wave propagation velocity depends on the orientation:

$$V = V(\theta),\ \theta = 0..\pi \tag{4.10}$$

Note that it is only necessary to predict the velocity distribution along two quadrants, in this case, directions at an angle between 0 and π. This is due to the assumption that composite plates will present anti symmetry with respect to any considered direction. Assuming that there are, at least, four sensors installed in a rectangular arrangement, it is possible to measure the velocity along four different directions. These directions correspond to the lines connecting each sensor pair:

$$V_i = V(\theta_i),\ i = 1..4 \tag{4.11}$$

Using these four known velocities the values for other directions can be estimated through interpolation using a cubic spline (Fig. 4.3).

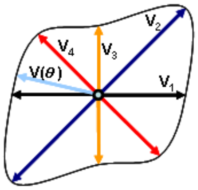

Fig. 4.3: Wave velocity distribution estimate for composite materials

Fig. 4.4 shows a typical wave velocity function.

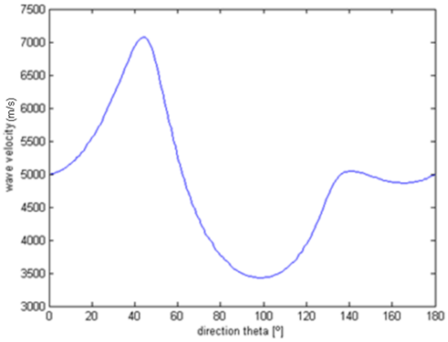

Fig. 4.4: Velocity as a function of theta

For the first method the circumferences will be transformed into velocity dependent shapes. Fig. 4.5 shows an example.

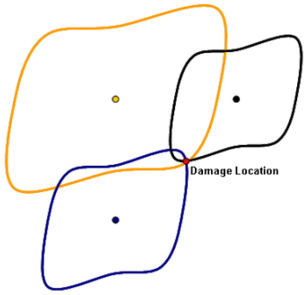

Fig. 4.5: Damage location for composite materials (1st triangulation method)

It is duly noted that the changes imposed by anisotropy will particularly affect the second method presented for damage scanning in networks. The circumference defined by the wave generator transducer will be transformed as previously stated. The velocity of the wave when travelling between the actuator and the damage is, in most cases, different from that of its reflection. Rather than the analytical approach adopted previously for the isotropic case, a numerical solution process is required and is explained below.

Fig. 4.6 shows an illustrative example of an ellipse degeneration (for pure anisotropy). The red circle on the left hand side represents the actuating PZT, while the right one is the sensor.

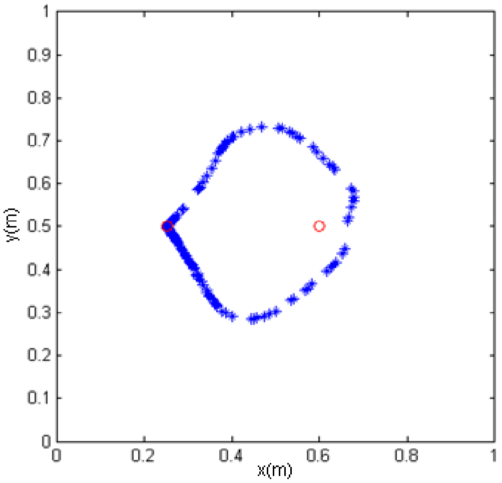

Fig. 4.6: Ellipse degeneration for anisotropic materials

The procedure is then:

1. Run one test using just one PZT as an actuator;
2. Store the responses sensed by all PZT;
3. Repeat step 1 on the damaged structure;
4. Repeat step 2. Now, for each PZT, both undamaged and damaged profiles exist;
5. For each data pair, subtract and determine the time at which the damage refection occurred (t_{ij} ,actuating PZT *i*, sensing PZT *j*);
6. Knowing the velocity distribution and the time at which the echo was detected, for each PZT, the distance travelled by the wave and its damage generated echo $\left(d_W + d_W\right)$ can be determined. Note that d_W will be associated with a particular direction, defined as the Actuator-Damage bearing (θ_W). d_E will have its own direction, defined as Damage-Sensor bearing (θ_E):

$$d_{W\,ij} = V(\theta_W)\ t_{W\,ij} \tag{4.12}$$

$$d_{E\,ij} = V(\theta_E)\ t_{E\,ij} \tag{4.13}$$

$$t_{Tij} = t_{Wij} + t_{E\,ij} \tag{4.14}$$

7. For each actuator PZT *i*, positioned at $\left(x_{Ai}, y_{Ai}\right)$, consider the following numeric procedure:
    a. Estimate the distance travelled by the wave (d_W). For each time step and for every possible direction:

$$d_{Wik} = V(\theta_W)\ t_{Wk}\ ,\ t_k = 1..t_{Ti}\ \theta_W = 0..\pi \tag{4.15}$$

    b. Determine the corresponding possible *x* and *y* coordinates (damage location candidates):

$$x_{ki\theta} = d_{Wik}\ \cos(\theta_W) + x_{Ai} \tag{4.16}$$

$$y_{ki\theta} = d_{Wik}\ \sin(\theta_W) + y_{Ai} \tag{4.17}$$

c. For each of the points above determine the distance and relative orientation with respect to the sensor PZT *j*, positioned at (x_{Sj}, y_{Sj}):

$$d_{Eijk} = \sqrt{(x_{ki\theta} - x_{Sj})^2 + (y_{ki\theta} - y_{Sj})^2} \tag{4.18}$$

$$\theta_{Eijk} = \tan^{-1}\left(\frac{x_{ki\theta} - x_{Sj}}{y_{ki\theta} - y_{Sj}}\right) \tag{4.19}$$

d. Knowing the relative orientation between the candidate points to the sensor PZT *j*, the determination of the corresponding wave propagation velocity becomes possible:

$$V_{Eijk} = V(\theta_{Eijk}) \tag{4.20}$$

e. Using this velocity, determine the time the echo takes to reach the sensor:

$$t_{Eijk} = \frac{d_{Eijk}}{V_{Eijk}} \tag{4.21}$$

f. Plot the candidate points that meet the total time criterion, i.e.:

$$t_{Wk} + t_{Eijk} = t_{Tij} \tag{4.22}$$

4.2 Phased Arrays

When using phased arrays, a number of PZT are being actuated in a predetermined and synchronized way. The lag between each individual actuation, along with the velocity of propagation (V) will determine the wavefront travel direction. These time lags are predetermined by the actuation system programming, which also sets the actuation frequency and, consequently, the wave propagation velocity. Nevertheless, these lags can be calculated using the acquired data. Consider that the reference position of the array is (x_A, y_A). Fig. 4.7 illustrates the procedure for damage location using a linear phased array, where it can be seen that:

- The red line shows the admissible damage locations;
- Blue lines stand for the wave front position at two time steps;
- Orange lines represent the evolution of the wavefront edges (equation (3.13));

- d_{WF} is the distance travelled by the wavefront;
- d_R is the distance travelled by the echo produced by damage;
- d_E is the length of the line that forms a rectangular triangle together with the d_{WF} and d_R lines.

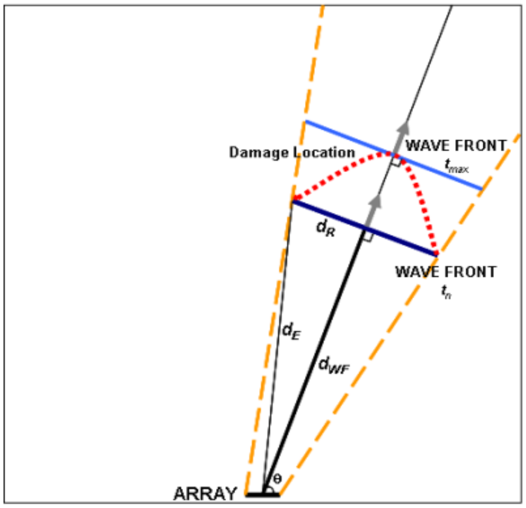

Fig. 4.7: Regions of damage location for a linear phased array

In the isotropic case, the damaged locations lie on a parabola. For composite materials, anisotropy renders this assumption invalid as the velocity of propagation will depend on the orientation. Hence, the locus of the damaged locations may not resemble any particular type of curve. For this reason a numeric procedure was selected.

For a preset orientation, the scanning procedure is as follows:

1. Run one test using the phased array;
2. Store the sensed response gathered by all array PZT;
3. Repeat step 1 on the damaged structure;
4. For each PZT, subtract undamaged from damaged data and determine the time at which the echo occurred (t_i, PZT *i*). This time corresponds to the time it takes for the wavefront to reach the defect plus the time required for the generated reflection to reach the PZT;

5. Knowing the velocity (V_i) and the time (t_i), the total distance (d_i) can be calculated. It corresponds to the distance travelled by the wave front (d_{WF}) plus that one travelled by the echo (d_E) (this is performed for each PZT):

$$d_i = V\,t_i \tag{4.23}$$

$$d_i = d_{WF} + d_E = V\,t_i \tag{4.24}$$

6. Note that the line connecting the damage location to the array may not be parallel to the direction along which the wavefront is propagating. In order to determine the damage position, an iterative calculation is required:

   a. Calculate the distance travelled by the wavefront at each time step:

   $$d_{WF} = V\,t_{WF} \quad t_{WF} = 0 \,..\, t_{\max} \tag{4.25}$$

   b. Determine the distance travelled by the echo:

   t_{MAX} corresponds to the condition where the orientation of the line connecting the damage to the array is parallel to the wavefront propagation direction. In this particular situation:

   $$d_E = d_{WF} \tag{4.26}$$

   For intermediate time steps, the distance travelled by the echo results from the subtraction of the distance travelled by the wavefront to the total distance:

   $$d_E = d_i - d_{WF} \tag{4.27}$$

   c. At each time step, calculate the coordinates (x_{WF}, y_{WF}) which correspond to the point where the wavefront is intersected by a line defining the orientation of the wave front:

   $$x_{WF} = x_A + d_{WF}\ \cos(\theta) \tag{4.28}$$

   $$y_{WF} = y_A + d_{WF}\ \sin(\theta) \tag{4.29}$$

d. Considering that triangle formed by d_{WF}, d_E and d_R, the latter can be computed. This distance is necessary to determine the two possible damage locations at each time step:

$$d_R = \sqrt{d_{WF}^2 + d_E^2} \tag{4.30}$$

e. Given these two candidates for damage location , which lie on either side of (x_{WF}, y_{WF}), the corresponding *x* and *y* coordinates can be calculated:

$$x_{LEFT} = x_{WF} - d_R \ \cos(\theta - \frac{\pi}{2}) \tag{4.31}$$

$$y_{LEFT} = y_{WF} - d_R \ \sin(\theta - \frac{\pi}{2}) \tag{4.32}$$

$$x_{RIGHT} = x_{WF} + d_R \ \cos(\theta - \frac{\pi}{2}) \tag{4.33}$$

$$y_{RIGHT} = y_{WF} + d_R \ \sin(\theta - \frac{\pi}{2}) \tag{4.34}$$

This proposed algorithm allows the detection of the probable damage location, for a given wave front orientation and echo ToF. There will be as many of these regions as transducers in the array. This contrasts with previous approaches, mentioned in the literature, where there is only one such region [71].

In composite materials, where the wave velocity depends on the chosen orientation for the beam, the algorithm should account for this fact. So, in steps 5 and 6 above, the propagation velocity becomes a function of the direction, $V(\theta)$.

From the application of the algorithms presented to real experiments, it was found that the equation solving and the numerical procedures involved are computationally demanding.

The approaches defined here do not account for experimental issues. It is assumed that the time at which the damage reflection occurred is known from the onset. Signal processing and treatment is therefore one of the main topics in the next chapter.

CHAPTER 5

PIEZO NETWORKS

With the Lamb wave preliminary study and algorithms determination already carried out, experimental damage detection could be tested. Several setups were put to test by varying the number of sensors, test specimen material and test procedures. During this work, post processing algorithms and related software were continuously updated. For the initial phase a three sensor network was implemented on a thin aluminum plate. As aforementioned, the S-Wave is used in all of the trials.

5.1 Three Sensor Network Applied to an Isotropic Plate

During this phase, experiments using the second network algorithm (section 4.1) were performed.

From the frequency scan results in section 3.5, at 333 KHz, the S-Wave reaches its maximum amplitude when the A-Wave is at one of its lowest amplitude values. Because of this, tests were also run at 240 KHz, where the S-Wave time definition was much better.

After selecting the trial frequencies, for each one of them, experiments were done using a single PZT as an actuator and then all of them as sensors. Since three PZT were available, one test run included three experiments and nine output files, three for each PZT. They were numbered and a Cartesian coordinate system was implemented, all according to Fig. 5.1. An N-S-E-W system where N is aligned with the y-axis was also considered, to refer to specific boundary reflections. A trial damage location was set at (0.448, 0.055) m. This particular location was chosen to avoid the overlap of the echo with other permanent reflections.

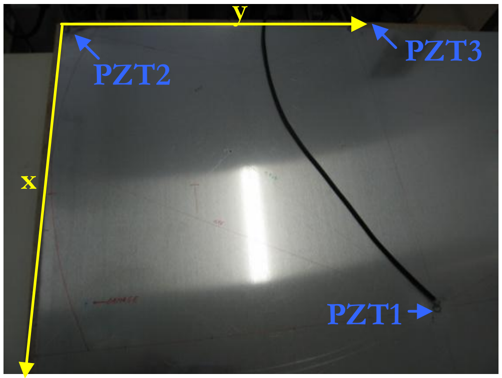

Fig. 5.1: Aluminum plate and coordinate system implemented

During the first test phase, the primary objectives were to identify both the S-Wave and the A-Wave, boundary reflections and the S-Wave propagation velocity. In Fig. 5.2, for the 240 KHz and 333 KHz frequencies, the actuation wave departing from sensor 1 and read on sensor 3, is shown. The S-Wave, the North, South and West reflections, the Sensor 2 reflection and the A-Wave can be easily identified.

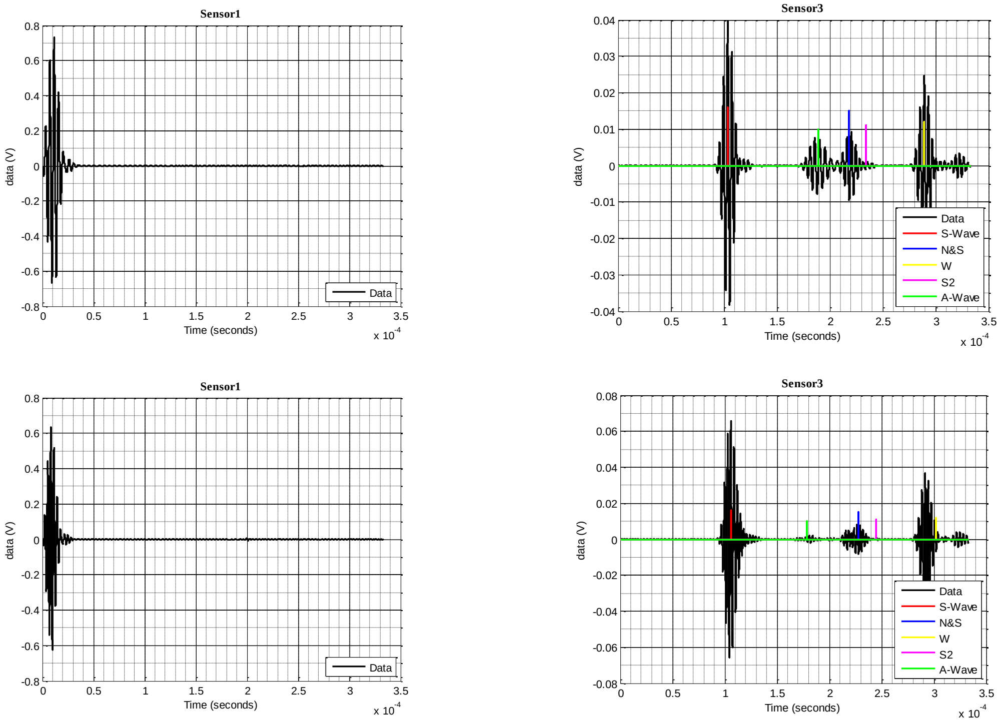

Fig. 5.2: Actuation wave and respective reflections (top 240 KHz - bottom 333 KHz)

As mentioned before, at the frequency of 333 KHz the A-Wave disappears and the S-Wave is not as well defined in time.

The velocity found for the S-Wave at 240 KHz was 5381 m/s and for 333 KHz it was 5175 m/s. These results are consistent with the theory (Fig. 3.11).

The wavelength plays an important role in the precision of the algorithms. For the S-Wave, at 240 KHz the half wavelength is 11.21 mm and for 333 KHz it is 8.1 mm (Fig. 3.12). These values are important for the determination of the tolerance that is set when trying to pinpoint the damage.

Next, data was collected for the undamaged plate and then for a damaged plate where defects were sequentially and cumulatively added : a 1 mm crescent shaped hole, a 1 mm diameter hole, a 2 mm diameter hole, a 7 mm crack, and a through-thickness 12 mm crack.

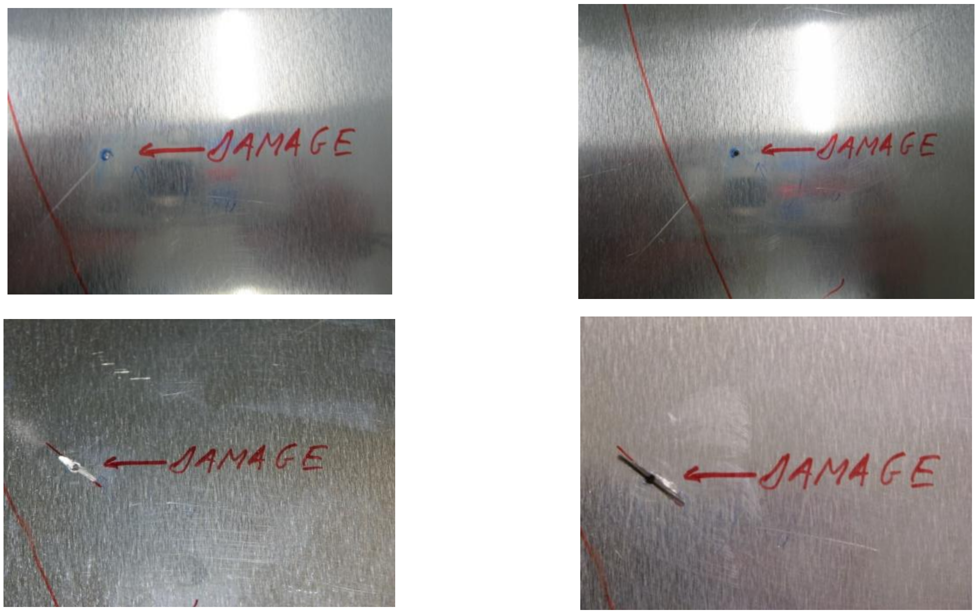

Fig. 5.3: Plate's inflicted damage types

The NI SIGNAL EXPRESS® was used during this phase. It allowed successive actuation waves to be sent to a PZT as well as to collect the responses sensed by all PZT. In addition, a 2nd order band-pass filter could be applied to remove all the out of frequency responses. Results can then be saved as ASCII text files.

After collecting all the responses for every case, a MATLAB® code was used to process them in a systematic manner. This code was designed to fulfill the following:

1. Read the output files and convert them to MATLAB® files;

2. Calculate the S-Wave speed, based on the time lapsed between the actuation and the wave arrival and the known distance between the actuator/sensor pair;
3. Compare the damage and undamaged data and find at which point in time the damage reflection occurs;
4. Determine the three ellipse equations and solve the system to find the damage position;
5. Display an image the plate and pinpoint the damage.

After running several experiments and analyzing the results, it was concluded that the reflection from the damage could not be easily identified. In theory, one extra wave should appear when subtracting the damaged response from the undamaged one. However, in reality, this procedure is not directly applicable since other factors affecting the data (e.g. noise). The challenge is then to define a data post-processing technique in way that the time at which the reflection wave appears can be clearly identified.

By comparison of the results from independent but identical trials it was found that:

- The hardware does not guarantee synchronism in the time domain. This problem leads to data shifting in the time axis;
- The sensed amplitude may not be exactly the same at the same step size, even if the data being compared is synchronized. Although these discrepancies may be small, they really affect the consistency of the data, which can lead to ghost damage being detected.

The solutions adopted for each of these cases were as follows:

1. Perform a phase study. The program analyzes the peaks and valleys and then stores that information for both the damaged and undamaged plate. If they present the same behaviour during a certain amount of time, which depends on the actuation frequency, subtraction is only considered if it reaches values that are higher than a certain reference.
2. Establish a noise threshold. A minimum amplitude difference is established, below which any data it discarded.

In this case study, the time at which the damage must appear is known, since the position is predetermined. Comparing data before and after the damage is created, it was found that differences appeared after the damage generated wave and before its "re-reflections" or A-Wave reflections. This occurs because the damage reflection itself will interfere with the permanent reflections. So, if one determines the beginning of the interference it is possible to determine the time at which the damage reflection occurred.

Despite all these corrections, ghost damage was still present. It became clear that false positives are also detected, which jeopardizes the location of the actual damage. Still, it was assumed that the damage reflection should be present in the majority of the data with reference to the damaged plate.

Data correction rules that reveal themselves to be too narrow can lead to undesirable data elimination. In order to avoid eliminating an actual damage reflection, the program is allowed to determine a number of possible damages per sensor - four in this case. In this way, it is accepted that detected damages may or not be true damages. The superposition of data sets will determine which ones are more likely to represent the actual damage. Therefore, the idea is to detect damage not in a deterministic way but by means of the consistency in responses obtained.

A last problem was identified, regarding the PZT that was connected to both signal generation and acquisition hardware. In this particular situation, after the PZT delivered the actuation signal (at which point it becomes a sensor), the connection to the generation channel absorbed part of the sensed signal energy. Due to this, it was sometimes impossible to retrieve any useful data. At this stage, the solution was to artificially include the expected ToF in the data acquired by these transducers.

After updating the MATLAB® code to account for all these particular issues, the damage detection tests were executed. The possible damage locations are found by solving the system of three equations in the algorithm explained in section 4.1. Because of some uncertainty, a tolerance of 7 mm was taken into consideration (for the intersections), which is smaller than the 333 KHz actuation wavelength.

In Fig. 5.4 to Fig. 5.13, results are presented for possible damage locations and respective intersections for each PZT actuation case (240 KHz and 333 KHz and all damages considered). In each set of results: Top-Left actuator PZT1; Top-Right actuator PZT2; Bottom-Left actuator PZT3; Bottom-Right possible damage locations (resulting from ellipse intersections). Furthermore, the partial circumferences in red denote results from PZT1, green from PZT2 and blue from PZT3. The partial ellipses colors refer to the passive PZT. The letter D marks the location of the actual damage.

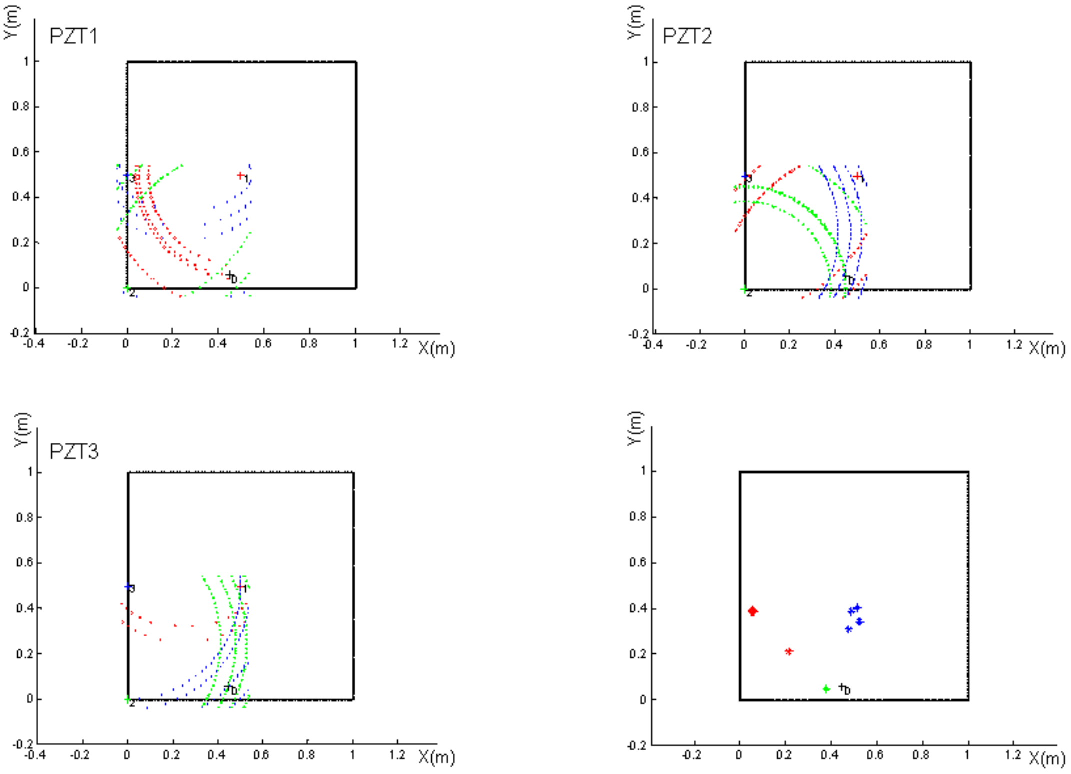

Fig. 5.4: 1st experiment (frequency 240 KHz - damage 1 mm diameter half hole)

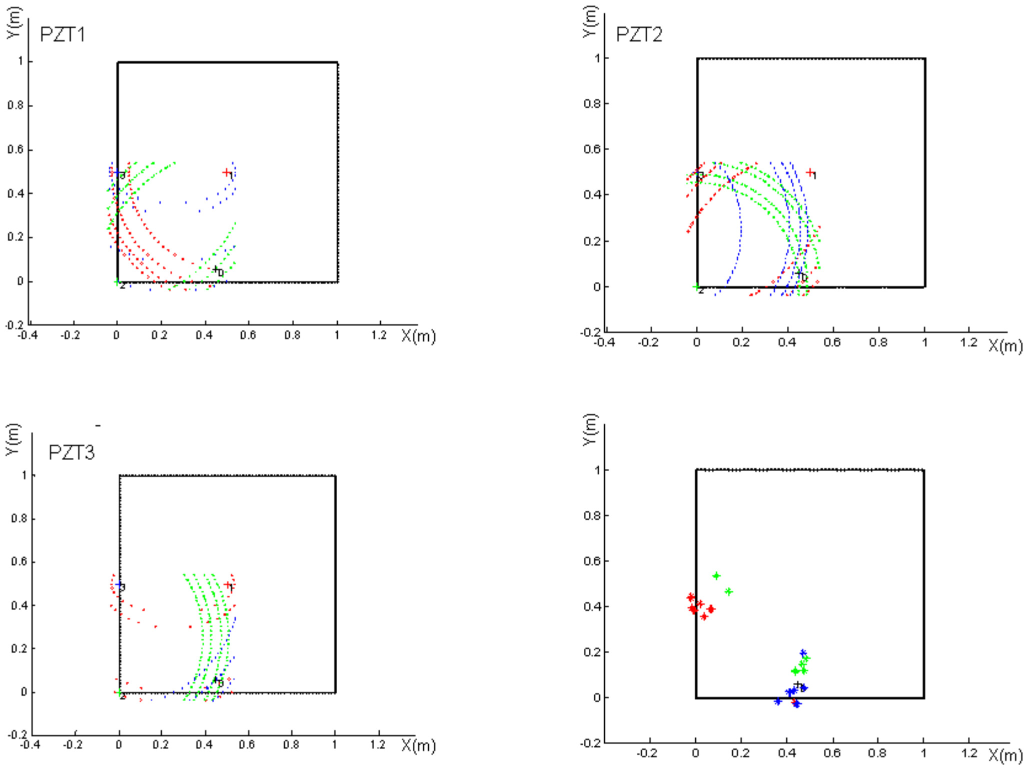

Fig. 5.5: 2nd experiment (frequency 333 KHz - damage 1 mm diameter half hole)

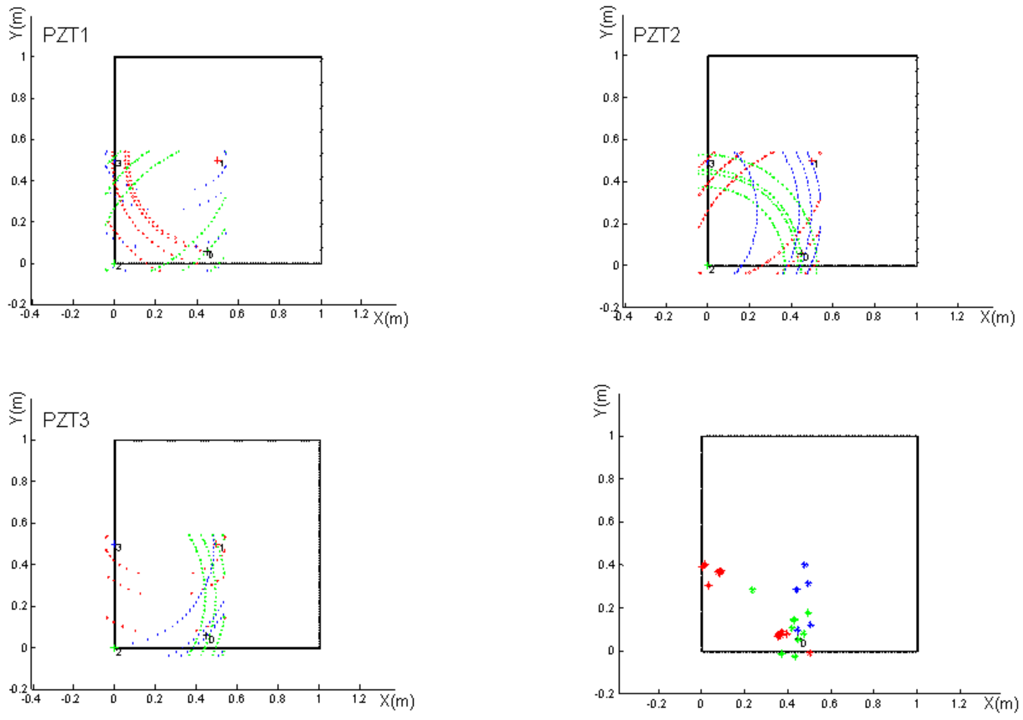

Fig. 5.6: 3rd experiment (frequency 240 KHz - damage 1 mm diameter hole)

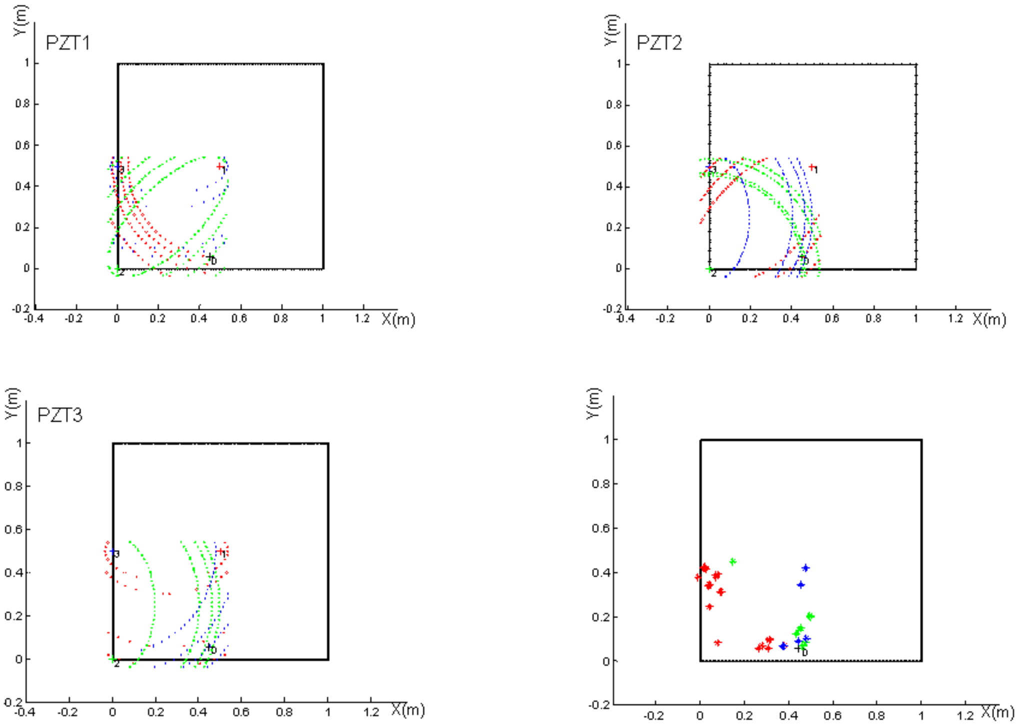

Fig. 5.7: 4th experiment (frequency 333 KHz - damage 1 mm diameter hole)

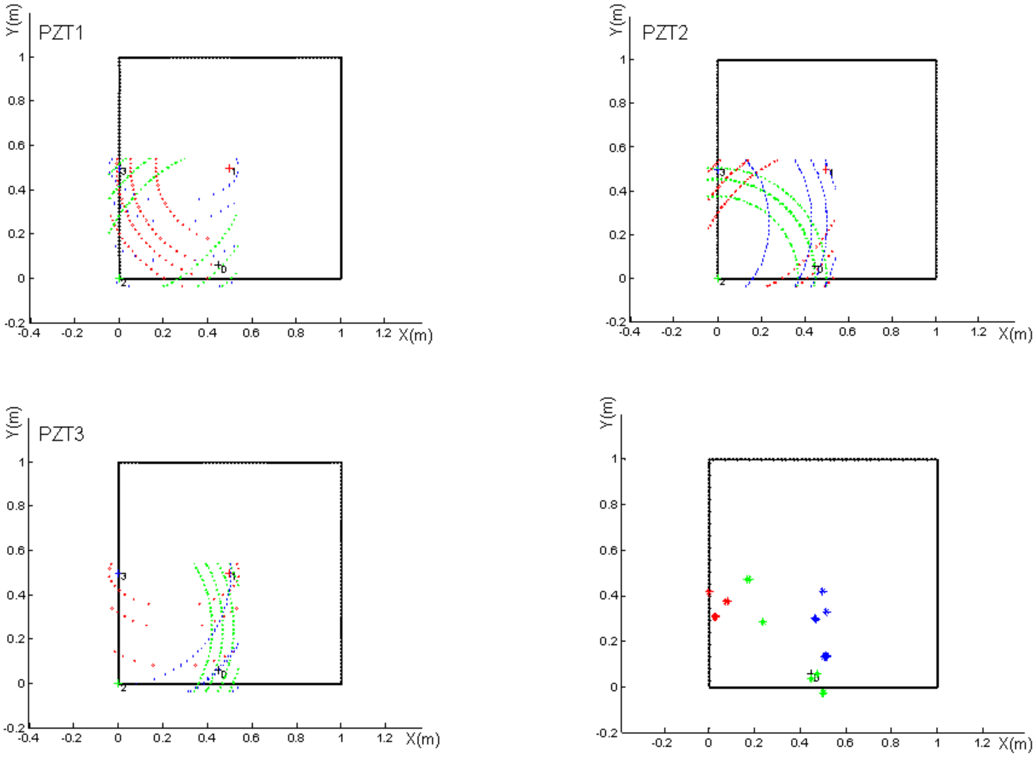

Fig. 5.8: 5th experiment (frequency 240 KHz - damage 2 mm diameter hole)

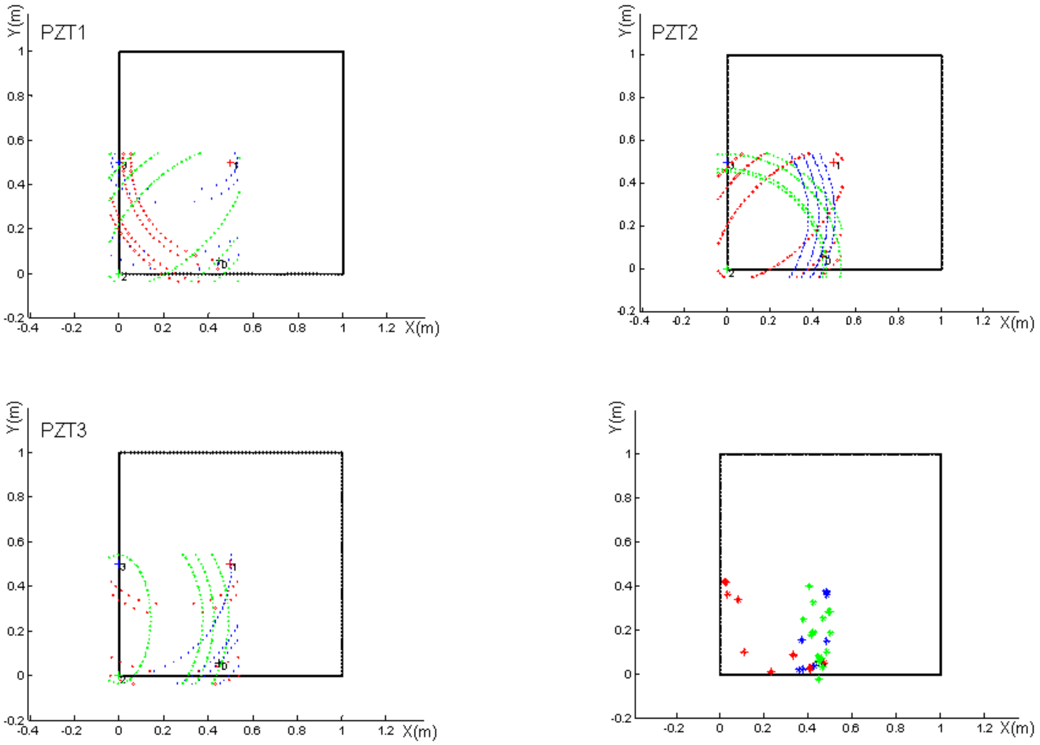

Fig. 5.9: 6th experiment (frequency 333 KHz - damage 2 mm diameter hole)

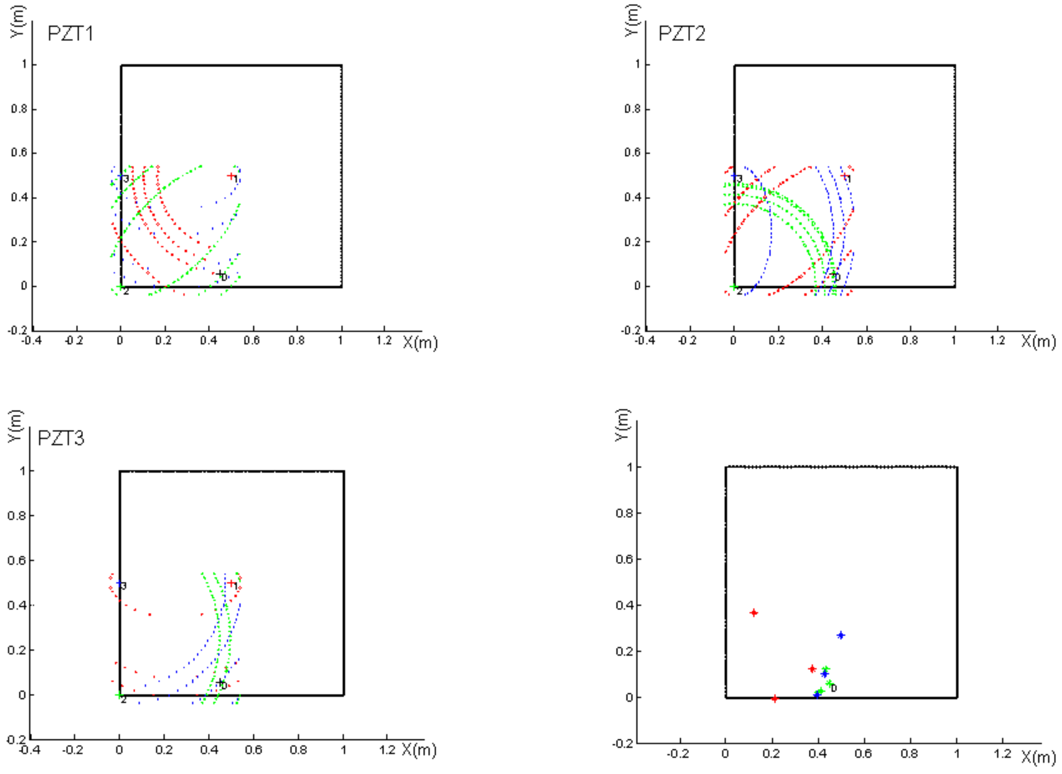

Fig. 5.10: 7th experiment (frequency 240 KHz - damage 7 mm crack)

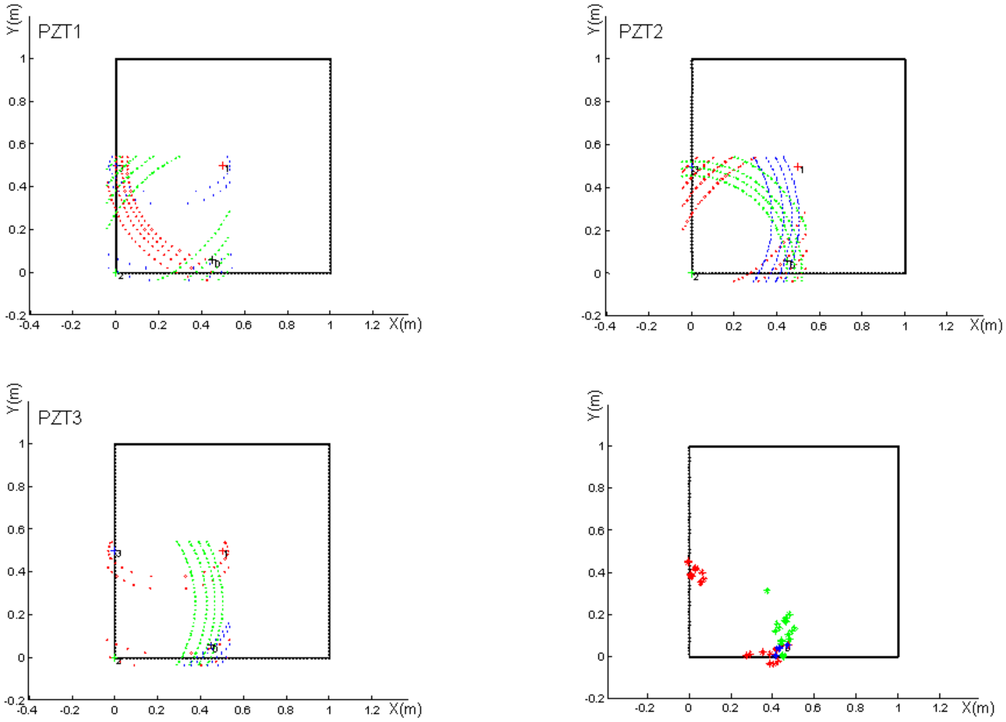

Fig. 5.11: 8th experiment (frequency 333 KHz - damage 7 mm crack)

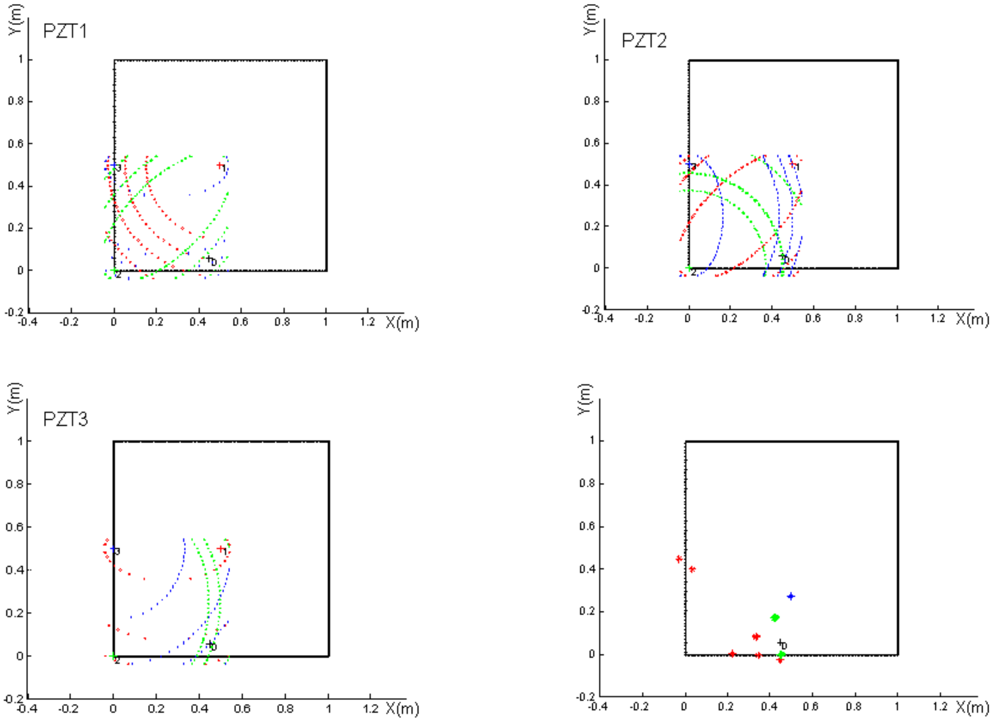

Fig. 5.12: 9th experiment (frequency 240 KHz - damage 12 mm crack)

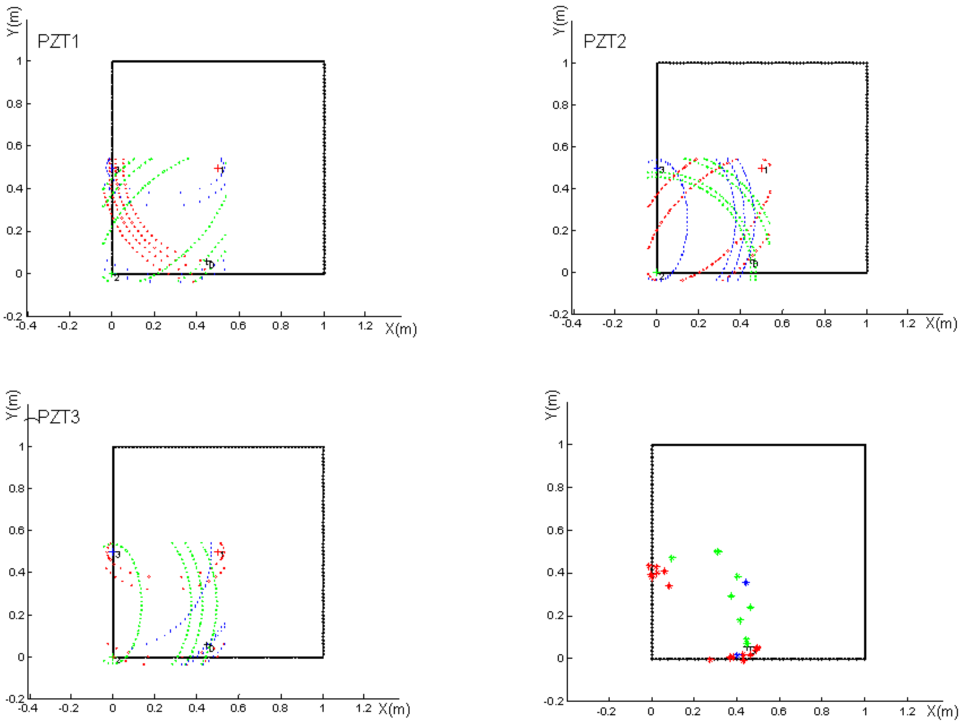

Fig. 5.13: 10th experiment (frequency 333 KHz - damage 12 mm crack)

Considering that damage will most likely be present in an area that shows the largest density of intersections (of every color, as seen on Bottom-Right in each set), the following remarks can be made:

- In spite of the tests at 240 KHz showing a better time definition, the damage detection results were not satisfactory. Still, on the 3rd experiment the damage presence was detected with reasonable accuracy;
- When applying the 333 KHz frequency improved results were obtained for all types of damage.

For each test case, a circular search region (with a radius equal to one half wavelength) is used to seek for areas where intersections found with the three actuating different PZT are present. If these conditions are met the centre of the search region will point to the probable damage location (shown in Fig. 5.14 and Fig. 5.15 as a red diamond).

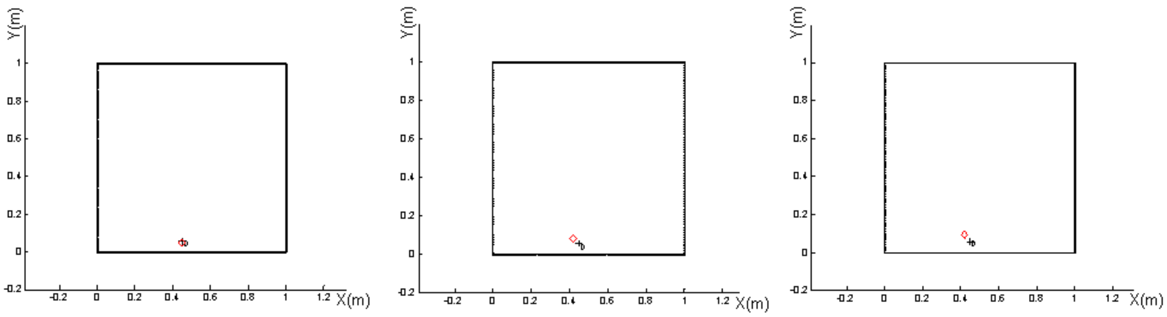

Fig. 5.14: Calculated damage positions for the 2nd, 3rd and 4th experiments

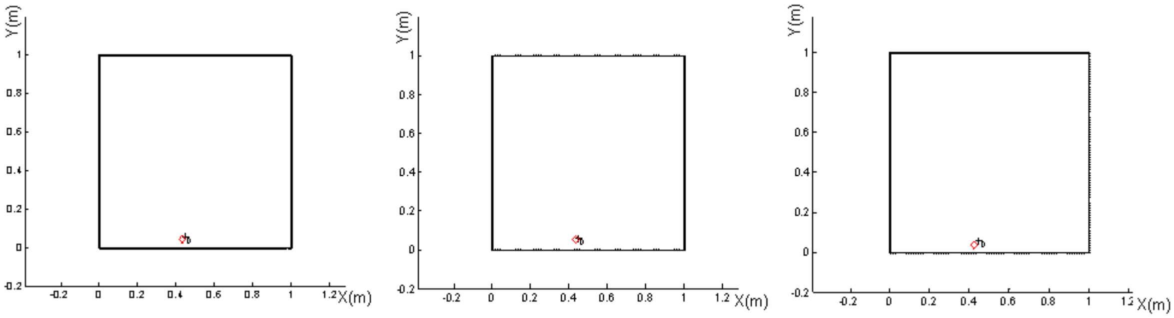

Fig. 5.15: Calculated damage positions for the 6th, 8th and 10th experiments

5.1.1 Conclusions

During these experiments path some important conclusions were drawn:

- With the assumption that unexpected reflections are detected, the capture of the real damage location was made possible;
- Although the actuating PZT data was artificially corrected, the remaining data allowed successful damage location;
- Although the algorithm is, up to a certain extent, very simple, it produced very good results.

Regarding the first set of results, the fact that it was possible to detect damages of 1 mm in size using the optimum 333 KHz frequency which confirmed that this was a worthwhile approach.

Even though the analysis process was not fully automated, several codes were developed which in quick and systematic way allowed the detection of the position of possible damages.

5.2 Four Sensor Network Applied to an Isotropic Plate

Experiments and their respective post-processing were time consuming. In order to help in reducing the time spent on data acquisition, processing and output of results, various MATLAB® codes were gathered and adapted for use with LABVIEW®. This software was chosen because it natively controls both acquisition and generation boards. Additionally, being a visual programming tool, it helped in defining all necessary processes intuitively. Initially developed to work with only three transducers, it was modified to support up to four sensors. The difficulties in reading the response gathered by the transducer which was responsible for the wave generation, justified this modification.

A slight change had to be made to the damage detection algorithm. Per test run, i.e., when a certain transducer worked as actuator, only the remaining three sensors responses were analyzed. No longer were one circle and two ellipses defined. Instead, three ellipses were established. The algorithm then used only these for pinpointing the damage.

Undamaged and damaged data post-processing, prior to the damage detection algorithm step, was improved. Additionally, equation solving (which is computationally demanding) for damage location was discontinued, giving place to a visual tool. Drawing the various ellipses on a representative plate is enough to pinpoint the damage location (by means of the superposition of these curves).

5.2.1 LABVIEW® Program

As mentioned before, a LABVIEW® program was developed to carry out all the necessary steps: configuration options, generation of theoretical dispersion graphs, data acquisition and damage detection.

The program front panel was defined on a Tab like control. Fig. 5.16 shows configuration tab.

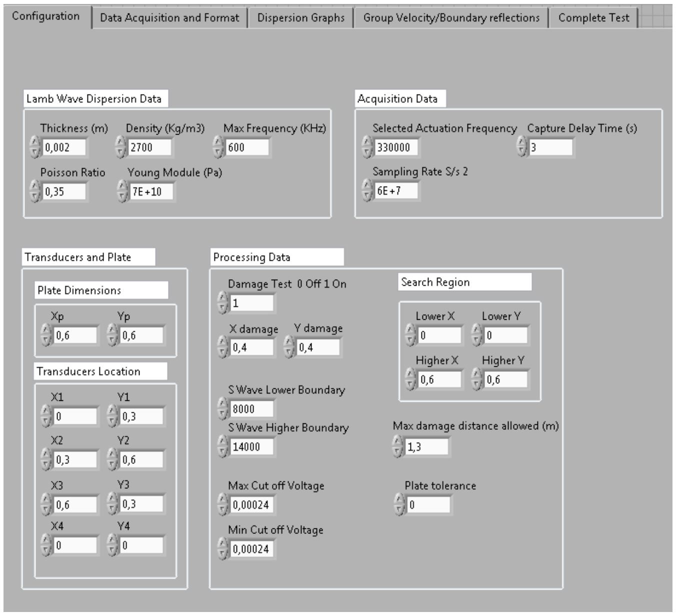

Lamb Wave Dispersion Data
Thickness (m) 0,002
Density (Kg/m3) 2700
Max Frequency (KHz) 600
Poisson Ratio 0,35
Young Module (Pa) 7E+10

Acquisition Data
Selected Actuation Frequency 330000
Capture Delay Time (s) 3
Sampling Rate S/s 2 6E+7

Transducers and Plate
Plate Dimensions
Xp 0,6
Yp 0,6
Transducers Location
X1 0
Y1 0,3
X2 0,3
Y2 0,6
X3 0,6
Y3 0,3
X4 0
Y4 0

Processing Data
Damage Test 0 Off 1 On 1
X damage 0,4
Y damage 0,4
S Wave Lower Boundary 8000
S Wave Higher Boundary 14000
Max Cut off Voltage 0,00024
Min Cut off Voltage 0,00024
Search Region
Lower X 0
Lower Y 0
Higher X 0,6
Higher Y 0,6
Max damage distance allowed (m) 1,3
Plate tolerance 0

Fig. 5.16: Configuration tab

On the configuration tab, the user can define all instances that refer to general configuration. The available options affect dispersion data, acquisition process, experimental setup and damage location process.

Lamb wave dispersion information is crucial for every test run. Based on this fact a tab was created which allows the user to input the mechanical properties and thickness of any plate being submitted to experimentation. This module numerically solves the Lamb wave equations for the first modes. It outputs the wave velocity, group velocity and wavelength graphs (as seen in section 3.3). Furthermore, the user can input a sensor diameter and check which for the most adequate actuation frequencies. Fig. 5.17 shows the Dispersion Graphs Tab.

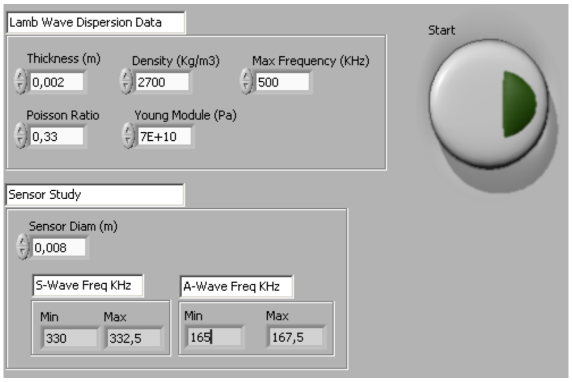

Lamb Wave Dispersion Data
Thickness (m) 0,002
Density (Kg/m3) 2700
Max Frequency (KHz) 500
Poisson Ratio 0,33
Young Module (Pa) 7E+10

Sensor Study
Sensor Diam (m) 0,008
S-Wave Freq KHz
Min 330
Max 332,5
A-Wave Freq KHz
Min 165
Max 167,5

Fig. 5.17: Dispersion graphs tab

Forwardly, Fig. 5.18 shows the acquisition tab.

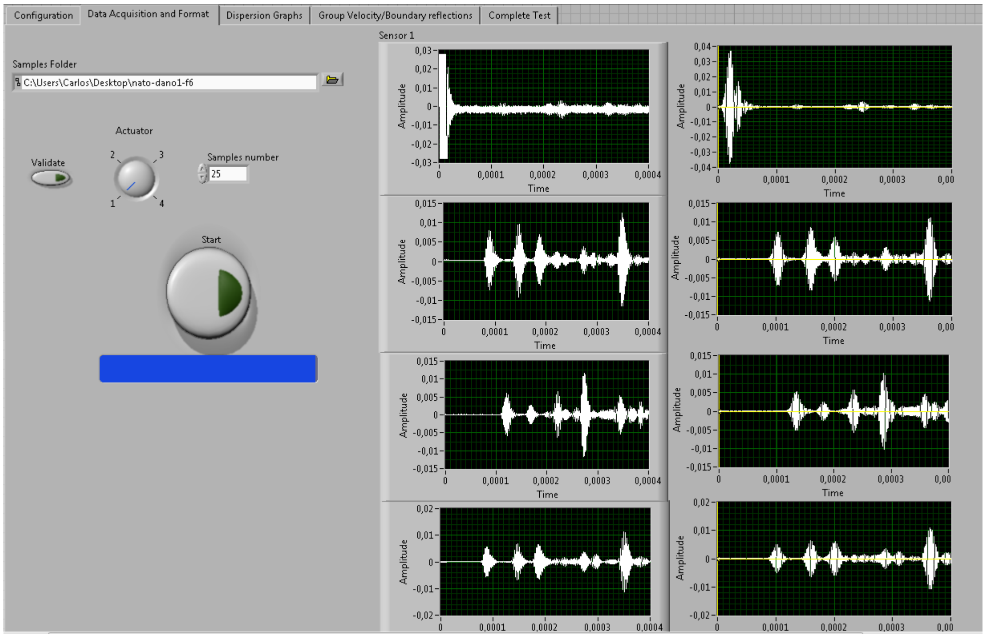
Samples Folder: C:\Users\Carlos\Desktop\nato-dano1-f6

Samples number: 25

Fig. 5.18: Acquisition tab

This frame allows the user to select the desired data destination folder, the transducer being used as an actuator and the number of samples to be captured. The user can also validate the real and filtered responses gathered by all transducers.

In order to make sure that the readings are more consistent, a number of samples are retrieved and averaged. During the averaging process the following values are calculated for each time step:

- Average;
- Maximum;
- Minimum;
- Standard deviation.

A file that includes all of the above is stored for future processing.

At the Group Velocity/Boundary reflections tab, Fig. 5.19, the user can validate each test run data with boundary reflections, group velocities and time responses checks.

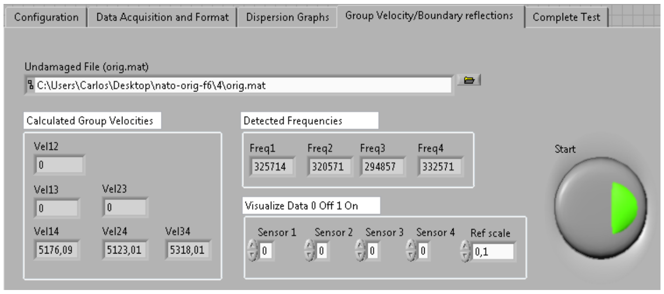

Undamaged File (orig.mat): C:\Users\Carlos\Desktop\nato-orig-f6\4\orig.mat

Calculated Group Velocities

Vel12: 0
Vel13: 0
Vel23: 0
Vel14: 5176,09
Vel24: 5123,01
Vel34: 5318,01

Detected Frequencies

Freq1: 325714
Freq2: 320571
Freq3: 294857
Freq4: 332571

Visualize Data 0 Off 1 On

Sensor 1: 0
Sensor 2: 0
Sensor 3: 0
Sensor 4: 0
Ref scale: 0,1

Fig. 5.19: Group velocity/Boundary reflections tab

Finally the tab that allows the user to run the detection algorithms is shown in Fig. 5.20.

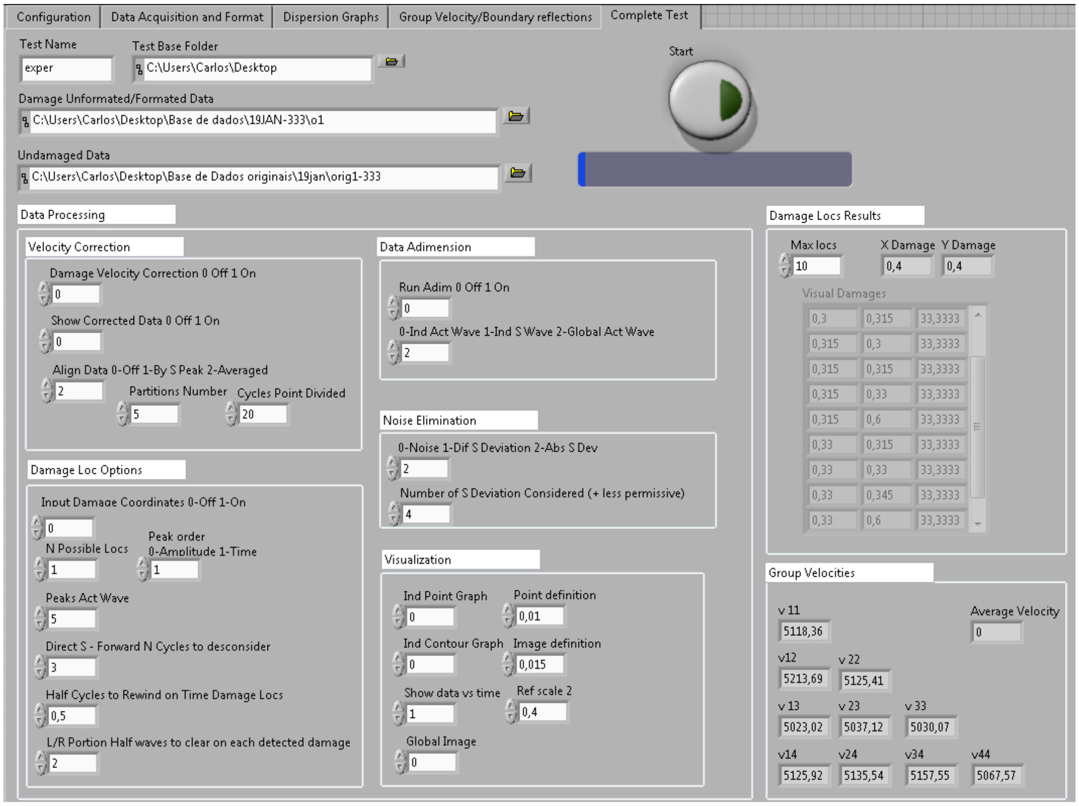

Test Name: exper
Test Base Folder: C:\Users\Carlos\Desktop
Damage Unformated/Formated Data: C:\Users\Carlos\Desktop\Base de dados\19JAN-333\o1
Undamaged Data: C:\Users\Carlos\Desktop\Base de Dados originais\19jan\orig1-333

Data Processing

Velocity Correction

Damage Velocity Correction 0 Off 1 On: 0
Show Corrected Data 0 Off 1 On: 0
Align Data 0-Off 1-By S Peak 2-Averaged: 2
Partitions Number: 5
Cycles Point Divided: 20

Damage Loc Options

Input Damage Coordinates 0-Off 1-On: 0
N Possible Locs: 1
Peak order 0-Amplitude 1-Time: 1
Peaks Act Wave: 5
Direct S - Forward N Cycles to desconsider: 3
Half Cycles to Rewind on Time Damage Locs: 0,5
L/R Portion Half waves to clear on each detected damage: 2

Data Adimension

Run Adim 0 Off 1 On: 0
0-Ind Act Wave 1-Ind S Wave 2-Global Act Wave: 2

Noise Elimination

0-Noise 1-Dif S Deviation 2-Abs S Dev: 2
Number of S Deviation Considered (+ less permissive): 4

Visualization

Ind Point Graph: 0
Point definition: 0,01
Ind Contour Graph: 0
Image definition: 0,015
Show data vs time: 1
Ref scale 2: 0,4
Global Image: 0

Damage Locs Results

Max locs: 10
X Damage: 0,4
Y Damage: 0,4

Visual Damages

0,3	0,315	33,3333
0,315	0,3	33,3333
0,315	0,315	33,3333
0,315	0,33	33,3333
0,315	0,6	33,3333
0,33	0,315	33,3333
0,33	0,33	33,3333
0,33	0,345	33,3333
0,33	0,6	33,3333

Group Velocities

v 11: 5118,36
Average Velocity: 0
v12: 5213,69
v 22: 5125,41
v 13: 5023,02
v 23: 5037,12
v 33: 5030,07
v14: 5125,92
v24: 5135,54
v34: 5157,55
v44: 5067,57

Fig. 5.20: Damage location tab

For the algorithm execution the user has some options available that have to be correctly adjusted in order to ensure the maximum degree of truth in the detection. At runtime, the software outputs a figure displaying the most probable damage locations. Additionally, it displays these possible damage locations along with their respective computed value of the degree of truth. This parameter is estimated based on the attained number of superimposed regions, and the number of damage locations allowed to be detected times the number of piezo sensors in the network.

5.2.2 Processing Updates

During the experiments in sections 5.1 and 5.2, problems relating to the lack of consistency in the data were detected. As an example, data retrieved from an undamaged plate at two different times would produce different signatures. After various observations, it was concluded that the main origin of these unexpected inconsistencies was the actuation equipment. A slight change in the initial actuation wave time or its amplitude is enough to produce small changes that deteriorate the validity of the data comparison. In order to mitigate this problem, the following updates were implemented:

- Data alignment processing. In order to correct time data shifts and slight velocities variations, data can be aligned using as a reference:
    - The velocity found for the undamaged data. For this case, the damaged plate data is processed in order to present the same exact velocity;
    - The actuation peak time;
    - The direct S-Wave peak time;
    - An average that considers a number of peak locations that must coincide in damaged and undamaged plate data.
- Data amplitude normalization, assuming, as a reference:
    - The direct S-Wave undamaged amplitude for each transducer;
    - The actuation wave amplitude:
        - From the undamaged actuating PZT;
        - From each actuating PZT, different for the damaged and undamaged case.
- Data noise reduction. During this procedure, a validation rule is applied to filter signal differences:
    - At each time step, determine the amplitude difference and compare it with the highest standard deviation (σ) determined for undamaged (*UD(t)*) and damaged plate data (*D(t)*). Discard only the differences that respect the following rule (*n* being the number of standard deviations allowed):

$$|UD(t)-D(t)|<n\sigma_{\max} \tag{5.1}$$

- At each time step, determine if the averaged damaged value follows the rule below. In case it does, discard it:

$$-n\sigma_{UD(t)}+\min(UD(t))<D(t)<n\sigma_{UD(t)}+\max(UD(t)) \tag{5.2}$$

$$-n\sigma_{D(t)}+\min(D(t))<UD(t)<n\sigma_{D(t)}+\max(D(t)) \tag{5.3}$$

Even though all updates provided satisfactory results, the last options for each update were the ones that provided the highest degree of truth in the detection.

5.2.3 Damage Location Experiment

A new setup, consisting of a 0.6m x 0.6m aluminum plate was prepared to test both the LABVIEW® based application and its updated processes. Four PZT were glued and a 1 mm through-thickness hole was drilled to simulate the damage. As there are four sensors, four sets of results can be obtained, each one corresponding to one actuating PZT. Fig. 5.21 shows the data acquired for the undamaged and damaged plate, using transducer #3 as an actuator. The green lines represent the possible damage ToF and the expected ToF of the actual damage is shown in magenta.

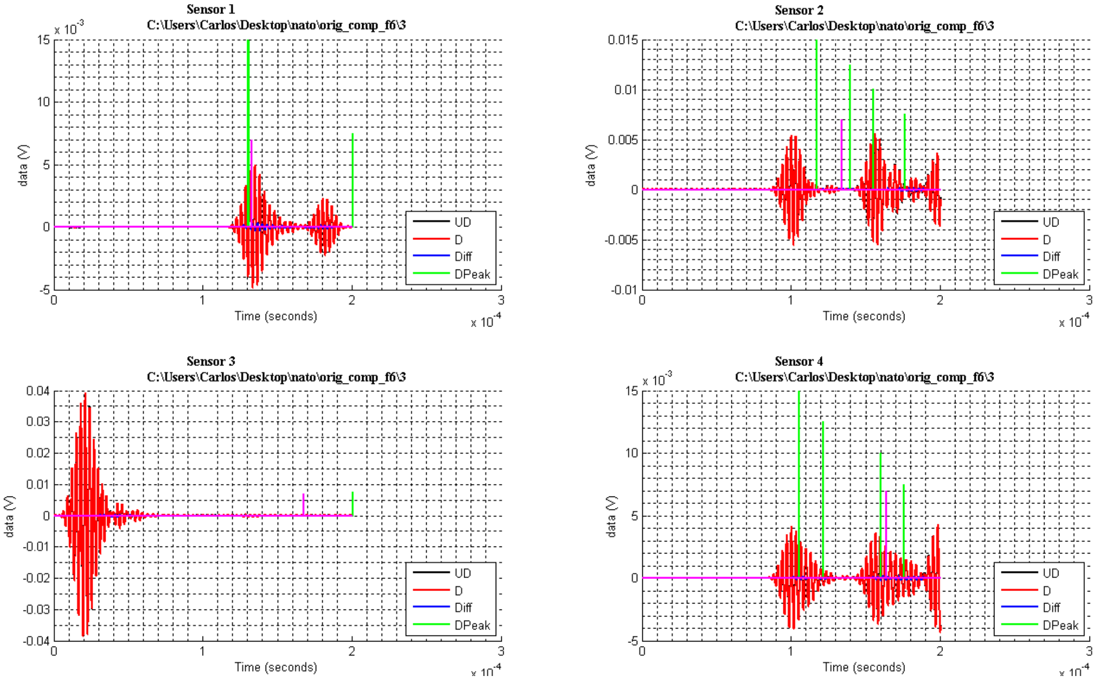

Fig. 5.21: Sensors acquired time data (actuating PZT #3)

Using the respective ToF's, the possible locations of the damage can be estimated and represented by ellipses. Fig. 5.22 exemplifies this.

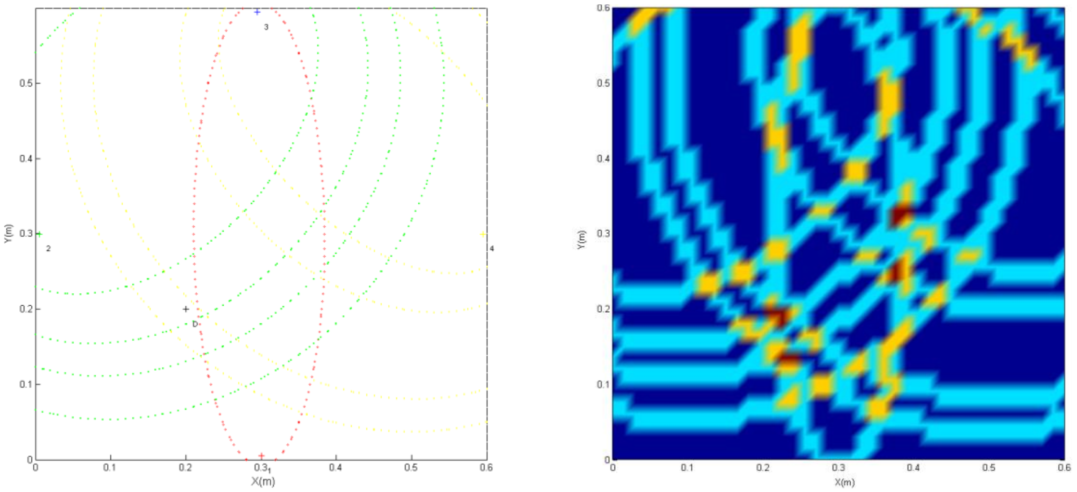

Fig. 5.22: Ellipses point (left) and contour (right) plots

In the point plot, the positions of transducers can be seen along with the actual location of the damage. Notice that all pairs including the actuator are the foci of the ellipses shown. In the contour plot, the superposition of ellipses allows for a better visual representation of the possible damage locations. Red zones represent the ones where superposition is more intense.

It can be seen that, despite the true damage location being correctly pointed, other ghost damage locations are also presented. Only by merging the results from all four sensors as actuators, can ghost damages be made to disappear.

On the left of Fig. 5.23 one can read the possible damage locations (in terms of x and y coordinates), followed by their calculated degree of truth (DT). On In Fig. 5.23 represents the summation of all contour plots, and the damage position is marked in red.

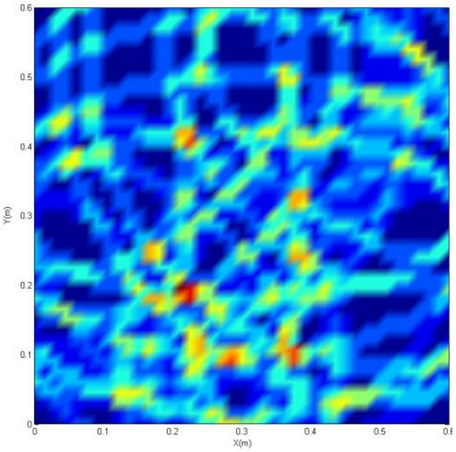

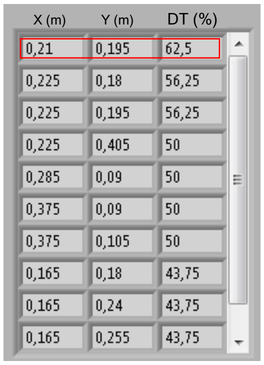

X (m)	Y (m)	DT (%)
0,21	0,195	62,5
0,225	0,18	56,25
0,225	0,195	56,25
0,225	0,405	50
0,285	0,09	50
0,375	0,09	50
0,375	0,105	50
0,165	0,18	43,75
0,165	0,24	43,75
0,165	0,255	43,75

Fig. 5.23: Global contour plot (left) - *x* and *y* probable damage locations (right)

One of problems mentioned in section 5.1 was the impossibility of acquiring useful data on the actuating transducer. Furthermore, during the experiments, the cables connecting the actuation board and the transducers had to be constantly changed, depending on the actuating PZT. This jeopardized the system's operational capability and reliability.

5.3 PCB Development and Testing

In order to make the actuating PZT useful for data acquisition, its connection to the signal generator board had to be cut immediately after the wave generation. By doing this, the signal produced by the transducer could be routed to the acquisition board directly. Also, the automation of the test process was desirable. Essentially, the idea was to create a "push-button" procedure to perform all the necessary data acquisition. A printed circuit board (PCB) was fitted to this solution.

The solution had to fulfill the following requisites:

- Select the actuating transducer;
- Open the acquisition channels for the sensing transducers;
- Open the generation channel for the actuating transducer;
- Send the actuation wave, created by the generation board, to the actuating transducer. This process is started automatically. The PCB triggers the generation board;

- Immediately after the actuation wave discharge, interrupt the generation channel and allow the connection between the actuating transducer to the respective acquisition channel;
- Finally, repeat all the above sequenced steps for the remaining transducers.

In order to comply with these requisites, an electronic circuit was designed, controlled by a microprocessor - a Texas Instruments MCP EZ430. This processor was selected because:

- It possessed a satisfactory processing clock speed;
- It had enough channels to operate the necessary integrated circuits (IC);
- It could be easily programmed (ASSEMBLY).

The IC used for this application, apart from resistors and capacitors, included switches and operational amplifiers. OpAmps were implemented because it was desired to have an enhanced actuation signal.

For testing and development of the PCB control system, a protoboard was used. In Fig. 5.24 the test board in use is shown.

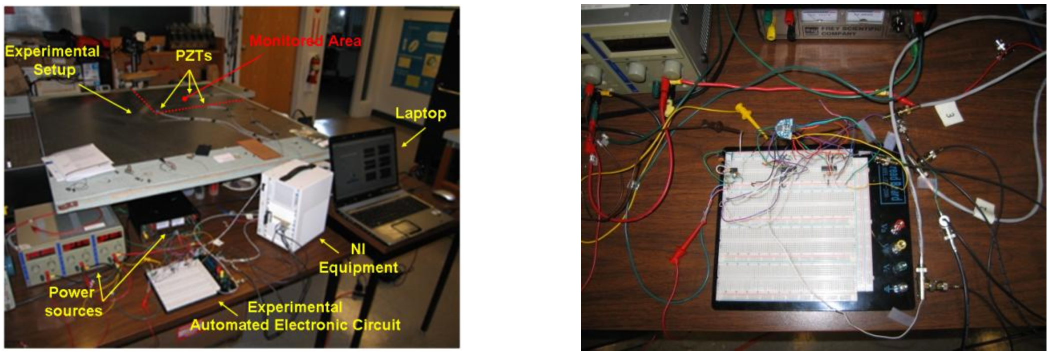

Fig. 5.24: Automated electronic circuit for network testing setup

After running several tests and fine-tuning the components, the circuit was drawn using dedicated PCB software. Fig. 5.25 shows a PCB prototype and the final board.

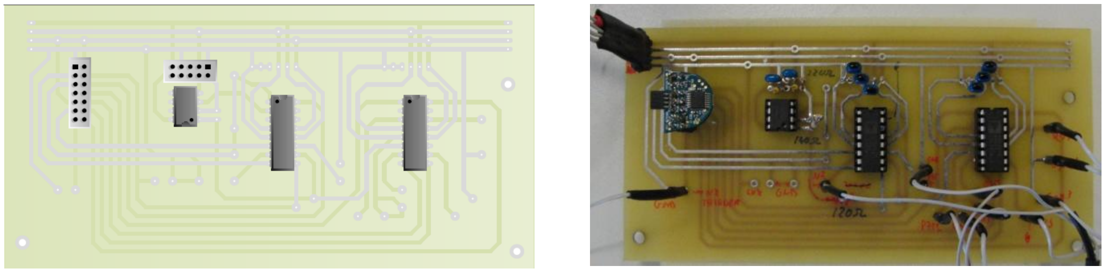

Fig. 5.25: PCB for networks prototype and final product

The data acquisition process in the LABVIEW® application was rewritten to account for the inclusion of this custom PCB. The user has then the option to run data acquisition on a manual or PCB controlled way. Fig. 5.26 illustrates the changes (Note that the wave created by the signal generation board is shown. When compared with the one output by the actuator, the expected amplification is observed. The graph on the bottom left corner represents the time during which the generation board and actuating transducer are allowed to be connected).

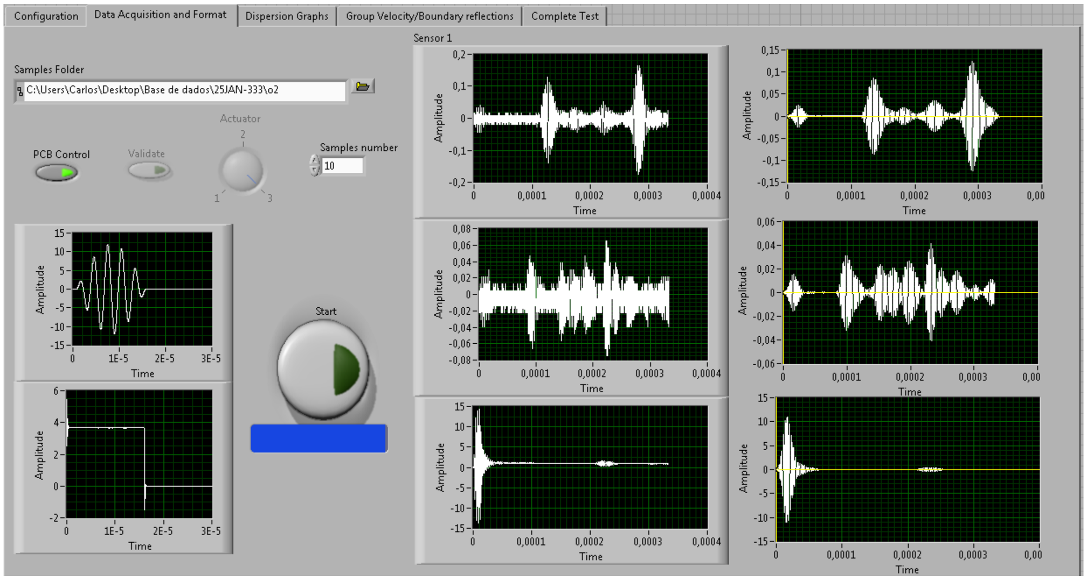

Samples Folder: C:\Users\Carlos\Desktop\Base de dados\25JAN-333\o2

Samples number: 10

Fig. 5.26: Acquisition tab (updated for the use of the PCB)

Experiments were successfully run on yet another aluminum plate with only three sensors installed and using the PCB control board. Damage was simulated by drilling a 1 mm through-thickness hole. Fig. 5.27 shows the experimental setup and the application output.

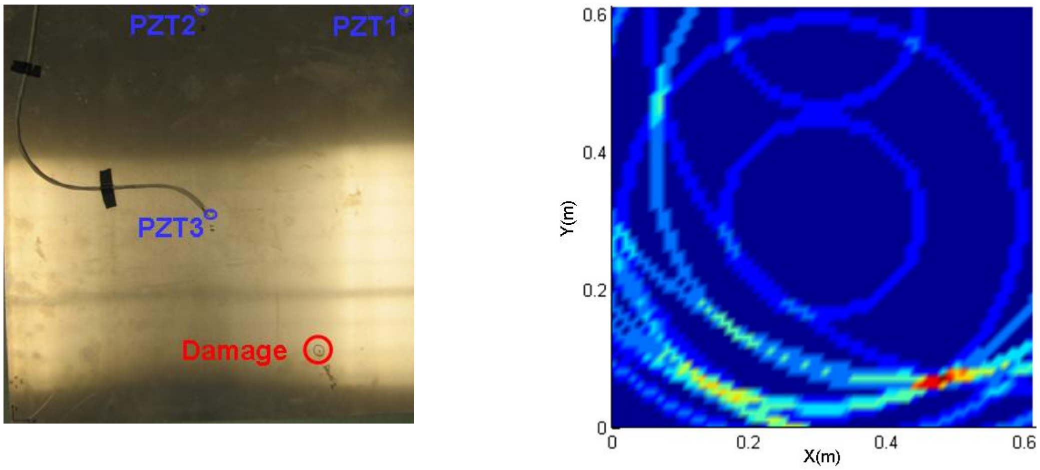

Fig. 5.27: Real and calculated damage location

Thanks to the custom PCB, the actuating sensor data was made useful and promising results were obtained. In an effort to provide better area coverage and to further reduce the appearance of false positives, the PCB was also adapted to be used in conjunction with 4 transducers (which should provide additional data).

5.4 PCB Testing on a Four Sensor Network

In order to investigate the possible application of larger diameter PZT, a 10 mm diameter transducer was employed. Having in mind that sensor diameter defines the most adequate actuation frequency, tests had to be performed in order to determine its value for this particular PZT size. Recalling that, for the S-Wave, the suitable actuation wavelength has to correspond to the twice the diameter, and by checking the wavelength dispersion graphs (Fig. 3.12), an estimate of the ideal actuation frequency was set at 250 KHz.

A new frequency scan was performed to validate the actuation frequency estimate. This test uses one PZT as an actuator and saves the response observed at a sensor. In Fig. 5.28 the scan results are presented for selected actuation frequencies between 230 KHz and 250 KHz.

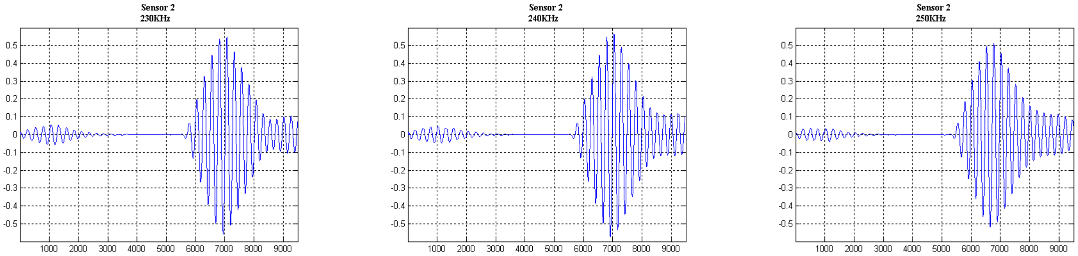

Fig. 5.28: 10 mm sensors frequency scan

The highest amplitude was registered for a 240 KHz actuation frequency, which is close to the 250 KHz estimate. Despite not being shown, the ratio between the amplitude of the A- and S-Waves is not as good as for the former PZT. The reason for this was explained in section 3.6.

The initial acquisition software was dedicated to the 333 KHz actuation frequency. The code was then adapted to allow the user to choose a variety of frequencies, in order to support new transducers. In Fig. 5.29, the major changes to the code are shown: an actuation frequency option was added, along with some filtering options, namely band pass limits and order. This version maintains the three sensor network capability.

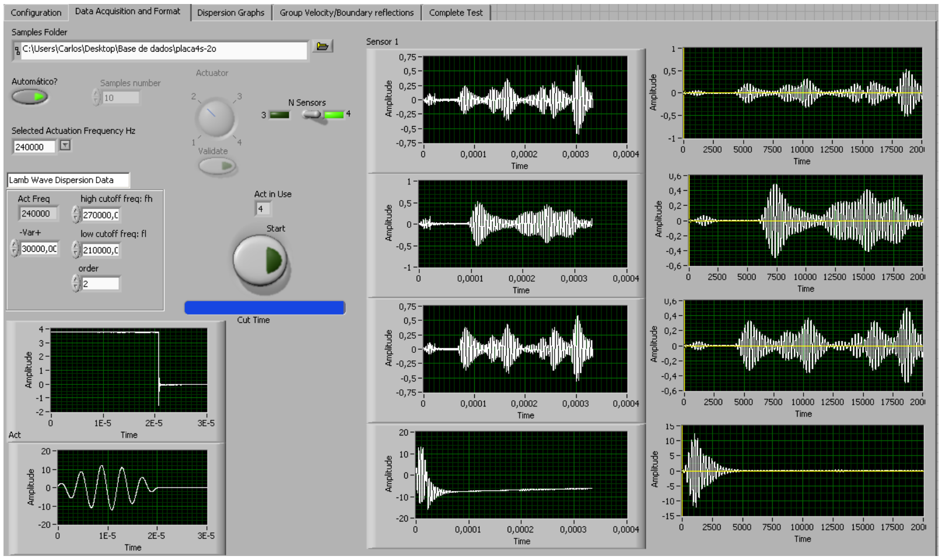

Samples Folder: C:\Users\Carlos\Desktop\Base de dados\placa4s-2o

Samples number: 10

Selected Actuation Frequency Hz: 240000

Lamb Wave Dispersion Data

Act Freq: 240000

high cutoff freq: fh: 270000,C

-Var+: 30000,0C

low cutoff freq: fl: 210000,C

order: 2

Act in Use: 4

Fig. 5.29: Acquisition tab (updated for four sensor networks)

The new experimental setup using four PZT mounted on a 2 mm thickness, 0.5 m x 0.5 m aluminum plate, can be seen in Fig. 5.30.

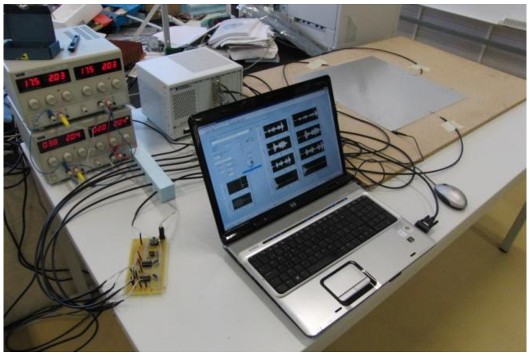

Fig. 5.30: PCB controlling four sensors experimental setup

A 1.5 mm hole was drilled at coordinates (0.15, 0.181) m and it was located, as seen in Fig. 5.31 and Fig. 5.32.

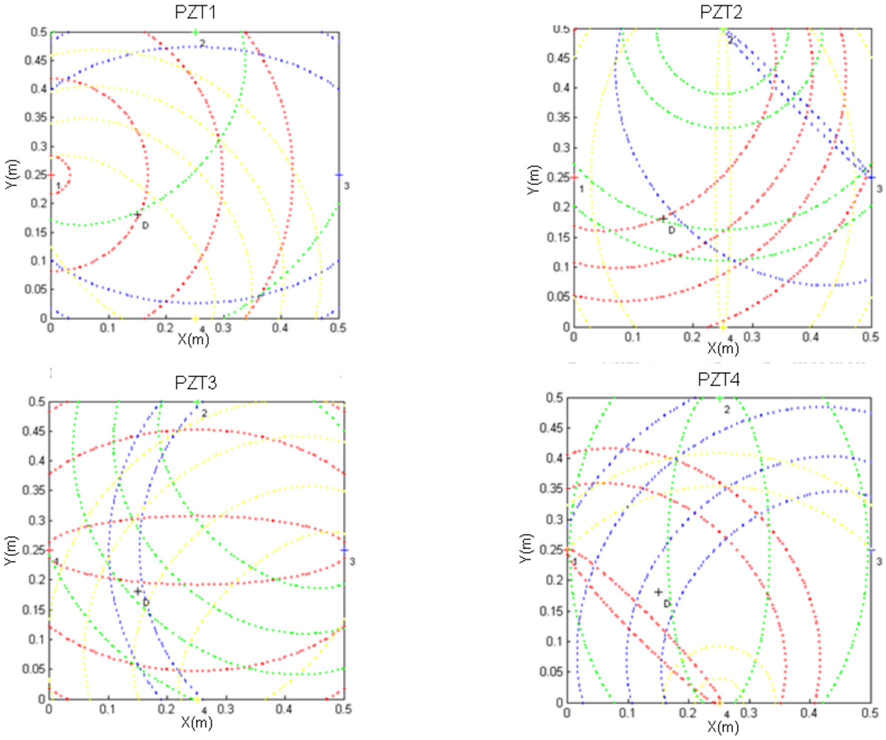

Fig. 5.31: Result sets for each actuating transducer

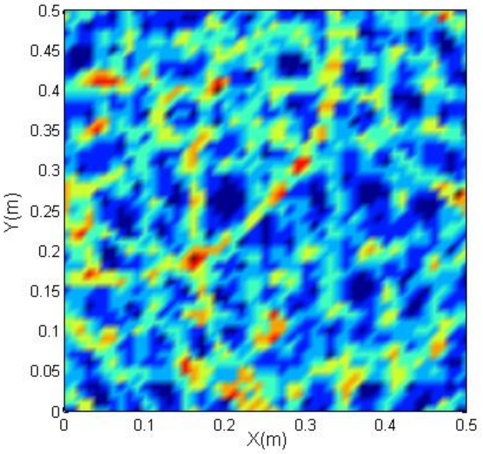

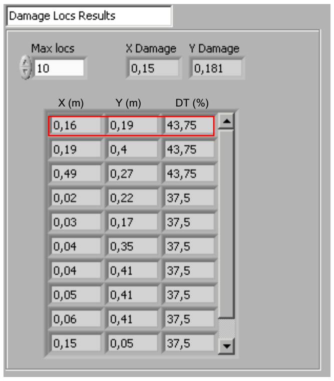

Damage Locs Results

Max locs 10

X Damage 0,15

Y Damage 0,181

X (m)	Y (m)	DT (%)
0,16	0,19	43,75
0,19	0,4	43,75
0,49	0,27	43,75
0,02	0,22	37,5
0,03	0,17	37,5
0,04	0,35	37,5
0,04	0,41	37,5
0,05	0,41	37,5
0,06	0,41	37,5
0,15	0,05	37,5

Fig. 5.32: Contour plot and damage location outputs

The inclusion of four PZT (also larger) did not show any improvements in terms of the tolerance to false positives.

5.5 Composite Plate

Given the promising results obtained with isotropic materials, the stage was set to attempt damage location in a composite medium. A 0.48m x 0.48m composite plate was manufactured using ten carbon fibre woven layers with the following layout: $[(0/90)/\pm45)/(0/90)/\pm45/(0/90)]_S$. By possessing an uneven ratio between (0/90) and ±45 layers the plate presents a higher stiffness (or Young Modulus) along the 0/90 directions.

Four 10 mm diameter PZT transducers were used. The network layout is seen in Fig. 5.33.

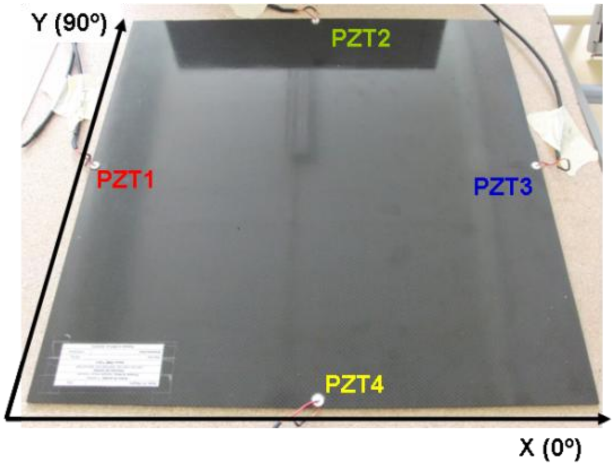

Fig. 5.33: Composite plate

5.5.1 Actuation Frequency Scan

A preliminary task that needs to be performed before damage detection is the actuation frequency scan. Every time transducers and/or the test plate are changed, this procedure needs to be executed. In order to facilitate this task, a LABVIEW® and corresponding MATLAB® codes were written.

Fig. 5.34 displays a test run in progress, where sensor one is used as an actuator. The output includes preliminary propagation velocity values. Using this feature, the user can fine tune the actuation frequency in real time.

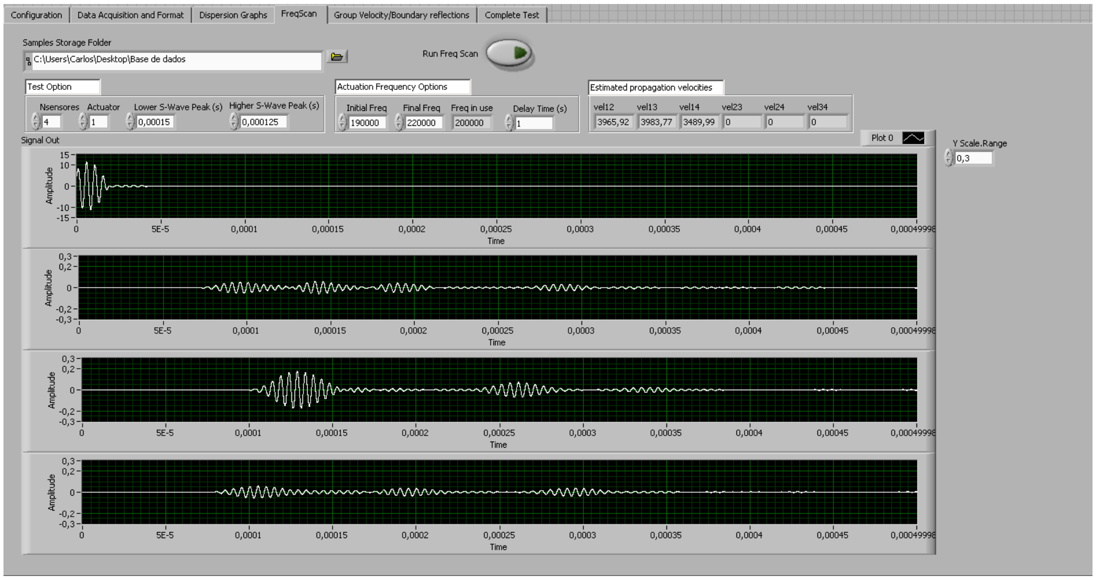

Samples Storage Folder: C:\Users\Carlos\Desktop\Base de dados

Test Option
Nsensores: 4
Actuator: 1
Lower S-Wave Peak (s): 0,00015
Higher S-Wave Peak (s): 0,000125

Actuation Frequency Options
Initial Freq: 190000
Final Freq: 220000
Freq in use: 200000
Delay Time (s): 1

Estimated propagation velocities
vel12: 3965,92
vel13: 3983,77
vel14: 3489,99
vel23: 0
vel24: 0
vel34: 0

Y Scale.Range: 0,3

Fig. 5.34: Frequency scan module

For this specific case, a frequency of 210 KHz was found to be the best.

5.5.2 Velocity Distribution

For isotropic plates, the S-Wave propagation velocity was the same for all directions. For anisotropic materials, such as composites, this property is orientation dependent, as mentioned in section 4.1.1. In order to account for this, the code for the calculation of the propagation velocity had to be updated. With this network of four sensors, each time one is used as an actuator, three sets of data will be acquired on the three sensing PZT. This provides velocity information regarding three different directions. By using all sensors, one at a time, twelve sets of data can be acquired, covering four different directions. Fig. 5.35 shows the output of the code. The data for velocity and direction is shown in matrix form.

The row index corresponds to the sensor being used as an actuator and the columns show the calculated velocity and direction for the remaining sensors. Finally, the data is processed in order to retrieve the averaged data for the four given directions.

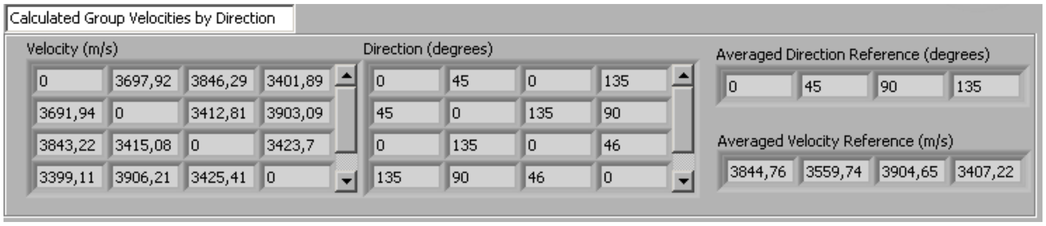

Calculated Group Velocities by Direction

Velocity (m/s)

0	3697,92	3846,29	3401,89
3691,94	0	3412,81	3903,09
3843,22	3415,08	0	3423,7
3399,11	3906,21	3425,41	0

Direction (degrees)

0	45	0	135
45	0	135	90
0	135	0	46
135	90	46	0

Averaged Direction Reference (degrees)

0	45	90	135

Averaged Velocity Reference (m/s)

3844,76	3559,74	3904,65	3407,22

Fig. 5.35: Velocity and direction data

Observing the velocity matrix, one can see that the 45 degree direction presents different values depending on the pair of sensors being used. Since a ±45 degree mesh was used, the velocities along 45 and 135 degree directions should be similar. Unexpectedly, the results from the 1-2 pair are about 7% higher than those obtained with the 3-4 pair. This may result from the fact that the meshes were manually layered, which does not guarantee a perfect placement.

Using a cubic spline, the velocity distribution can then be estimated for the entire plate. This is shown in Fig. 5.36.

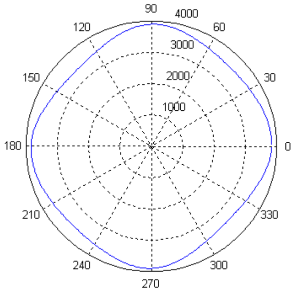

Fig. 5.36: S-Wave propagation velocity distribution

The propagation velocity of the S-Wave depends on several material properties, including Young's modulus. Using the code written for the dispersion graphs, it can be seen that, all other things being equal, the highest S-Wave velocity also corresponds to the highest Young's modulus. In fact, for the composite plate in question, the 0/90-degree directions present the highest wave propagation velocities. Additionally, since the top layer is also

0/90-degree oriented. Since the S-Wave is mainly a surface wave, the top layers will play a pivotal role in its propagation velocity.

5.5.3 Damage Location Experiment

For damage location, the previously established algorithm had to be modified. Isotropic materials present a direction independent S-Wave propagation velocity. This allows a system of circles and ellipse equations to be established-It can than be solved in order to determine the damage location. For other materials this is no longer valid. A numerical approach has to be implemented, as described in section 4.1.1. The previous code for damage location was reprogrammed to accommodate this new functionality.

A setup was prepared for damage location testing. Data from the undamaged plate was retrieved and stored. Then, a through-thickness hole of 1.5 mm was drilled at location (0.17, 0.17) m. Damage data was collected afterwards. Both the experimental setup and the damage can be seen in Fig. 5.37.

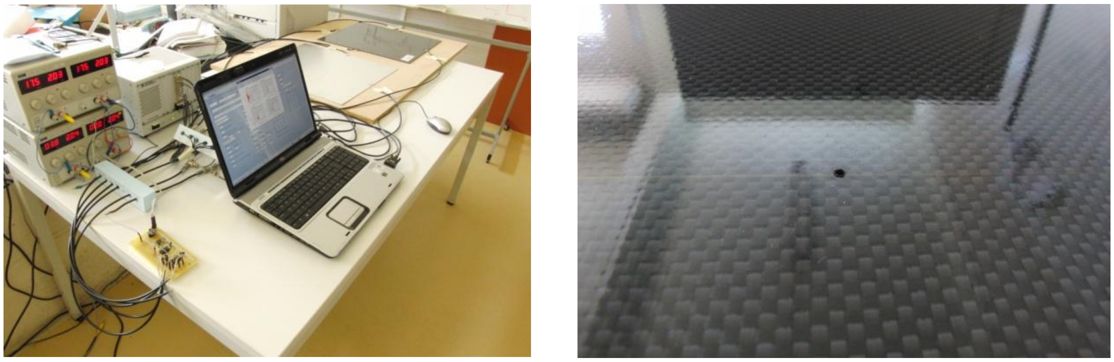

Fig. 5.37: Composite experimental setup and simulated damage

The algorithm for detection of differences was time based. This was preceded by noise treatment through a statistical process of elimination, where amplitude normalization and data alignment are performed (section 5.2.2).

Before beginning the damage location trials, undamaged data comparison took place. Several discrepancies appeared, even though there was no damage present. Nevertheless, this did not compromise the capability for damage detection. In order to overcome the referred obstacle, a new approach was proposed and implemented. Instead of comparing the damaged and undamaged signal at all times, sets of data were gathered in time intervals. The time interval size each was chosen as the Lamb wave period. So, in this case, an actuation frequency of 210 KHz corresponds to a period of 4.76×10^{-6} s. Narrowing down this window is not advisable since data analysis will then tend to be the same as in the time domain. On the other hand, enlarging it would result in a loss of precision.

Upon having these sets defined, their amplitudes are calculated by FFT. Fig. 5.38 shows the results for PZT one and three, the first being the actuator. Notice that not all amplitudes are calculated for the entire time domain. Because there is a minimum amount of time necessary for the wave to travel, the corresponding data is not considered.

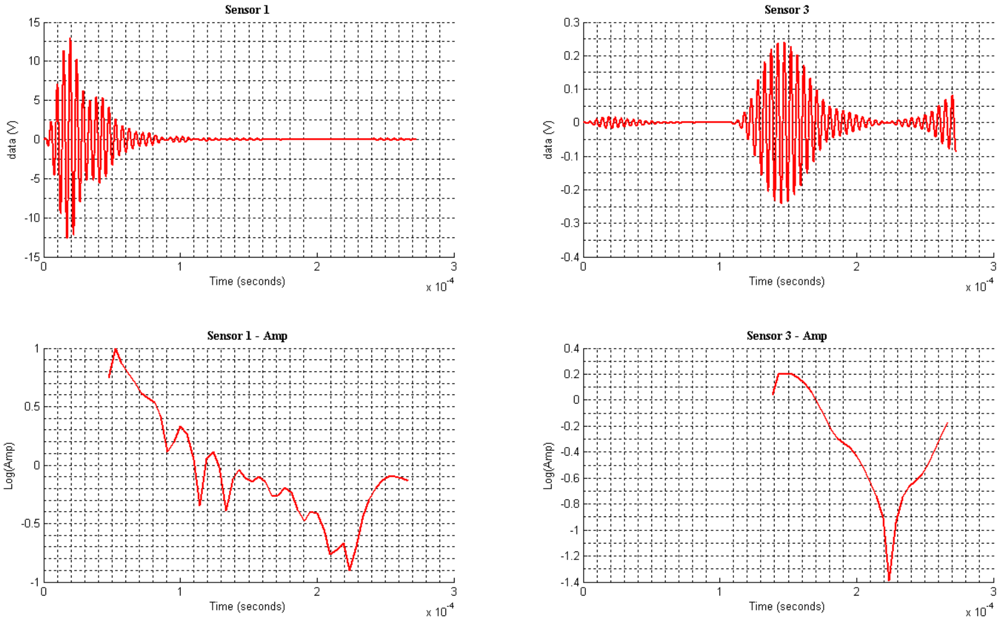

Fig. 5.38: Time and wave amplitude domain signals

Fig. 5.39 shows the differences detected between the damaged and undamaged responses, for the case in which PZT #3 is the actuator. Magenta points represent the true damage reflection. The green peaks show the differences selected based on their amplitudes.

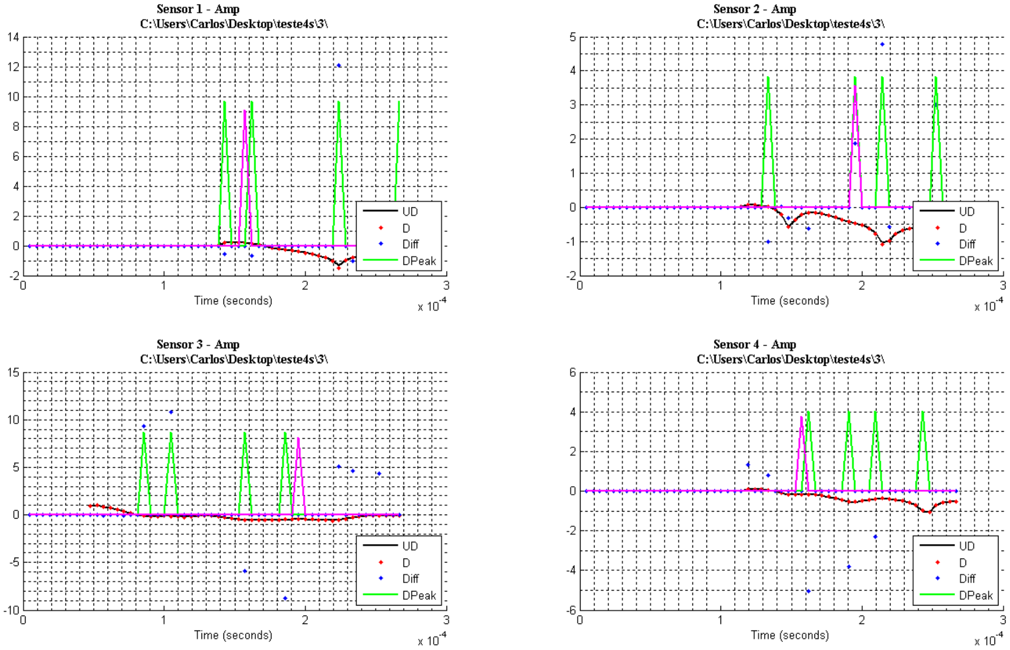

Fig. 5.39: Damage and undamaged wave amplitude comparison.

Once differences have been located, the code calculates the probable positions of damage, which can be seen in Fig. 5.40. Notice the degenerated circles and ellipses as a result of the dependence of velocity on direction.

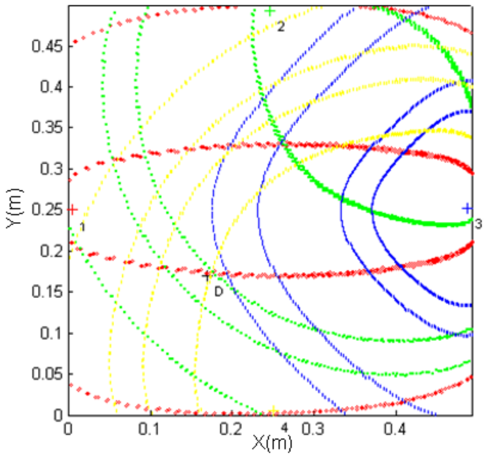

Fig. 5.40: Probable damage locations for actuating PZT #3

Having performed all the required PZT tests, damage location tests were successfully performed. Fig. 5.41 shows the software output.

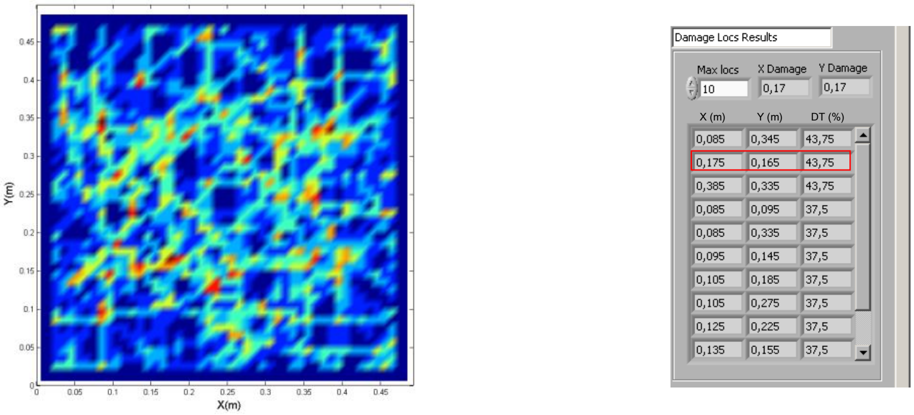

Damage Locs Results

Max locs 10

X Damage 0,17

Y Damage 0,17

X (m)	Y (m)	DT (%)
0,085	0,345	43,75
0,175	0,165	43,75
0,385	0,335	43,75
0,085	0,095	37,5
0,085	0,335	37,5
0,095	0,145	37,5
0,105	0,185	37,5
0,105	0,275	37,5
0,125	0,225	37,5
0,135	0,155	37,5

Fig. 5.41: Composite plate damage location

Even though two false positives were detected, the true damage is also pinpointed.

This new approach was also tested in the experiments from section 5.4. It is less precise and again results in two false positives, but damage was nonetheless detected. Also, the probable points are located in the same vicinity (Fig. 5.42).

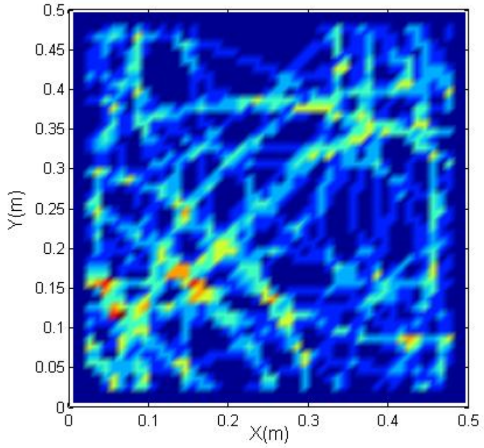

Fig. 5.42: Results for the section 5.4 setup

5.6 Networks Software Development Tool

As mentioned before, LABVIEW® natively supports the equipment in use. The fact that MATLAB® code can be embedded makes it very versatile and easy to update. The way it was implemented allows: initial Lamb wave studies and testing, natural boundaries check, and damage location detection. Fig. 5.43 shows the generic software modules.

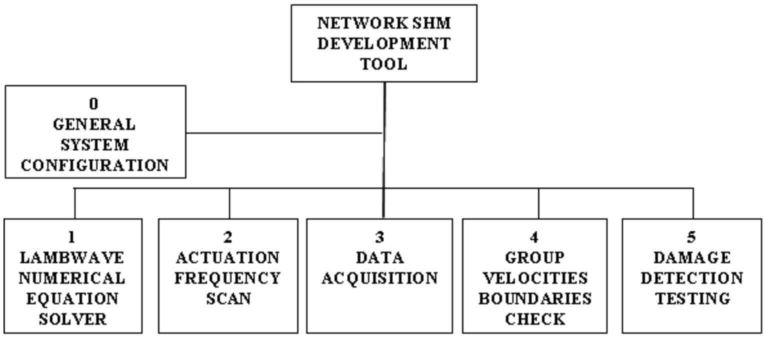

Fig. 5.43: LABVIEW® network software block diagram

The main features of the tool:

0. **General System Configuration**
   - Input:
     - National Instruments Equipment Options;
     - Sensors and test plate dimensions and position.
1. **Lamb Wave Numerical Equation Solver**
   - Input:
     - Mechanical properties;
     - Sensor diameter.
   - Output:
     - Dispersion graphs;
     - A- and S- waves preferred actuation frequency;
     - Check for wave mode separation.
2. **Actuation Frequency Scan**
   - Input:
     - Actuation frequency scan interval and actuating sensor.
   - Processing:
     - Preliminary propagation velocity calculation.
   - Output:
     - Real-time wave readings.
3. **Data Acquisition** (Manual or PCB automated process)
   - Input:
     - Actuation Frequency, band pass filter options and network size.

- Processing:
    - Statistical data treatment.
- Output:
    - Option to save and plot both raw and filtered data.

4. **Group Velocities and Boundary Check**
    - Input:
        - Data file.
    - Processing:
        - Propagation velocity calculation;
        - Determine expected boundary reflections.
    - Output:
        - Propagation velocity distribution plots;
        - Plot time data merged with expected boundary reflections.
5. **Damage Detection Testing**
    - Input:
        - Damaged and undamaged data.
    - Processing:
        - Data pre-processing, including: velocity correction, data alignment and amplitude normalization;
        - Propagation velocity calculation;
        - Time or wave amplitude domain comparison.
    - Output:
        - Plot of data and differences for time or wave amplitude domain;
        - Plot of probable locations;
        - Locations for probable damage.

The fact that it was coded in modules, allows for a smooth transition to new approaches/equipment.

5.7 Network Conclusions

Throughout this phase of the experimental work, several milestones were achieved, namely:

- Damages as small as 1-1.5 mm were successfully detected, thus proving that early stage defects can be identified (without any particular boundary condition being applied);
- Nondeterministic logic, which makes allowances for the detection of false positives through with data fusion, facilitates small damage detection;
- It is possible to use a minimum amount of sensors necessary for triangulation (three). Nonetheless, the inclusion of extra sensors allows for an extended coverage of the inspected plate;
- Signal conditioning (custom PCB) allows the acquisition of useful data from the actuating transducer and can enhance the generated Lamb wave amplitude. Furthermore, it allows a reduction in the time spent conducting damage detection tests;
- The proposed approach is valid for composites;
- Besides the choice of the best actuation frequency for the desired mode, a specific PZT model must be matched to each particular component.

CHAPTER 6

PHASED ARRAYS

Based on the lessons learnt and the experience gained during the design and implementation of sensor networks, phased arrays present a viable alternative for damage detection. Studies on beam forming and experiments on damage detection using phased array systems are presented next. It is noted that the actuation hardware system was developed in the context of another graduate studies research in the area of SHM by B. Rocha [90].

6.1 Hardware

As the name implies, a phased array system is comprised of a linear array of sensors. Each sensor is individually controlled in order to achieve the actuation objective. Thus each sensor has its own control structure. In order to manage the independent sensors, there is a hardware master circuit whose function is to trigger each individual slave system, at a pre-programmed time to form a coherent beam.

The array studied here consists of seven sensors, each being an 8mm in diameter piezo sensor. As explained in Section 3.5, these sensors present the highest actuation at a frequency of about 330 KHz. At this frequency, the corresponding wavelength is 16 mm. Following the minimum pitch condition (section 3.9.3), the distance between sensors has to be less than 8mm. Since 8 mm is the minimum physical distance between the centres of each sensor, the actuation frequency had to be lowered. On the other hand, sensors need to be placed as close as possible, in order to ensure beam forming. The smallest distance which guarantees that no interference occurs between each transducer was found to be around 1 mm (section 3.9.3). Since sensor placement is crucial to the design of the system, a custom holed ruler was manufactured using CNC machining. With the desired spacing of 1 mm, the resultant pitch was 9 mm, resulting in a wavelength higher than 18 mm. The actuation frequency was selected to be 250 KHz to minimize possible side lobes.

Fig. 6.1 illustrates the complete system, including both the hardware developed in the context of another MASc thesis [90] and the phased array system developed here.

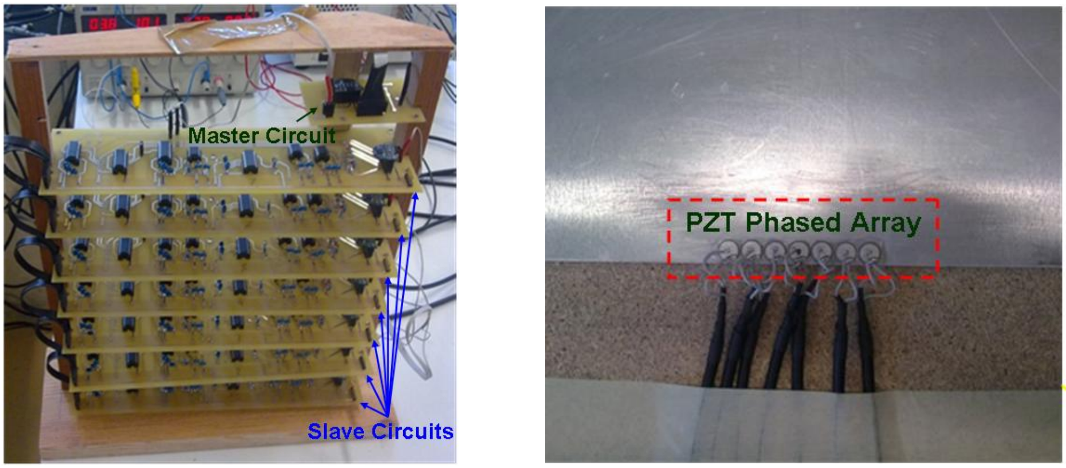

Fig. 6.1: Phased array system and implementation

6.2 Experimental Setup

In order to perform systematic tests using phased arrays, a custom designed software tool was developed. Similar to the approach adopted for sensor networks, a modular LABVIEW® application including MATLAB® code was designed and implemented.

The first step was to implement the SHM system on a test structure. As one of the objectives is to compare sensor networks to phased array systems, the setup used in section 5.2, was adapted for phased array tests (Fig. 6.2).

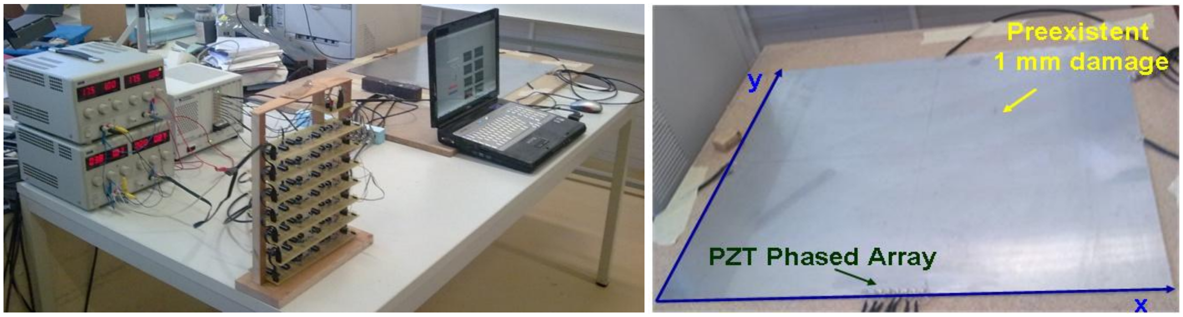

Fig. 6.2: Phased array experimental setup

A new configuration tab was set up for this particular case, as seen in Fig. 6.3.

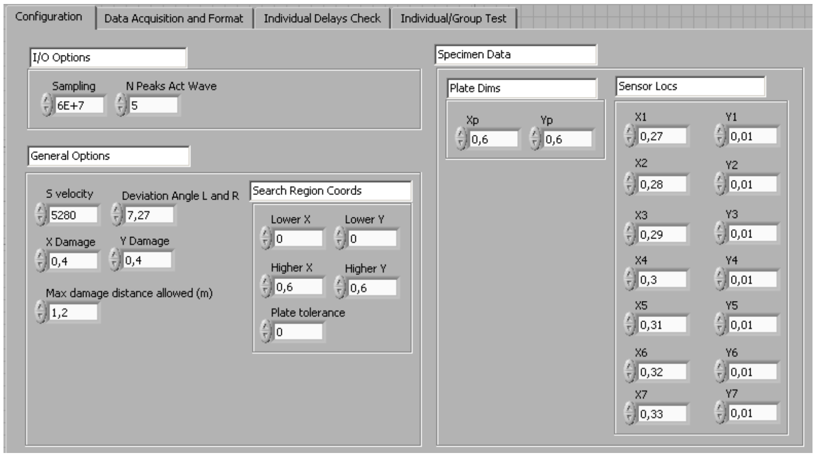

Sampling 6E+7
N Peaks Act Wave 5
S velocity 5280
Deviation Angle L and R 7,27
X Damage 0,4
Y Damage 0,4
Max damage distance allowed (m) 1,2
Lower X 0
Lower Y 0
Higher X 0,6
Higher Y 0,6
Plate tolerance 0
Xp 0,6
Yp 0,6
X1 0,27
Y1 0,01
X2 0,28
Y2 0,01
X3 0,29
Y3 0,01
X4 0,3
Y4 0,01
X5 0,31
Y5 0,01
X6 0,32
Y6 0,01
X7 0,33
Y7 0,01

Fig. 6.3: Phased array configuration tab

One difference between the two software tools is that the S-wave propagation velocity has to be provided for phased arrays. The positions of all seven transducers in the array are also user defined. The data acquisition module was also modified to fit the current system (Fig. 6.4).

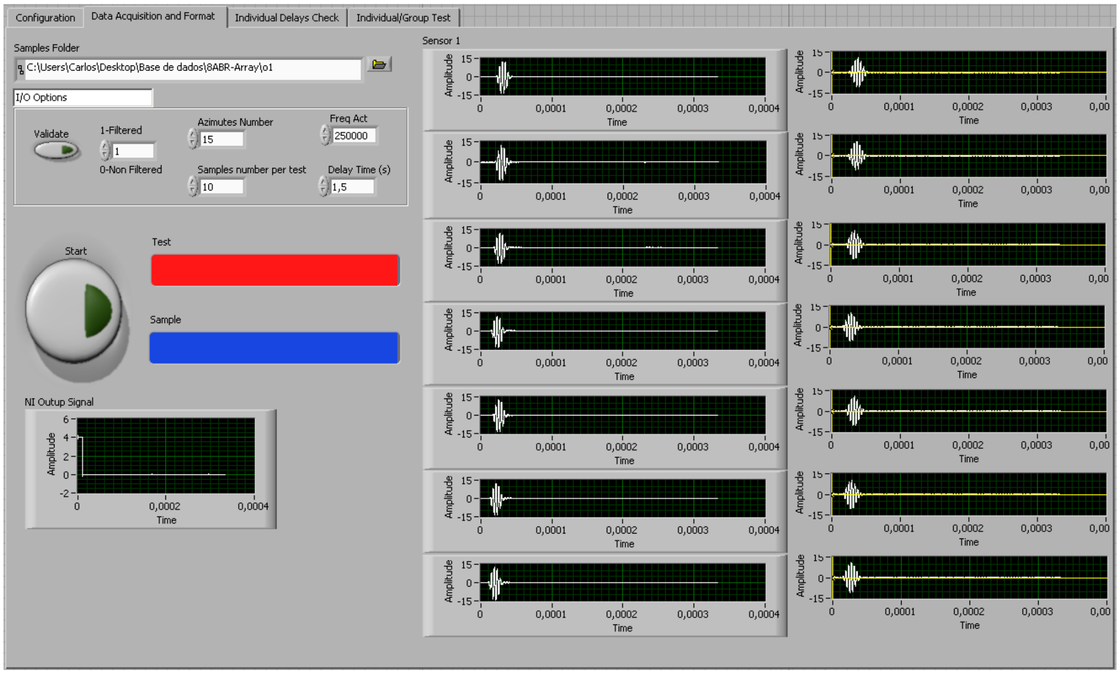

Samples Folder C:\Users\Carlos\Desktop\Base de dados\8ABR-Array\o1
1-Filtered 0-Non Filtered 1
Azimutes Number 15
Freq Act 250000
Samples number per test 10
Delay Time (s) 1,5

Fig. 6.4: Phased array data acquisition tab

Since the number of directions in the sweep and the number of samples are hard coded into the phased array control hardware, this data needs to be input by the user. Both raw and filtered data can be verified in real-time. This allows the user to have an insight into the actuation delay between each sensor.

A control module was also programmed to check the delays and the resulting beam direction, using the collected data. This module searches for the actuation peaks of each sensor so that each neighbouring difference is calculated and then converted into an orientation. The delays check module is seen in Fig. 6.5.

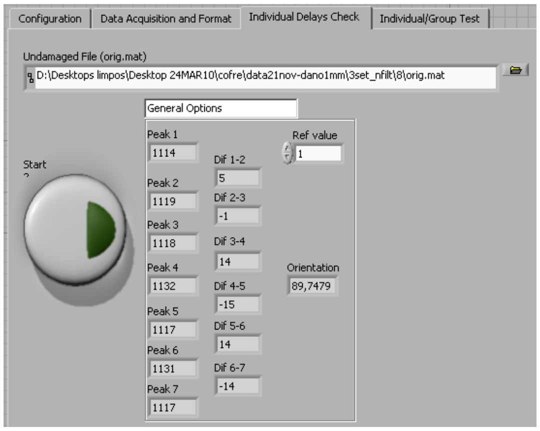

Undamaged File (orig.mat): D:\Desktops limpos\Desktop 24MAR10\cofre\data21nov-dano1mm\3set_nfilt\8\orig.mat

Peak 1: 1114
Peak 2: 1119
Peak 3: 1118
Peak 4: 1132
Peak 5: 1117
Peak 6: 1131
Peak 7: 1117
Dif 1-2: 5
Dif 2-3: -1
Dif 3-4: 14
Dif 4-5: -15
Dif 5-6: 14
Dif 6-7: -14
Ref value: 1
Orientation: 89,7479

Fig. 6.5: Phased array delays check tab

6.3 Beam Forming Testing

The sensor network structure used in section 5.2 has been used to perform experimental studies using phased arrays, and thus one of the pre-existent sensors became part of the array. The remaining three sensors were used to perform beam forming tests. Since the sensors relative location with respect to the array is known, beam forming for 45^0, 90^0 and 135^0 directions was evaluated. For each of these directions, two additional beams are tested (as seen in figure Fig. 6.6). These additional orientations are at angles that envelop the reference ones (which were pre-programmed in the hardware). As expected, beams directly aligned with the sensors show the highest S-wave amplitude.

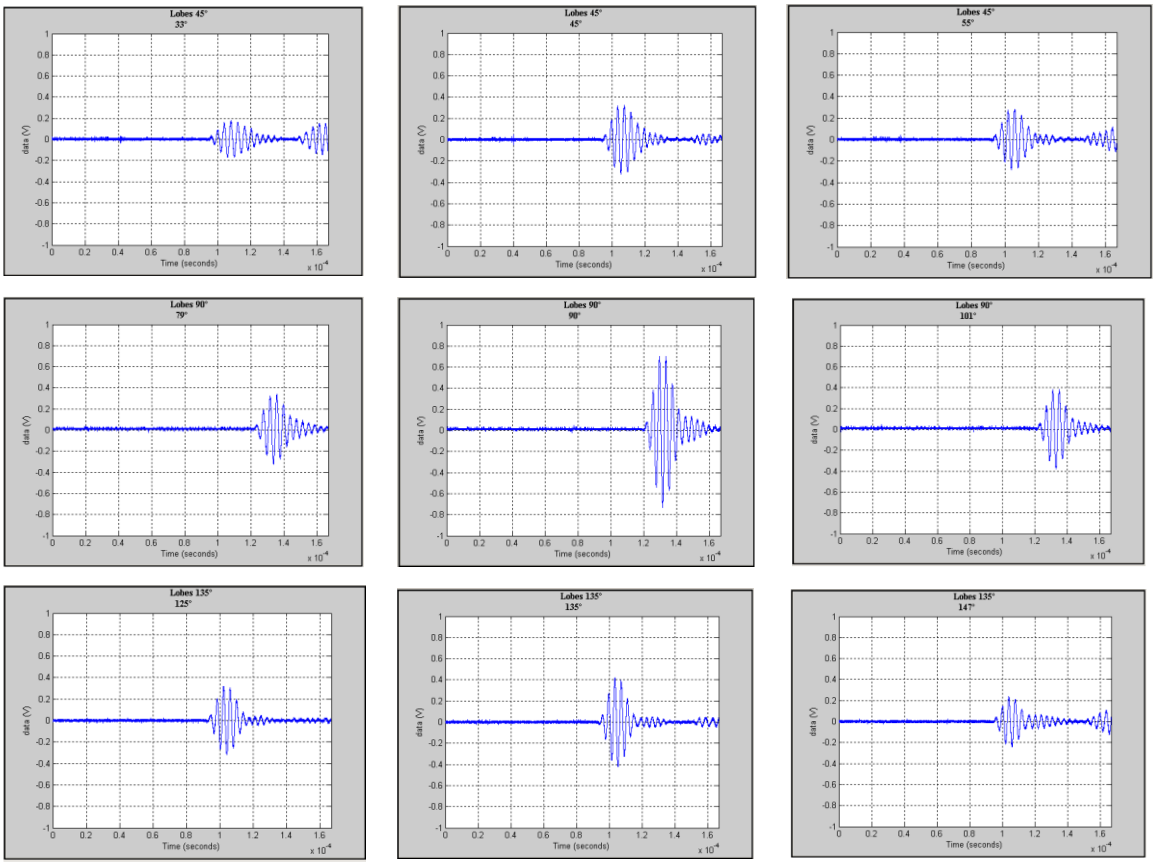

Fig. 6.6: Beam amplitude evolution for 45°, 90° and 135° directions

6.4 Damage Location Test

A new MATLAB® code was developed following the procedure outlined for damage detection using phased arrays (section 4.2). The code was incorporated on a LABVIEW® module, similar to the one presented for networks. Bearing in mind that the wavefront amplitude is quite high when compared with the waves generated in sensor networks, additional functionality was added. Therefore, besides being able to compare damaged and undamaged responses, this module allows the user to run a scan based on a single response. This approach has some similarity to the technique used in ultrasonic NDT. Fig. 6.7 shows the damage location module developed for the phased arrays, in LABVIEW®.

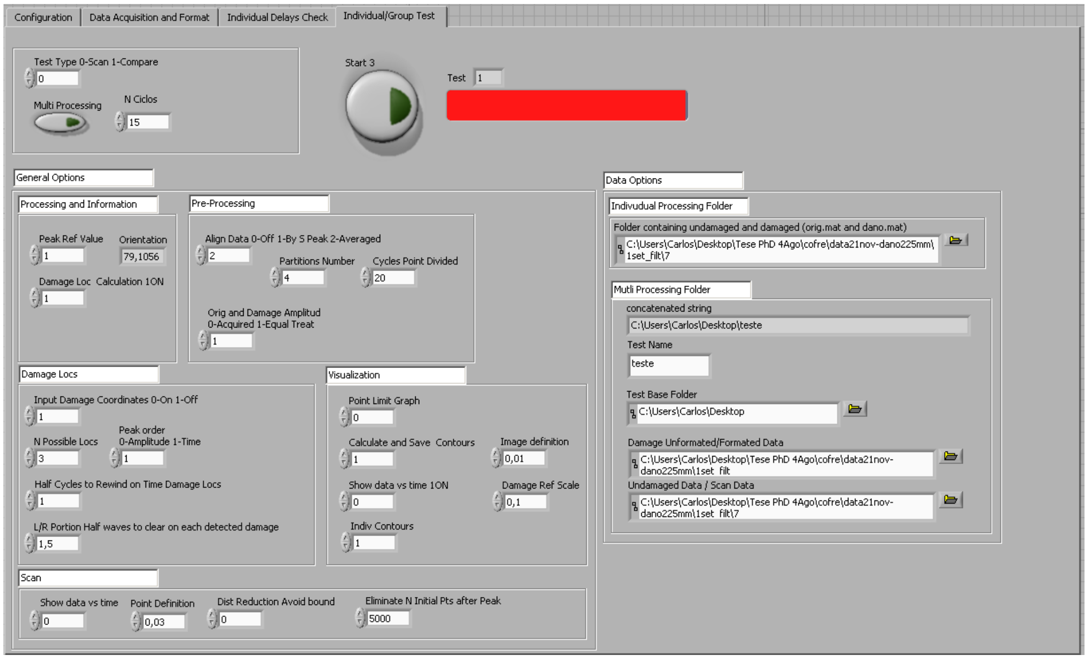

Test Type 0-Scan 1-Compare	0
Multi Processing	
N Ciclos	15
Test	1
Peak Ref Value	1
Orientation	79,1056
Damage Loc Calculation 1ON	1
Align Data 0-Off 1-By S Peak 2-Averaged	2
Partitions Number	4
Cycles Point Divided	20
Orig and Damage Amplitud 0-Acquired 1-Equal Treat	1
Input Damage Coordinates 0-On 1-Off	1
N Possible Locs	3
Peak order 0-Amplitude 1-Time	1
Half Cycles to Rewind on Time Damage Locs	1
L/R Portion Half waves to clear on each detected damage	1,5
Point Limit Graph	0
Calculate and Save Contours	1
Image definition	0,01
Show data vs time 1ON	0
Damage Ref Scale	0,1
Indiv Contours	1
Show data vs time	0
Point Definition	0,03
Dist Reduction Avoid bound	0
Eliminate N Initial Pts after Peak	5000
Folder containing undamaged and damaged (orig.mat and dano.mat)	C:\Users\Carlos\Desktop\Tese PhD 4Ago\cofre\data21nov-dano225mm\1set_filt\7
concatenated string	C:\Users\Carlos\Desktop\teste
Test Name	teste
Test Base Folder	C:\Users\Carlos\Desktop
Damage Unformated/Formated Data	C:\Users\Carlos\Desktop\Tese PhD 4Ago\cofre\data21nov-dano225mm\1set filt
Undamaged Data / Scan Data	C:\Users\Carlos\Desktop\Tese PhD 4Ago\cofre\data21nov-dano225mm\1set filt\7

Fig. 6.7: Phased array damage location tab

During the sensor network damage location testing, a 1mm through-the-thickness hole was drilled. After the array installation, data was acquired and considered as undamaged or reference signal. This means that the original plate had a discontinuity at the 1mm damage location. The damaged versus undamaged approach for the initial state had to be altered: in order to execute tests with the array, the hole was enlarged by 1 mm to simulate damage. Its position lies at (0.4, 0.4) m, considering the new coordinate system adopted for the phased array setup (Fig. 6.2).

For each pre-established direction, the phased array algorithm searches for up to four differences, sorted by their amplitudes. The software plots the time comparison between both undamaged and damaged signals. This is shown in Fig. 6.8, for the direction where damage is placed. Red lines denote the damage response. Green peaks refer to the highest differences detected, while magenta lines indicate the point where the damage effectively is.

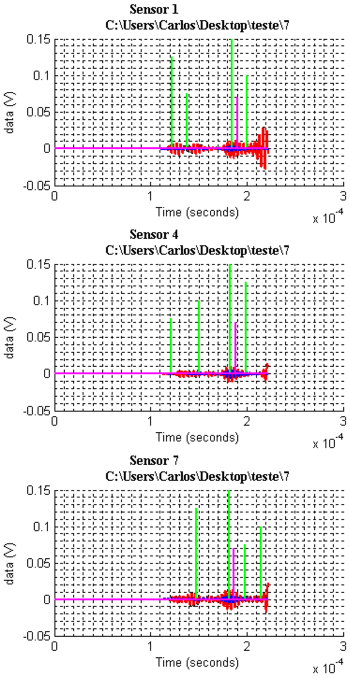

Fig. 6.8: Time data comparison for each transducer

Then, for each detected difference and for each sensor, the algorithm calculates the probable location points. Fig. 6.9 shows the probable damage locations (plotted in green) for sensor 6. The aperture limits (determined by equation (3.13)) are also illustrated.

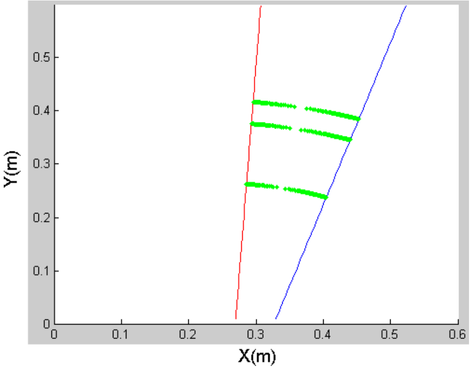

Fig. 6.9: Sensor #6 probable damage locations

For each point, the amplitude difference is stored for comparison purposes. This is done because for every direction, up to four differences are detected. Fig. 6.10 shows an example of this phase of the algorithm. The direction preceding the one where the damage is present shows the probable damage locations with significantly lower overall amplitude.

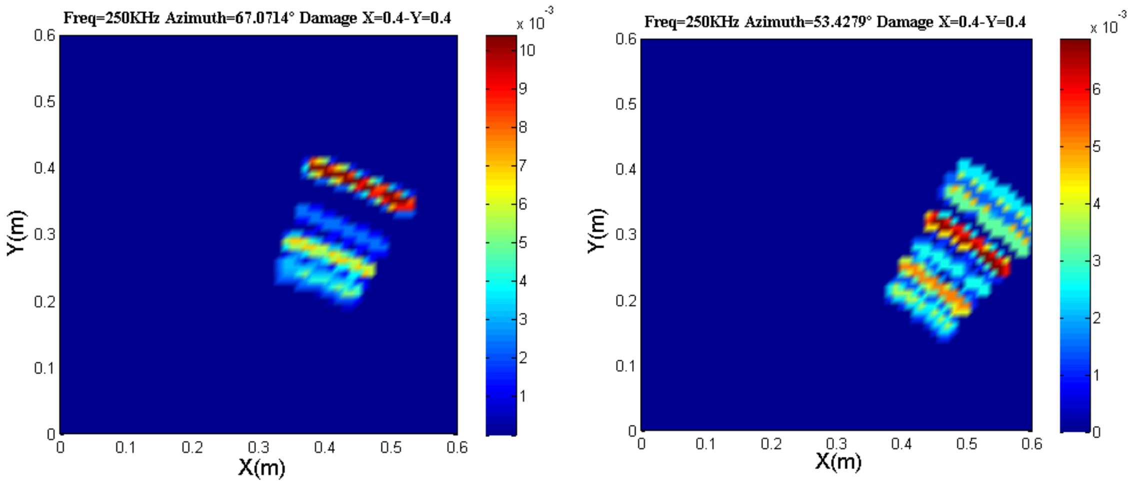

Fig. 6.10: Contour plots for two adjacent scanned azimuths

Since it is their corresponding amplitude difference that will allow the determination of the true damage position, all data should be merged in one contour plot. Fig. 6.11 shows this contour plot, where the damage is successfully pinpointed indicating the damage, as calculated by the software.

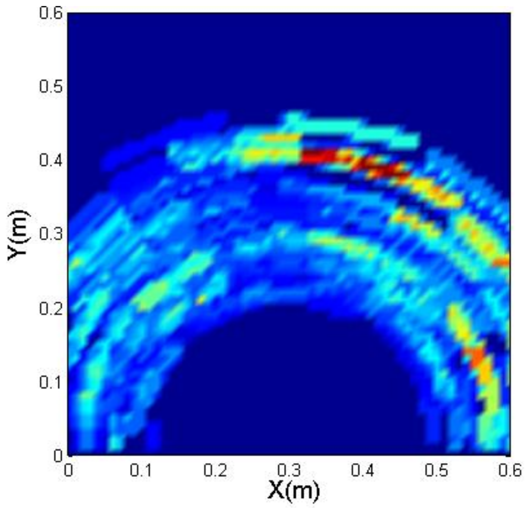

Fig. 6.11: Damage location contour output

Single response scan tests were also undertaken. In the scan results obtained prior (left) and after (right) the hole enlargement are shown in Fig. 6.12 (The red circle represents the damaged area and inside the green line is the void created by the presence of the damage).

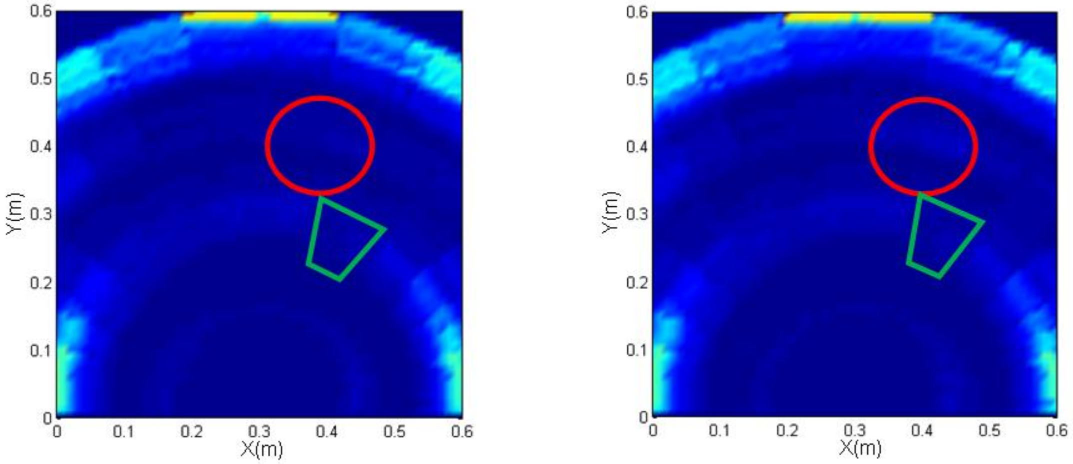

Fig. 6.12: Scan contour plots (left –1 mm damage, right – 2 mm damage)

Boundary reflections are clearly observable. However, the damage echo proved to be too small for significant differences to be observed in the overall spectrum. The damaged regions are shown in a brighter color. The attenuation of boundary reflections due to the presence of damage in that direction creates a void in the scan, which is made clearer in the damaged state. No study in the amplitude domain was undertaken for this case due to the fact that damage reflections are much more energetic than the ones verified in sensor networks. It is noted that one of the principal limitations of phased arrays is that during wave front generation, a blind spot exists in the vicinity of the array.

6.5 Phased Array Software Development Tool

Based on the same principles applied in sensor networks, the phased array software was designed and implemented. Fig. 6.13 shows the software modules.

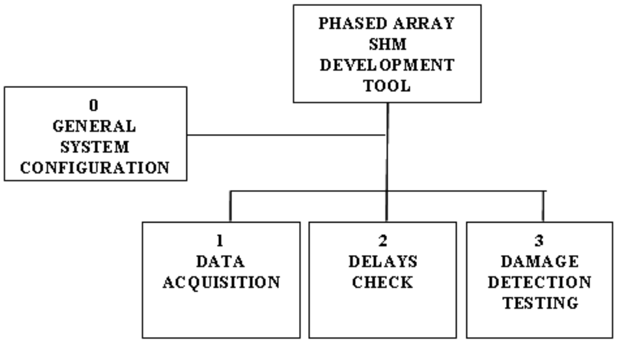

Fig. 6.13: LABVIEW® phased array software block diagram

The main features of this tool:

0. **General System Configuration**
   - Input:
     - National Instruments equipment options;
     - Sensors and test plate dimensions and position;
     - S-Wave propagation velocity.
1. **Data Acquisition**
   - Input:
     - Actuation frequency;
     - Number of azimuths to be scanned;
     - Number of samples per azimuth.
   - Processing:
     - Statistical data treatment.
   - Output:
     - Option to save and plot both raw and filtered data.
2. **Delays Check**
   - Input:
     - Data file.
   - Processing:
     - Calculate delay between each neighbouring sensor.
   - Output:
     - Azimuth.
3. **Damage Detection Testing**
   - Input:
     - Damaged and undamaged data.
   - Processing:
     - Data pre-processing, including: velocity correction, data alignment and amplitude normalization;
     - Propagation velocity calculation;
     - Time domain comparison;
     - Time domain scan.

- Output:
    - Plot of data and differences for time domain;
    - Plot of probable locations;
    - Plot scan image.

6.6 Phased Array Conclusions

The following is a summary of the findings from the experimental and computational work described in this chapter:

- The phased array hardware designed, implemented and tested can be used for damage detection. The software tool has the necessary flexibility in order to be adapted to different array designs;
- The S-wave mode can be used for damage detection;
- Damage progression of 1mm was successfully detected, which proves that detecting damage at early stages is possible;
- Nondeterministic logic, which makes allowances for the detection of false positives with data fusion, facilitates small damage detection;
- A novel approach to a damage location algorithm, based on individual acquired data, proved to be efficient and accurate.

CHAPTER 7

CONCLUSIONS

A comprehensive study on the feasibility of using Lamb waves to detect damage has been presented. The first phase of the research involved acquiring fundamental knowledge on Lamb wave's properties, enabling a better understanding on how Lamb modes propagate and behave, to identify the mode selection for damage identification and to determine the desired geometric and electric properties for the piezoelectric sensors.

Two damage identification sensor configurations were designed and implemented: the PZT network consisting of spatially distributed sensors on the plate, and the phased array consisting of a cluster of sensors located at the edge of the plate. Both architectures performed well allowing detection of 1 mm damage and its respective location. This was a significant contribution of the thesis to the state of the art and it was made possible with the development of new damage detection algorithms.

Development software tools have been designed and implemented. The open design of the software tool allows for testing of new and improved detection algorithms for damage detection.

7.1 Networks vs. Phased Arrays

A comparative study was carried out between the sensor network and phased array architectures. The main advantage of phased arrays is that signal processing is simpler (high signal to noise ratio). They are nevertheless limited by their inability to avoid blind spots. Sensor networks are simpler to implement, however, signal processing complexity (poor signal to noise ratio) is a disadvantage. Table 7.1 presents several criteria for comparison of networks with phased arrays.

Table 7.1: Networks and phased arrays comparison

Item	*Networks*	*Phased Arrays*
Signal Generation Complexity	Low	High
Number of Transducers	Small	Large
Damage detection sensitivity	1 mm	1 mm
Damage location precision	High	Low
Signal processing complexity	High	Low
Processing Time	Low	High
Reference Line Independence	Low	High
Area Coverage	High	Low

The choice of the most appropriate technique will depend on the particular application at hand. If an acquisition system is to be developed, the portability of the phased array equipment can be easily enhanced. Transducers output power and cost may determine whether they are unsuitable for network applications or too expensive for the phased array solution. The lower precision of phased arrays in terms of damage location is outweighed by their relatively simpler processing requirements. Also, the blind spots can be partially eliminated in the case where other, possibly differently shaped arrays, are installed.

A hybrid solution, combining the capabilities of networks and phased arrays may enhance the damage detection capability while minimizing the shortcomings of each.

7.2 Contributions and Findings

The developed work contributes to the state of the art of current Lamb wave application potential on different aspects, namely:

- It has been demonstrated that small damages can be detected, both for isotropic (1 mm) and composite materials (1.5 mm). This was made possible by the development of a new signal processing and detection algorithm based on nondeterministic logic principles;
- For sensor networks, data fusion was improved by enabling data to be properly sensed from the actuating sensor. This was made possible by the implementation of

a custom PCB. Also, three and four sensors solutions were successfully tested in wider areas, when compared to the available literature;

- For phased arrays, it has been demonstrated that S-waves can be used for damage detection. Due to the high wave velocity at lower frequencies, it requires a high velocity actuation, faster data acquisition with better signal processing capabilities. Here, the damage detection algorithm is a variation of the algorithm developed for the network architecture with an improved damage location strategy. Instead of globally considering one azimuth for the data acquired by the sensors, each sensor response was analyzed individually for each azimuth;
- The comparative studies between networks and phased arrays using the same sensors, test article, wave mode and data acquisition equipment shows that the damage detection using phased arrays is simpler requiring less signal processing, while requiring less sensor signal processing. However, blind areas are wider;
- Another contribution is related to the proposed method of defining the best suited sensors for the proposed application, by seeking a clear separation between both the available Lamb wave modes. This procedure distinguishes itself from what is common practice, i.e., based on a simple determination and analysis of amplitude vs. frequency for the A- and S-waves.

7.3 Future work

Given the open architecture of the software tool developed, it should be possible to implement and test other more complex signal processing strategies. This may lead to the detection of smaller damages. The effect of temperature and other environmental variables should also be researched.

Damage severity assessment is another important aspect in SHM as it completes the diagnostic phase. Additional natural progressions of the current thesis include damage prognosis and the determination of remaining useful life.

Finally, the developed strategies need to be tested on real aircraft components. Presently, a proposal has been made to the Portuguese Ministry of Defence. The proposed research program covers a wide scope of study related to condition based maintenance concepts for the Lockheed C-130 aircraft. The proposed research will address monitoring of engines using vibration based methods and structures using acoustic emission and Lamb wave health evaluation. The final objective is to enable an operational life extension, based on the implementation of the novel SHM techniques proposed here.

BIBLIOGRAPHY

[1] Marado, B.S., "Aircraft Life Concepts and Life Extension", 9th Portuguese Conference on Fracture, p1, 2004

[2] DEFSTAN 970 Requirements for the Design and Airworthiness of Composite Aircraft Structure, Defence Science and Technology

[3] Military Specification MIL A83444 Airplane Damage Tolerance Requirements

[4] ACJ 25.571, Damage Tolerance and Fatigue Evaluation of Structure (Acceptable Means of Compliance), Joint Aviation Regulations Nº25

[5] Balageas, D.L., "Structural health monitoring R&D at the European Research Establishments in Aeronautics (EREA)", Aerospace Science and Technology Vol.6, pp. 159–170, 2002

[6] Gray, J., Tillack, G.-R.,"X-ray imaging methods over the last 25 years - new advances and capabilities", Thompson, D.O., Chimenti, D.E. (eds.) Review of Progress in Quantitative Nondestructive Evaluation Vol.20, pp. 16–32. American Institute of Physics, New York, 2001

[7] Boller, C., "Ways and options for aircraft structural health management", Smart Materials and Structures Vol.10, pp. 432–440, 2001

[8] Sohn, H., Farrar, C.R., Hemez, F.M., Shunk, D.D., Stinemates, D.W., Nadler, B.R., "A Review of Structural Health Monitoring Literature: 1996-2001," Los Alamos National Laboratory Report, LA-13976-MS, 2003

[9] Achenbach, J.D., "Quantitative nondestructive evaluation", International Journal of Solids and Structures Vol.37, pp. 13–27, 2000

[10] Cheeke, J.D.N., "Fundamentals and Applications of Ultrasonic Waves", CRC Press, Boca Raton, 2002

[11] Bical, D., "NDT procedures Qualification process", ATA NDT forum, Hartford, 1995

[12] http://www.usread.com/flight587/Prelim_Report/default.html

[13] Chang, F.-K., "Introduction to health monitoring: context, problems, solutions", Presentation at the 1st European Pre-workshop on Structural Health Monitoring, Paris, France, 2002

[14] Farrar, C.R., Lieven, N.A.J., Bement, M.T. "An introduction to damage prognosis", Inman, D.J., Farrar, C.R., Lopes Jr., V., Steffen Jr., V. (eds.), Damage Prognosis: for Aerospace, Civil and Mechanical Systems, ch. 1, pp. 1–12. John Wiley & Sons, Chichester, 2005

[15] Montalvão, D., Maia, N.M.M., Ribeiro, A.M.R., "A review of vibration-based structural health monitoring with special emphasis on composite materials", The Shock and Vibration Digest Vol.38(4), pp. 295–324, 2006

[16] Rocha, B., Silva, C.P., Suleman, A., "Vibration-based Health Monitoring of Aircraft Structures", 3rd European Workshop on Structural Health Monitoring, Granada, Spain, 2006

[17] Giurgiutiu, V., Rogers, C.A., "Recent advancements in the Electro-Mechanical (E/M) impedance method for structural health monitoring and NDE", Proceedings of the SPIE Vol.3329, pp. 536–547, 1998

[18] Tandon, N., Choudhury, A., "A review of vibration and acoustic measurement methods for the detection of defects in rolling element bearings", Tribology International Vol.32, pp. 469–480, 1999

[19] Raghavan, A., Cesnik, C.E.S. , "Review of guided-wave structural health monitoring", The Shock and Vibration Digest Vol.39(2), pp. 91–114, 2007

[20] Ye, L., Su, Z., "Identification of Damage Using Lamb Waves", Lecture Notes in Applied and Computational Mechanics Vol.48, pp. 4-5, Springer, 2009

[21] Rayleigh, L., "Waves propagated along the plane surface of an elastic solid", Proceedings of the London Mathematical Society Vol.20, pp. 225–234, 1889

[22] Lamb, H. "On waves in an elastic plate", Proceedings of the Royal Society, A: Mathematical, Physical and Engineering Sciences 93, pp. 114–128, 1917

[23] Osborne, M.F.M., Hart, S.D., "Transmission, reflection and guiding of an exponential pulse by a steel plate in water, I: theory", Journal of the Acoustical Society of America Vol.17, pp. 1–18, 1945

[24] Lowe, M.J., "Matrix techniques for modelling ultrasonic waves in multilayered media", IEEE Transactions on Ultrasonics, Ferroelectrics and Frequency Control Vol.42, pp. 525–542, 1995

[25] Worlton, D.C., "Experimental confirmation of Lamb waves at megacycle frequencies", Journal of Applied Physics Vol.32, pp. 967–971, 1961

[26] Frederick, C.L., Worlont, D.C., "Ultrasonic thickness measurements with Lamb waves", Journal of Nondestructive Test Vol.20, pp. 51–55, 1962

[27] Rose, J.L., "A vision of ultrasonic guided wave inspection potential, Proceedings of the Seventh ASME NDE Topical Conference", NDE-Vol. 20 (1–5), 2001

[28] Dalton, R.P., Cawley, P., Lowe, M.J., "The Potential of Guided Waves for Monitoring Large Areas of Metallic Aircraft Fuselage Structure", Journal of Nondestructive Evaluation Vol. 20, No. 1, 2001

[29] Giurgiutiu, V, Bao, J., "Embedded Ultrasonic Structural Radar With Piezoelectric Wafer Active Sensors for the NDE of Thin-Wall Structures", ASME International Mechanical Engineering Congress, New Orleans-LA, USA, 2002

[30] Rose, J.L., "Ultrasonic Waves in Solid Media", Cambridge University Press, New York, 1999

[31] Lee, B.C., Staszewski, W.J., "Modelling of Lamb waves for damage detection in metallic structures: Part I - Wave propagation", Smart Materials and Structures Vol.12, pp. 804–814, 2003

[32] Lee, B.C., Staszewski, W.J., "Modelling of Lamb waves for damage detection in metallic structures: Part II - Wave interactions with damage", Smart Materials and Structures Vol.12, pp. 804–814, 2003

[33] Apetre, N., Ruzzene, M., Hanagud, S., Gopalakrishman, S., "Nonlinear Spectral Methods for the Analysis of Wave Propagation" ", 49th AIAA/ASME/ASCE/AHS/ASC Structures, Structural Dynamics, and Materials, Schaumburg-IL, USA, 2008

[34] Galan, J.M., Abascal, R., "Boundary element solution for the bidimensional scattering of guided waves in laminated plates", Computers & Structures Vol.83, Issues 10-11, pp. 740-757, 2005

[35] Ostachowicz, W.M., "Damage detection of structures using spectral finite element method", Computers and Structures Vol.86, pp. 454–462, 2008

[36] Blaise, E., Chang, F.-K., "Built-in diagnostic for debonding in sandwich structures under extreme temperature-2", Chang, F.-K. (ed.) Proceedings of the 3rd International Workshop on Structural Health Monitoring, Stanford, CA, USA, September 12-14, 2001, pp. 154–163, CRC Press, Boca Raton, 2001

[37] Blaise, E., Chang, F.-K., "Built-in damage detection system for sandwich structures under cryogenic temperatures", Proceedings of the SPIE Vol.4701, pp. 97–107, 2002

[38] Konstantinidis, G., Drinkwater, B.W., Wilcox, P.D., "The temperature stability of guided wave structural health monitoring systems", Smart Materials and Structures Vol.15, pp. 967–976, 2006

[39] Nguyen, C.-H., Pietrzko, S., Buetikofer, R., "The influence of temperature and bonding thickness on the actuation of a cantilever beam by PZT patches", Smart Materials and Structures Vol.13, pp. 851–860, 2004

[40] Zhao, X., Gao, H., Zhang, G., Ayhan, B., Yan, F., Kwan, C., Rose, J.L., "Active health monitoring of an aircraft wing with embedded piezoelectric sensor/actuator network: I. defect detection, localization and growth monitoring", Smart Materials and Structures Vol.16, pp. 1208–1217, 2007

[41] Monnier, T., "Lamb waves-based impact damage monitoring of a stiffened aircraft panel using piezoelectric transducers", Journal of Intelligent Material Systems and Structures Vol.17, pp. 411–421, 2006

[42] Lu, Y., Ye, L., Su, Z., Huang, N., "Quantitative evaluation of crack orientation in aluminium plates based on Lamb waves", Smart Materials and Structures Vol.16, pp. 1907–1914, 2007

[43] Jin, J., Quek, S.T., Wang, Q., "Design of interdigital transducers for crack detection in plates", Ultrasonics Vol.43, pp. 481–493, 2005

[44] CeramTec AG Catalog - MF080007/D/GB/ 2.000/0807/echolot (3570)

[45] Chambers, J. T., Wardle B. L., Kessler, S. S., "Durability Assessment of Lamb Wave-Based Structural Health Monitoring Nodes", 47th AIAA/ASME/ASCE/AHS/ASC Structures, Structural Dynamics, and Materials, Newport-RI, USA, 2006

[46] Bottai, G.S., Pollock, P.J., Behling, T.A., Giurgiutiu, V., Bland, S.M., Joshi, S.P., "Damage Detection in Cryogenic Composites for Space Applications Using Piezoelectric Wafer Active Sensors", 49th AIAA/ASME/ASCE/AHS/ASC Structures, Structural Dynamics, and Materials, Schaumburg-IL, USA, 2008

[47] Giurgiutiu, V., Bao, J., Zhao, W., "Piezoelectric wafer active sensor embedded ultrasonics in Beams and plates", Experimental Mechanics Vol.43(4), pp. 428–449, 2003

[48] Park, G., Sohn, H., Farrar, C. R., Inman, D. J., "Overview of Piezoelectric Impedance-Based Health Monitoring and Path Forward", The Shock and Vibration Digest Vol.35, no6, 2003

[49] IFFM, USHF, "Piezotransducer network design", 1st Annual Meeting, Lisbon, Portugal, 2005

[50] Worden, K., Dulieu-Barton, J. M., "An Overview of Intelligent Fault Detection in Systems and Structures", Structural Health Monitoring Vol.3(1), pp. 85-98, 2004

[51] Nieuwenhuis, J. H., Neumann, J. J., Greve, D. W., Oppenheim, I. J, "Generation and Detection of Guided Waves using PZT Wafer Transducers", IEEE Ultrasonics, Ferroelectrics, and Frequency Control Society Vol.5(11), pp. 2103 – 2111, 2005

[52] Giurgiutiu, V., "Tuned Lamb Wave Excitation and Detection with Piezoelectric Wafer Active Sensors for Structural Health Monitoring", Journal of Intelligent Material Systems and Structures Vol.16, pp. 291-305, 2005

[53] Quek, S.T., Tua, P.S., Jin, J., "Comparison of plain piezoceramics and inter-digital transducer for crack detection in plates", Journal of Intelligent Material Systems and Structures Vol.18, pp. 949–961, 2007

[54] http://www.ktech.com/ (last visited February 2009)

[55] Rogers, A., "Distributed optical-fibre sensing", Measurement Science and Technology Vol.10, pp. 75–99, 1999

[56] Betz, D.C., Thursby, G., Culshaw, B., Staszewski, W.J., "Structural damage location with fiber Bragg grating rosettes and Lamb waves", Structural Health Monitoring: An International Journal Vol.6(4), pp. 299–308, 2007

[57] Amano, M., Okabe, Y., Takeda, N., Ozaki, T., "Structural health monitoring of an advanced grid structure with embedded fiber Bragg grating sensors", Structural Health Monitoring: An International Journal Vol.6(4), pp. 309–324, 2007

[58] Kwun, H., Light, G.M., Kim, S.-Y., Spinks, R.L., "Magnetostrictive sensor for active health monitoring in structures", Proceedings of the SPIE Vol.4702, pp. 282–288, 2002

[59] Varadan, V.K., "Nanotechnology, MEMS and NEMS and their applications to smart systems and devices", Proceedings of the SPIE Vol.5062, pp. 20–43, 2003

[60] Neumann, J.J., Greve, D.W., Oppenheim, I.J., "Comparison of piezoresistive and capacitive ultrasonic transducers", Proceedings of the SPIE Vol.5391, pp. 230–238, 2004

[61] Giurgiutiu, V., Cuc, A., "Embedded non-destructive evaluation for structural health monitoring, damage detection, and failure prevention", The Shock and Vibration Digest Vol.37(2), pp. 83–105, 2005

[62] Wang, L., Yuan, F.G., "Group velocity and characteristic wave curves of Lamb waves in composites: modeling and experiments", Composites Science and Technology Vol.67, pp. 1370–1384, 2007

[63] Rose, J.L., Pilarski, A., Ditri, J.J., "An approach to guided wave mode selection for inspection of laminated plate", Journal of Reinforced Plastics and Composites Vol.12, pp. 536–544, 1993

[64] Su, Z., Ye, L., "Selective generation of Lamb wave modes and their propagation characteristics in defective composite laminates" Proceedings of the Institution of Mechanical Engineers Part L - Journal of Materials: Design and Applications Vol.218, pp. 95–110, 2004

[65] Wilcox, P.D., Lowe, M.J.S., Cawley, P., "Mode and Transducer Selection for Long Range Lamb Wave Inspection", Journal of Intelligent Material Systems and Structures Vol.12(8), pp. 553-565, 2001

[66] Chakrabarty, K., Iyengar, S.S., Ai, H., Cho, E., "Grid Coverage for Surveillance and Target Location in Distributed Sensor Networks", IEEE Transactions on Computers Vol.51, pp. 1448–1453, 2002

[67] Staszewski, W.J., Worden, K., "Overview of optimal sensor location methods for damage detection", Rao, V.S. (ed.) Proceedings of the 8th SPIE Symposium on Smart Structures and Materials (Conference on Modelling, Signal Processing and Control of Smart Structures) Vol.4326, pp. 179–187, Newport Beach, CA, USA, 2001

[68] Guo, H.Y., Zhang, L., Zhang, L.L., Zhou, J.X., "Optimal placement of sensors for structural health monitoring using improved genetic algorithms", Smart Materials and Structures Vol.13, pp. 528–534, 2004

[69] Tongpadungrod, P., Rhys, T.D.L., Brett, P.N., "An approach to optimise the critical sensor locations in one-dimensional novel distributive tactile surface to maximize performance", Sensors and Actuators A: Physical Vol.105, pp. 47–54, 2003

[70] Lee, B.C., Staszewski, W.J., " Sensor location studies for damage detection with Lamb waves", Smart Materials and Structures Vol.16, pp. 399–408, 2007

[71] Bao, J., "Lamb Wave Generation and Detection with Piezoelectric Wafer Active Sensors", PhD Thesis, College of Engineering and Information Technology, University of South Carolina, 2003

[72] Salas, K.I., Cesnik, C.E.S., "Guided Wave Experimentation using CLoVER Transducers for Structural Health Monitoring", 49th AIAA/ASME/ASCE/AHS/ASC Structures, Structural Dynamics, and Materials, Schaumburg, IL, 2008

[73] Michaels, J.E., Michaels, T.E., " Guided wave signal processing and image fusion for in situ damage localization in plates", Wave Motion Vol.44, pp. 482–492, 2007

[74] Sohn, H., Park, H.W., Law, K.H., Farrar, C.R., "Combination of a time reversal process and a consecutive outlier analysis for baseline-free damage diagnosis", Journal of Intelligent Material Systems and Structures Vol.18, pp. 335–346, 2007

[75] Prada, C., Kerbrat, E., Cassereau, D., Fink, M., "Time reversal techniques in ultrasonic nondestructive testing of scattering media", Inverse Problems Vol.18, pp. 1761–1773, 2002

[76] Xu, B., Giurgiutiu, V., "Single mode tuning effects on Lamb wave time reversal with piezoelectric wafer active sensors for structural health monitoring", Journal of Nondestructive Evaluation Vol.26, pp. 123–134, 2007

[77] Gomez-Ullate, Y., Espinosa, F., Reynolds, P., Mould, J., "Selective Excitation of Lamb Wave Modes in Thin Aluminium Plates using Bonded Piezoceramics: Fem Modelling and Measurements", Poster 205, ECNDT, 2006

[78] Gao, W., Glorieux, C., Thoen, J., "Laser ultrasonic study of Lamb waves: determination of the thickness and velocities of a thin plate", International Journal of Engineering Science Vol.41, pp. 219–228, 2003

[79] Paget, C.A., Grondel, S., Levin, K., Delebarre, C., " Damage assessment in composites by Lamb waves and wavelet coefficients", Smart Materials and Structures Vol.12, pp. 393–402, 2003

[80] Yuan, S., Liang, D., Shi, L., Zhao, X., Wu, J., Li, G., Qiu, L., "Recent progress on distributed structural health monitoring research at NUAA", Journal of Intelligent Material Systems and Structures Vol.19, pp. 373–386, 2008

[81] Rizzo, P., di Scalea, F.L., " Feature extraction for defect detection in strands by guided ultrasonic waves", Structural Health Monitoring: An International Journal Vol.5(3), pp. 297–308, 2006

[82] Chang, F.-K., Markmiller, F.C., Ihn, J.-B., Cheng, K.Y., "A potential link from damage diagnostics to health prognostics of composites through built-in sensors", Journal of Vibration and Acoustics Vol.129, pp. 718-729, 2007

[83] Ihn, J.-B., Chang, F.-K., "Pitch-catch active sensing methods in structural health monitoring for aircraft structures", Structural Health Monitoring: An International Journal Vol.7(1), pp. 5–19, 2008

[84] Raghavan, A., Cesnik, C.E.S., "Effects of elevated temperature on guided-wave structural health monitoring", Journal of Intelligent Material Systems and Structures Vol.19, pp. 1383–1398, 2008

[85] Wang, L., Yuan, F.G., "Damage identification in a composite plate using prestack reverse-time migration technique", Journal of Intelligent Material Systems and Structures Vol.12, pp. 469–482, 2001

[86] Malinowski, P., Wandowski, T., Trendafilova, I., Ostachowicz, W., "A Phased Array-based Method for Damage Detection and Localization in Thin Plates", Structural Health Monitoring Vol.31, pp. 611–628, 2009

[87] Yu, L., Santoni-Bottai, G., Xu, B., Liu, W., Giurgiutiu, V., "Piezoelectric wafer active sensors for in situ ultrasonic-guided wave SHM", Fatigue & Fracture of Engineering Materials & Structures, 2008

[88] Read, I., Foote, P., McFeat, J., MacPheat, Y., "Flight Trials of Structural Damage Detection Systems on a Fast Military Jet", 4th EWSHM, Krakow, Poland, 2008

[89] Giurgiutiu, V., "Structural Health Monitoring with Piezoelectric Wafer Active Sensors", Elsevier Academic Press, Boston, 2008

[90] Rocha, B., "Structural Health Monitoring of Aircraft Structures: Phased Array Development ", MASc Thesis (*in preparation*), Department of Mechanical Engineering, University of Victoria, 2010